

UNIMORE
UNIVERSITÀ DEGLI STUDI DI
MODENA E REGGIO EMILIA

UNIVERSITY OF MODENA AND REGGIO EMILIA

"Enzo Ferrari" Department of Engineering

Master's Degree in Electronics Engineering

Analysis of an Analog Bipolar multiplier at cryogenic and room temperature

Supervisor:
Prof. Mattia Borgarino

Candidate:
Matteo Biscolli
Student ID 195420

ACADEMIC YEAR 2025/2026

Contents

List of Figures **4**

List of Tables **7**

Introduction **1**

1 Cryogenic RFIC for quantum technologies **3**
1.1 RFIC front-ends 3
1.2 Mixer Theory 12
1.3 HBT SiGe 4K characterization 14
1.3.1 IHP HBT SG13G2 19
1.4 Cryo-CMOS differences and improvement 22

2 Analytical modelization of a degenerated differential couple **25**
2.1 DC Transfer Function 25
2.1.1 Harmonic Analysis 33
2.1.2 Application 35
2.2 Validation of the Analytical Model 35
2.2.1 DC behaviour 35
2.3 Overall Comparison 39
2.4 Comparing the two configuration for same transconductance value 40
2.5 Conclusions 41

3 Gilbert multiplier vs Jones demodulator **43**
3.1 Introduction 43
3.2 Gilbert multiplier 44
3.3 Circuit Analysis 45
3.3.1 Circuit simulation and comparison 51
3.3.2 SFDR analytical evaluation 60
3.4 Jones demodulator 67

3.5 Analytical evaluation and simulation result 69
3.5.1 SFDR in classical switching topology 73
3.6 Circuit comparison in short 74
3.6.1 SFDR obtained from analytical model 74
3.6.2 SFDR obtained from the simulation 74
3.7 Final Consideration 75

4 RF Figure of Merit for the Gilbert multiplier 77
4.1 1 dB CP and IIP3 77
4.2 Noise Figure (NF) 81
4.3 Port Isolation 81
4.4 Results Summary 84

Conclusion 85

A Current Mirror approximation [19] 87

B Cardano's demonstration 89

List of Figures

1.1.1 Superheterodyne receiver 4
1.1.2 Heterodyne receiver 4
1.1.3 Hartley receiver [8] 5
1.1.4 Weaver receiver [9] 5
1.1.5 Direct transmitter 6
1.1.6 Two-Step transmitter 6
1.1.7 Offset VCO transmitter 7
1.1.8 SSB transmitter [14] 7
1.1.9 Representation of a Quantum microprocessor as an array of N resonance frequencies (reported as $f_{R,i}, \quad i \in [1, N]$) and microwave pulse spectra (red curve) for a DSB-SC (**a**), USSB (**b**) and LSSB (**c**) modulation architecture [14, 15] 8
1.1.10Bloch sphere representation 9
1.2.1 Upconversion mixer 12
1.2.2 Downconversion mixer 12
1.3.1 Qualitative band diagram of an HBT. 16
1.3.2 Qualitative band diagram of an HBT. 17
1.3.3 Simulated $I_C - V_{BE}$ (**a**) and $I_B - V_{BE}$ (**b**) plot for the HBT (IHP), for 300K and 4K. 20
1.3.4 Output characteristics for the HBT (IHP). 20
1.3.5 β plotted versus I_C for the HBT (IHP). 21
1.3.6 η_C vs I_C at 300 K (**a**) and 4 K **b** 21
1.4.1 "Measured $I_D(V_{GS})$ characteristics of thin-oxide NMOS in 40-nm CMOS. V_{DS} = [0.1 V; 0.6 V; 1.1 V]. Solid line: 4 K; dashed line: 300 K."[48] 23

2.1.1 Differential amplifier stage 25
2.2.1 Linear Sweep of V_{IN} for 300K and 4K 36
2.2.2 Matlab spectrum obtained for 300K (on the left) and 4K (on the right) calculated from Equation 2.1.13 38

2.2.3 FFT spectrum for 300K (on the left) and 4K (on the right) from circuit simulation 39
2.4.1 Spectrum evaluation for current value of $735uA$ 40

3.2.1 Schematic of the Gilbert multiplier 44
3.3.1 Schematic of Gilbert multiplier implemented in the IHP technology 52
3.3.2 Amplitude of second-order intermodulation product versus V_{LO} (**a**) and V_{IF} (**b**) for $V_{IF} = 100\,\text{mV}$ and $V_{LO} = 100\,\text{mV}$, respectively, at 300 K. 56
3.3.3 Amplitude of third-order intermodulation product at $\omega_{LO} \pm 3\omega_{IF}$ versus V_{LO} (**a**) and V_{IF} (**b**) for $V_{IF} = 100\,\text{mV}$ and $V_{LO} = 100\,\text{mV}$, respectively, at 300 K. . 57
3.3.4 Amplitude of third-order intermodulation product at $3\omega_{LO} \pm \omega_{IF}$ versus V_{LO} (**a**) and V_{IF} (**b**) for $V_{IF} = 100\,\text{mV}$ and $V_{LO} = 100\,\text{mV}$, respectively, at 300 K. . 57
3.3.5 Amplitude of the intermodulation product at $\omega_{LO} \pm \omega_{IF}$ versus V_{LO} (**a**) and V_{IF} (**b**) for $V_{IF} = 100\,\text{mV}$ and $V_{LO} = 100\,\text{mV}$, respectively, at 4 K. 58
3.3.6 Amplitude of the third-order intermodulation product at $3\omega_{LO} \pm \omega_{IF}$ versus V_{LO} (**a**) and V_{IF} (**b**) for $V_{IF} = 100\,\text{mV}$ and $V_{LO} = 100\,\text{mV}$, respectively, at 4 K. 58
3.3.7 Amplitude of the third-order intermodulation product at $\omega_{LO} \pm 3\omega_{IF}$ versus V_{LO} (**a**) and V_{IF} (**b**) for $V_{IF} = 100\,\text{mV}$ and $V_{LO} = 100\,\text{mV}$, respectively, at 4 K. 59
3.3.8 Amplitude of third order intermodulation product versus input voltage sweep V_{LO} 62
3.3.9 Amplitude of third order intermodulation product versus input voltage sweep V_{IF} 62
3.3.10 Amplitude of third order intermodulation product versus input voltage sweep V_{LO} 63
3.3.11 Amplitude of third order intermodulation product versus input voltage sweep V_{LO} 63
3.3.12 Amplitude of third order intermodulation product versus input voltage sweep V_{IF} 63
3.3.13 Amplitude of third order intermodulation product versus input voltage sweep V_{LO} 64
3.3.14 Analytical and simulated SFDR vs R_1 at $300K$ (**a**), or Analytical and simulated SFDR vs R_2 at $300K$ (**b**) 64
3.3.15 Analytical and simulated SFDR vs R_1 at $4K$ (**a**), or Analytical and simulated SFDR vs R_2 at $4K$ (**b**) 65
3.3.16 Analytical and simulated SFDR vs $R_1 = R_2 = R$ at 300 K (**a**) and 4 K (**b**) . 65
3.4.1 Jones schematic 67
3.4.2 Representation of differential output current at load of circuit 3.4.1 68

3.5.1 Jones schematic implemented using IHP technology 70

4.1.1 Test implementation 77
4.1.2 Output Gain versus f_{RF} frequency 78
4.1.3 1dB-Compression Point curves compared at 4K and 300K 79
4.1.4 IIP3 curves at 300 K (**a**) and 4 K (**b**) 79
4.2.1 NF SSB compared to DSB for 300K and 4K model. The value is much higher than 1 dB because the gain is lower than 0dB 81
4.3.1 300 K Port isolation between each port configuration 82
4.3.2 4 K Port isolation between each port configuration 82
4.3.3 300 K Output signal at each port. The y label P1-P2 refer respectively for input port where we inject signal, and output port in which we plot the signal 83
4.3.4 4 K Output signal at each port. The y label P1-P2 refer respectively for input port where we inject signal, and output port in which we plot the signal . . 83

A.0.1 Schematic 87

List of Tables

1.1 Summary of the main electrical parameters of the cryogenic devices analyzed. 18
1.2 HBT parameters at different temperature. **m1** refer to the number of emitter, the effectively area emitter is defined as $m1 \times W \times L$ 19
1.3 Specific values of η_C. 22

2.1 Circuit parameters at different temperature. 35
2.2 Harmonic amplitudes — Analytical (Taylor) model 35
2.3 Knee voltage estimated by the analytical Taylor-based model. 37
2.4 Tones of the FFT Matlab spectrum 38
2.5 Harmonic amplitudes — Circuit Model 39
2.6 Overall comparison with relative error for the tones evaluated at 300 K and 4 K 39
2.7 Harmonic amplitudes - 300k values with transconductance value equal to the one at 4K 40

3.1 Resistors and capacitors at RT and CT 53
3.2 Bias voltages at RT and CT and tail currents 53
3.3 Transistor sizes. m1 refer to the number of emitter, the effectively area emitter is defined as m1$\times W \times L$ 53
3.4 Calculated tone amplitudes at 300 K for sweeping V_{LO} and $V_{IF} = 100mV$ . . 54
3.5 Calculated tone amplitudes at 300 K for sweeping V_{IF} and $V_{LO} = 100mV$ . . 54
3.6 Calculated tone amplitudes at 4 K for sweeping V_{LO} and $V_{IF} = 100mV$ . . . 54
3.7 Calculated tone amplitudes at 4 K for sweeping V_{IF} and $V_{LO} = 100mV$ . . . 55
3.8 Simulated tone amplitudes at 300 K for sweeping V_{IF} and $V_{LO} = 100\,\mathrm{mV}$ . . 55
3.9 Simulated Tone amplitudes a 300 K for sweeping V_{IF} and $V_{LO} = 100\,\mathrm{mV}$ . . 55
3.10 Simulated tone amplitudes at 4 K for sweeping V_{LO} and $V_{IF} = 100\,\mathrm{mV}$ . . . 56
3.11 Simulated tone amplitudes at 4 K for sweeping V_{IF} and $V_{LO} = 100\,\mathrm{mV}$ . . . 56
3.12 SFDR from analytical model 66
3.13 SFDR from circuit simulation 66

3.14 Transistor sizes for different temperature. n_1 define the number of gates in the MOS, instead, m_1 the number of emitter 70
3.15 Circuit bias for different temperature. 70
3.16 Input signals for different temperature. 71
3.17 Amplitudes calculated from the analitical model. 71
3.18 Amplitude from the circuit simulation 72
3.19 Comparison between analytical and simulated amplitudes 72
3.20 Comparison of SFDR. 73
3.21 SFDR extrapolated from the analytical model of the multiplier for $V_{IF} = V_{LO} = 100mV$ (see Tables 3.4-3.7). 74
3.22 SFDR obtained from the analytical model of the switching mixer for $V_{IF} = V_{LO} = 100mV$. 74
3.23 SFDR extrapolated from the simulated model of the multiplier for $V_{IF} = V_{LO} = 100mV$ (see Tables 3.8-3.11). 74
3.24 SFDR extrapolated from the simulated model of the switching mixer for $V_{IF} = V_{LO} = 100mV$. 75

4.1 Circuit parameters for AC simulations. 78
4.2 Table 1dB compression point values at 300 K and 4 K 79
4.3 IIP3 at 4 K and 300 K 80
4.4 Simulated and analytical IIP3 values at 300 K and 4 K 80

Artificial intelligence tools were only used to improve the English grammar, vocabulary, and formal style of this thesis. All concepts, mathematical derivations, simulations, analyses, and results were developed independently by the author.

Introduction

Quantum computing sound nowadays like a promising archetype for a new computation era. At the core of a quantum processor is an array of two-state physical microsystem, dubbed quantum bits (qubits), kept at cryogenic temperature (tipically tens of mK) for preserving quantum coherence and controlled and read-out by classical mixed-signal and radiofrequency integrated electronics [1][2]. Unlike classical bits, qubits can assume quantum states superposition of their two canonical states. This paves the way to a logic free from the third excluded and the no-contradiction principles to which the classical algorithms must obey. This quantum logic makes possible the conceiving of a new class of algorithms (quantum algorithms) to which several high-tech companies, active in fields spanning from information technologies to pharmaceutics, look with great interest for solving a speeding-up mathematical tasks of pratical interest [1][3][4]. Aim of this thesis is investigating non-linear integrated circuits (mixer and multiplier) able to operate frequency conversions, processes largely used in controlling and reading-out qubits. This circuits are sources of several noise and nonlinear effects that, in a quantum computer, could result in unwanted operations on qubits or readout errors. The main purpose of this thesis is to realize a structure that relies on a very high SFDR (Spurious-Free Dynamic Range) and high linearity, and to compare it with other structures.

The thesis is organised as follows; First, we introduce the theorethical background on Radio Frequency Integrated Circuit (RFIC), electronics devices, the application for control and read-out in Quantum computing and how they behaves in a cryogenic environment, introducing also the concept of Qubit. The analysis then focuses on the degenerated differential couple circuit, that constitute the main block of the Gilbert multiplier. A mathematical large-signal description is provided and validated with Cadence simulation. Subsequently, the Gilbert multiplier is investigated analytically. The spectral response is examined by evaluating the amplitude of the principal output frequency component, harmonic and intermodulation products, and the SFDR. Then, the performance are compared with a classical Jones demodulator topology. Finally, the main Figure of Merits (FoM) of the Gilbert multiplier are extracted and discussed in order to provide a complete assesment of its performance. All simulation and analyses are conducted at both CT and RT, allowing the influence on temperature to be evaluated.

1 Cryogenic RFIC for quantum technologies

1.1 RFIC front-ends

Radio-Frequency Integrated Circuits (RFICs) are a class of integrated circuit specifically designed to operate at radio frequencies. They are a fundamental part of modern wireless systems, supporting functions such as signal reception, transmission, frequency conversion, and frequency synthesys [5].

RFICs are typically organized into a set of functional blocks that together implement the radio front-end. More specifically, RFICs are commonly distributed in receiver and transmitter front-ends, which are distinct chains with different purposes. The Low-Noise Amplifier (LNA) at the receiver input amplifies the incoming signals, preserving the Signal-to-Noise Ratio (SNR) as much as possible. Mixers are used to translate signals between different frequency bands by combining them with a Local Oscillator (LO), enabling both downconversion and upconversion. The frequency synthesys, often based on a Voltage-Controlled Oscillator (VCO) closed in a Phase-Locked Loop (PLL), generates the LO frequency. In transmission, a Power Amplifier (PA) provides the output power required to propagate the signal over a given distance.

Depending on the architecture, additional blocks such as filters, gain-control circuits, and buffers may also be included to improve selectivity, isolation, and dynamic range. Their design must account for impedence matching, noise, linearity, stability, and parasitics, all of which strongly influence overall performance.
Most common receiver architectures can be classified according to RF signal being translated to Base-Band (BB) or to an Intermediate Frequency (IF). Each architecture exhibits trade-off among selectivity, image rejection, DC-offset sensitivity, and implementation complexity.

- Superheterodyne is a two-step receiver architecture. Figure 1.1.1 shows that the LNA pass to an Image Reject Filter an amplified version of the RF signal (picked up by the antenna). Since the signals own hermitian symmetry , this filter for $f_{LO} < f_{RF}$ ($f_{LO} > f_{RF}$) the positive (negative) frequency spectral component of the radio frequency signal overlaps with the negative (positive) frequency spectral component of the Image frequency signal.

Then, a mixer downconvert the RF signal to a fixed (IF) frequency. Eventually, an I/Q demodulator, composed by two mixers each followed by a low pass filter, solves theincoming composite IF signal into its in-phase (I) and in quadrature (Q) components (constellation). In a superheterodyne receiver, the IF choice creates a trade-off between image rejection and channel selectivity. A higher IF pushes the image farther away from the desired RF signal, which makes the image-reject filter easier to design, but it also makes the channel-select filter at IF harder to realize because it needs a higher Q. At a lower IF, the channel-select filter can be much sharper and more practical, but the image frequency moves closer to the wanted signal, so the front-end image-reject filter must become much more selective [6];

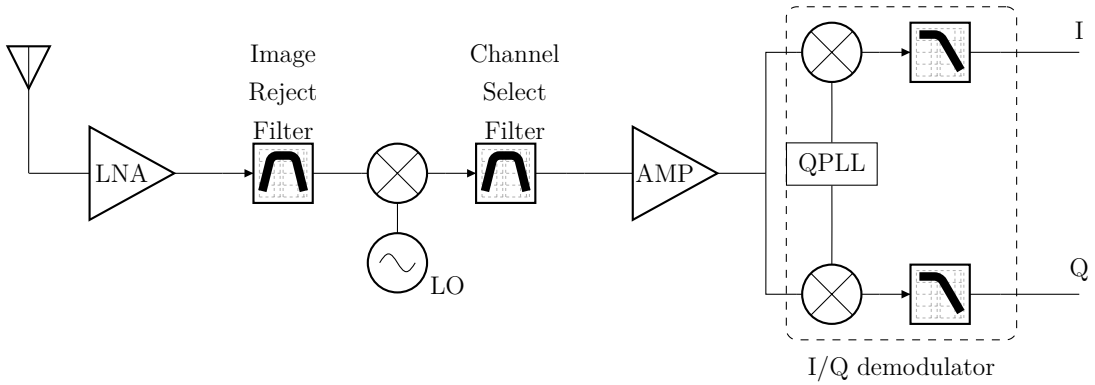


Figure 1.1.1: Superheterodyne receiver

- Heterodyne is a single-step architecture composed by an LNA and an I/Q demodulator, so in this way Image Rejection filter and Channel selection filter are no longer needful. Since the intermediate-frequency stage is removed, the architecture is compact and well suited for integration. However, it is sensitive to DC offsets, LO leakage, flicker noise, and I/Q imbalance [7];

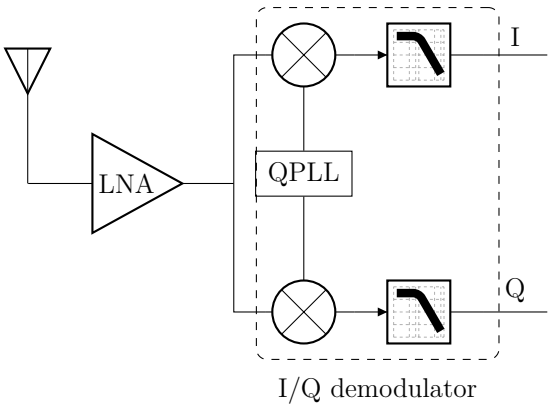


Figure 1.1.2: Heterodyne receiver

- Hartley is an interferometric architecture designed so that the radiofrequency (image frequency) signals is splitted in two branches and recombined with constructive (destructive) interference at the output. The structure is similar to the heterodyne receiver but the use of quadrature filter in the upper branches, which is critical, because its impulsive response is anticausal. The Hartley receiver avoids the need for a highly selective image filter, but its performance depends strongly on the accuracy of the quadrature network and is therefore affected by I/Q mismatch [8];

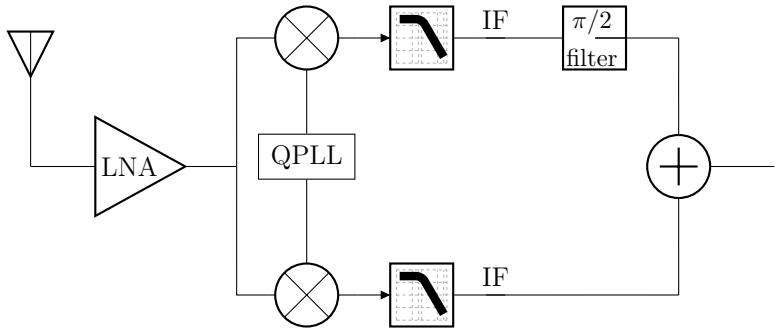


Figure 1.1.3: Hartley receiver [8]

- Weaver is also an interferometer architecture. Its advantage over the Hartley receiver is that it replaces the need of a quadrature filter by a second quadrature PLL at the cost of a higher complexity and power consumption [9].

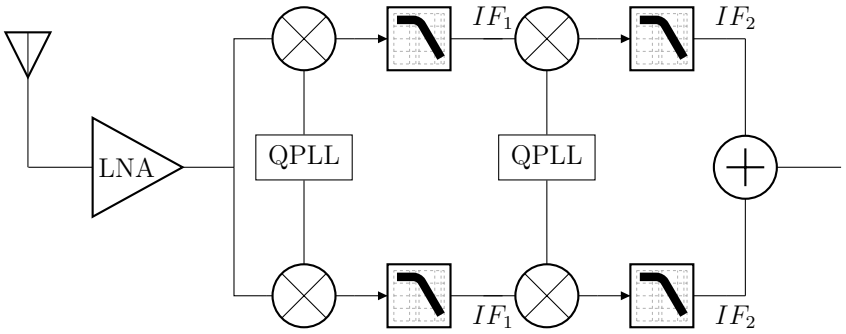


Figure 1.1.4: Weaver receiver [9]

Transmitter architectures can also be classified according to the number of frequency-translation stages employed to move the signal from baseband or intermediate frequency to the final RF band. As in the receiver case, each solution represents a different compromise among implementation complexity, spectral purity, power consumption, and susceptibility to oscillator leakage or pulling.

- Direct transmitter is the dual circuit of the homodyne receiver. It is composed by an I/Q modulator whose output signal is recombined after a filtering and then provided to a Power Amplifier. In general, transmitter design is driven by the need of high spectral purity and efficiency while minimizing leakage, distortion, and power consumption. Since PA and PLL operates at the same frequency, the strong output modulated signal may induce frequency pulling in the PLL [10];

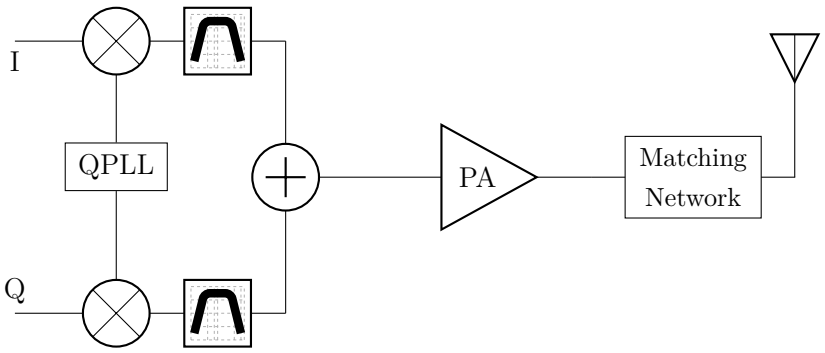


Figure 1.1.5: Direct transmitter

- Two-step transmitter is similar to the Direct transmitter. It uses an I/Q modulator, but in this case the output frequency is not an RF, but an IF frequency. After the recombination of the signal into a summing node, an upconversion mixer shifts the signal to the RF before the PA amplification. Since PA and PLL operates at different frequency this architecture avoids the pulling effect even if this may occurs if IF is chosen too low [11];

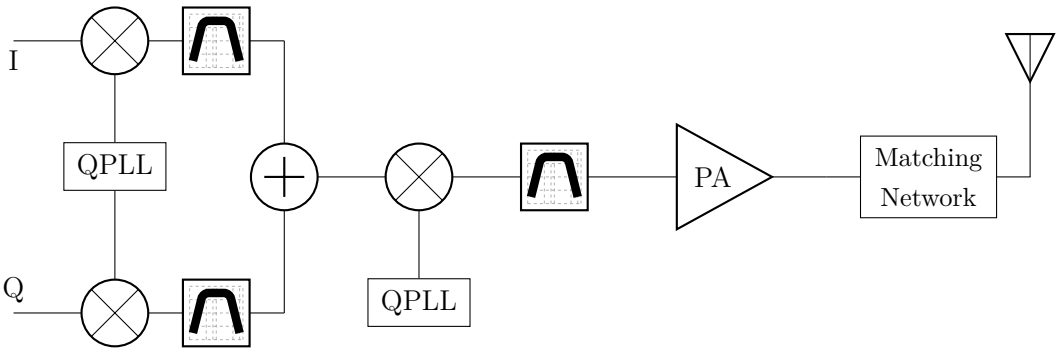


Figure 1.1.6: Two-Step transmitter

- Offset VCO transmitter exploits the same logic of a Direct transmitter, with the only difference that LO signal for the I/Q modulator is obtained by beating two LO frequencies. In this way, again, the pulling effect is avoided because because PA and PLL's operate at different frequencies [12].

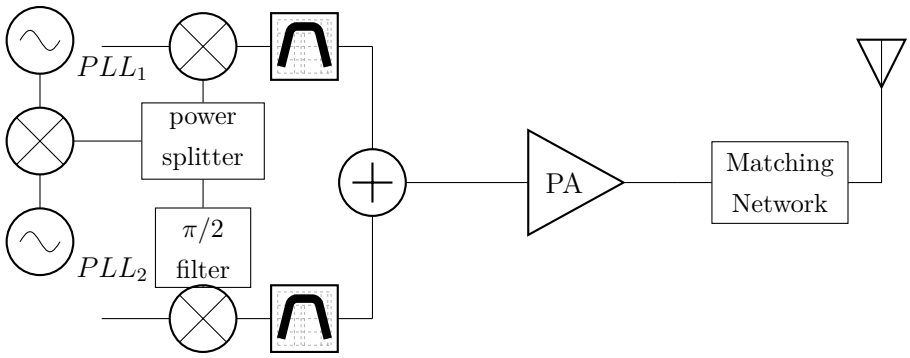


Figure 1.1.7: Offset VCO transmitter

Another relevant way to classify transmitter architectures is based on the sideband structure of the generated signal. In particular, modulation can be implemented either as Single Side Band (SSB), where only one sideband of the spectrum is transmitted, or Double Side Band (DSB), where both sidebands are present, thus requiring approximately twice the bandwidth compared to SSB. DSB modulators are generally simpler to implement but require larger bandwidth, because the energy is distributed over both sidebands. Conversely, SSB modulation is more frequency-efficient since it locates the signal energy into a single sideband; however, it comes at the cost of increased implementation complexity [13]. In practice, SSB transmitters demand either highly selective filtering or precise interferometer architecture to effectively suppress the unwanted sideband. An example of a SSB interferometric transmitter is reported in Figure 1.1.8.

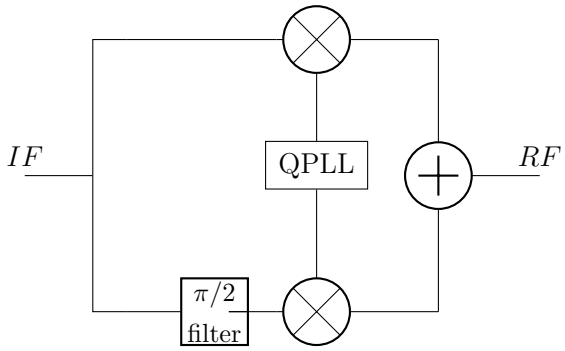


Figure 1.1.8: SSB transmitter [14]

All the previous transmitter and receiver architectures have been used for a long time in the telecommunications devices. In the framework of a Quantum Processor Unit (QPU) they serves for controlling and reading-out qubits. In the readout chain of a quantum computer, RFIC receivers enable the measurement of the qubit state via a reflected signal whose phase carries information about the state of the qubit.

At this stage, low-noise RF front-ends are critical, as the readout signal is typically very weak and must be processed without degrading the information encoded in its phase. In the control chain an RFIC SSB transmitter allows to excite a single qubit without exciting the "image qubit".

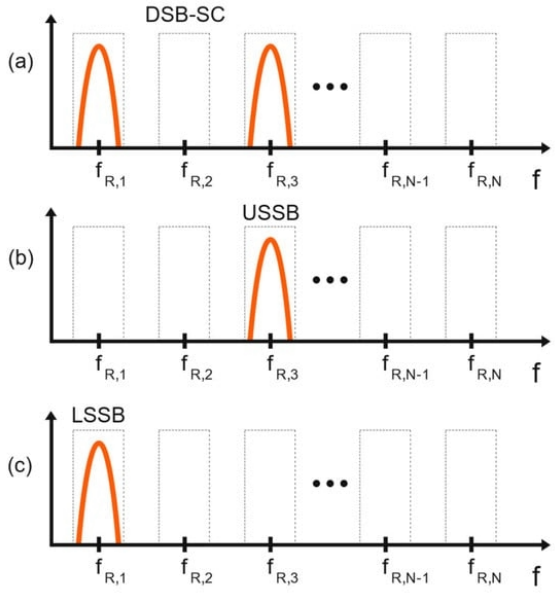


Figure 1.1.9: Representation of a Quantum microprocessor as an array of N resonance frequencies (reported as $f_{R,i}, \quad i \in [1, N]$) and microwave pulse spectra (red curve) for a DSB-SC (**a**), USSB (**b**) and LSSB (**c**) modulation architecture [14, 15]

Generally speaking, the RF spectrum generated by the SSB transmitter should be as clear as possible, in order to avoid unwanted excitations of other qubits in the array [1]. To this aim, the Figure 1.1.9 shows that a central role is played by the linearity of the mixers (see Section 1.2). Power contraints are forced by the cryogenic operation environment (4 K), where the RFIC circuitry should operate so that to be as close as possible to the qubit array. The power dissipated by the RFIC circuitry be indeed compliant with the cryostat power budget. Neverthless, at cryogenic temperature charge carrier transport, voltage threshold, and mobilities are affected strongly, making mandatory the investigation of the electronics devices in the cryogenic regime (see Section 1.3) [16].

The Qubit

Being a two canonical state quantum microsystem, quantum bit can be represented by a state vector $|\phi\rangle$ defined as

$$|\phi\rangle = \alpha|0\rangle + \beta|1\rangle, \tag{1.1.1}$$

where the two canonical state $|0\rangle$ and $|1\rangle$ are the orthonormal basis vectors of the Hilbert space, while α and β are complex coefficients, described probability amplitudes, satisfying the constraints:

$$|\alpha|^2 + |\beta|^2 = 1. \tag{1.1.2}$$

This equation describes the superposition of the two basis states and represents one of the fundamental differences between quantum and classical information. Upon measurement, the qubit collapses probabilistically to either $|0\rangle$ or $|1\rangle$, with probabilities $|\alpha|^2$ and $|\beta|^2$, respectively. A single qubit can be parameterized by two angles, θ and ϕ, and represented geometrically on the Bloch sphere depicted in Figure 1.1.10. Up to an irrelevant global phase, the qubit state can be written as

$$|\psi\rangle = \cos\left(\frac{\theta}{2}\right)|0\rangle + e^{j\phi}\sin\left(\frac{\theta}{2}\right)|1\rangle. \tag{1.1.3}$$

The physical state of a qubit is unchanged by a global phase factor, meaning that the vectors $|\psi\rangle$ and $e^{j\phi}|\psi\rangle$ describe the same quantum state. Therefore, only the relative phase between basis states has physical significance. In the Bloch sphere representation, the north and south poles represent respectively $|0\rangle$ and $|1\rangle$, while every point on the surface of the sphere corresponds to a possible pure qubit state. More generally, the Bloch sphere provides a one-to-one representation of pure qubit states up to a global phase, whereas mixed states are represented by points inside the sphere [17].

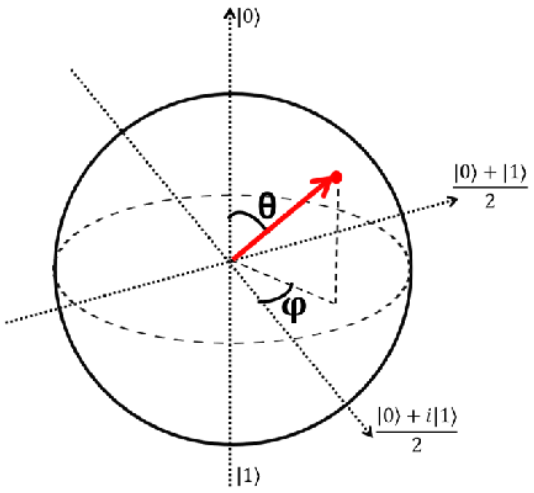


Figure 1.1.10: Bloch sphere representation

Single-qubit operations can be visualized as rotations on the Bloch sphere.

This provides an intuitive representation of quantum control and state manipulation, and also has physical meaning when the control is implemented through electromagnetic signals driving transitions between quantum states.

A more general description of a qubit is given by the density matrix formalism, which is particularly useful when the system is not perfectly isolated or when statistical mixtures must be considered. In this representation, both the state populations and the coherences are explicitly captured. For a pure state, the density matrix can be written as

$$\rho = |\psi\rangle\langle\psi| \tag{1.1.4}$$

while more general mixed states are represented as statistical ensembles of pure states. In the case of a single qubit, the density matrix formalism is especially convenient because it allows the distinction between pure states, which lie on the surface of the Bloch sphere, and mixed states, which occupy its interior[17]. In practical systems, qubit states are often affected by decoherence and environmental noise, so the pure-state description is an idealization that is valid only under limited conditions. This makes the density matrix a natural tool to describe decoherence and loss of quantum coherence in realistic systems.

A practical realization of a qubit can be obtained by means of anharmonic LC resonator. When the circuit is cooled down to cryogenic temperatures, its energy levels results quantized, and not equally spaced. The two lowest energy levels are tipically used to encode a quantum state as $|0\rangle$ or $|1\rangle$ [1]. In this circuit Quantum Electron Dynamic (c-QED) framework, a dedicated electronic system for control and readout must be able to perform single- and multi-qubit operations as well as measurements [1]. As the number of qubits in quantum processors continues to grow rapidly, the complexity of the control and readout infrastructure increases accordingly, making scalability a central design issue. In physics laboratories, the control of superconducting qubits is usually implemented through carefully shaped microwave pulses generated at room temperature and delivered to the cryogenic processor through an appropriate transmission chain. In an engineering perspective, an alternative and more scalable solution is needful and if claims the use of integrated circuitry.

In the context of qubit control and readout, the adoption of an integrated circuit rather than conventional external instrumentation is primarily motivated by the need for improved scalability, reduced power dissipation, and better thermal management. As quantum processors evolve toward larger qubit counts, the use of room-temperature bench equipment becomes increasingly impractical due to the large number of microwave lines required, the associated wiring complexity, and the excessive thermal load introduced into the cryogenic environment.

Each additional cable entering the cryostat not only increases the heat leak from higher temperature stages to the millikelvin region, but also complicates the system architecture and worsens the overall scalability of the setup.

By contrast, integrating control and readout functions on-chip, or in close proximity to the qubit device, allows the electronic interface to be significantly compacted and localized. This reduces the number and length of interconnects, lowers the total power required for signal delivery and processing, and mitigates parasitic losses, crosstalk, and latency. From a thermal perspective, a smaller cabling infrastructure directly translates into a reduced heat burden on the cryostat, which is essential for preserving the low-temperature conditions needed for qubit operation. In addition, closer integration can improve signal integrity and enable more efficient multiplexing strategies, both of which are fundamental for scaling quantum hardware toward more complex architectures.

For these reasons, integrated cryogenic electronics represent a more suitable solution than conventional instrumentation when the objective is to build a scalable, power-efficient, and thermally sustainable quantum control platform.

The generated control signals must exhibits high precision in amplitude, phase, frequency, and time in order to selectively excite the desired transition and limit leakage or crosstalk between different qubits if the same array.

Qubit readout is commonly performed through dispersive measurement, by observing the reflection coefficient of a resonator coupled to the qubit. Reflectometry constitutes a fundamental measurement technique in microwave engineering and RF characterization, wherein an electromagnetic signal directed toward a device under test yields information about the device's electrical properties through analysis of the reflected wave [18]. The physical principle underlying reflectometry is kept on wave scattering at boundaries where electromagnetic impedance changes. This reflection coefficient, expressible as a complex quantity incorporating both amplitude and phase information, serves as the primary observable in reflectometry measurements and encodes detailed information about the device's electrical state.

$$\Gamma = \frac{Z_L - Z_0}{Z_L + Z_0} \quad \text{with} \quad Z_L \in \mathbb{C} \tag{1.1.5}$$

$|\Gamma|$ is a value between 0 and 1.
In this way, the quantum state is transformed into a measurable microwave response, and the readout chain can be interpreted as a receiver-like architecture, in which the reflected tone must be amplified, down-converted, and processed with minimal degradation[1][19].

Unlike a direct measurement of the qubit state, dispersive readout relies on the state-dependent perturbation of the resonator response, so that the information carried by the quantum system is encoded into the amplitude and phase of the outgoing microwave signal. In large-scale systems, several qubits may need to be addressed and measured simultaneously, which increases the complexity of the control and readout chain and places stringent requirements on channel isolation, linearity, and frequency planning.

Moreover, qubit states are inherently fragile and susceptible to decoherence and noise. For the addressed reasons above the electronics in the quantum processor must operate in a cryogenic environment [3][4], that forces limitation to such electronics as, for instance a reduced available power budget [18]. In addition low-noise, highly linear, and spectrally clean RF electronics is a key enabler for the advancement of superconducting quantum technologies. Challenging task for the microelectronics engineer is therefore the design of control and readout circuitry at the best compromise between the requirements claimed, on the one hand, by the cryogenic environment, and, on the other hand, by the brittle quantum nature of the qubits.

1.2 Mixer Theory

The mixer is a circuit shared by all the architectures described in Section 1.1. It is a three-port network with two input ports and one output port. For a downconversion mixer the input ports are called RF and LO; the former receives the signal to be down-converted, the latter the LO signal. The output port is called IF, where intermediate signal is present. An up-conversion mixer, instead, receives at the input port the IF signal, so the port is called IF, and the local oscillator signal at the LO-port. Its output port is the RF one where the radio frequency signal is present [5].

A mixer operates frequency translation by leveraging on two possible principles:

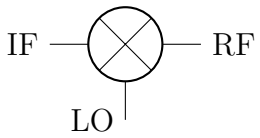


Figure 1.2.1: Upconversion mixer

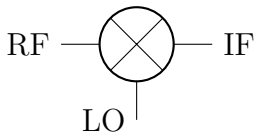


Figure 1.2.2: Downconversion mixer

- Nonlinearities: In this type of circuit the LO signal is large enough to excite the nonlinearities of the electronics circuit generating product between signals [20];

- Time-variance: the LO signal is used to periodically modulate the input signal in time exploiting switching circuitry [20].

Several mixer topologies are commonly used from an architectural standpoint, each characterized by distinct trade-offs among conversion gain, linearity, noise performance, power consumption, and implementation complexity. From an architectural standpoint, mixer topologies can also be divided according to two main criteria: passive or active devices depending on the presence or not of transistors used as amplifiers, and balance degree, ranging from unbalanced to single-balanced and double-balanced structures:

- Passive mixers are among the most frequently used solutions in modern RF integrated circuits. They are typically realized by using only transistor as switching devices driven by a sufficiently large local-oscillator signal. They do not inherently provide conversion gain. Their main advantages are low static power consumption, good linearity, and suitability for high-frequency operation. Their principal limitation is conversion loss, which often necessitates subsequent amplification stages [20].
- Active mixers incorporate amplifying transistors and can therefore provide conversion gain. This feature is especially attractive in receiver front-ends, where it helps mitigate the impact of later stages on the overall noise figure. Nevertheless, active implementations generally require more power and tend to exhibit reduced linearity compared with passive counterparts. It helps improve the overall noise figure by providing conversion gain [20];
- In Single-ended mixers all the input signals are single-ended;
- In Single-balanced mixers represent a simple alternative, usually the LO signals are differential. Its reduced complexity and lower area make it attractive in some applications; however, LO and RF port isolations is modest [20].
- In Double-balanced mixers all the input signals are differential. They are preferred when port isolation is critical. By improving the cancellation of even-order terms and undesired coupling between ports, they generally deliver superior spectral purity. This performance, however, is obtained at the cost of increased circuit complexity, larger silicon area, and, in many cases, higher LO drive requirements [20].

The selection of a mixer topology depends on the requirements of the intended RF application. The most appropriate choice is determined by the required operating frequency, available supply voltage, acceptable power budget, and the relative importance of linearity, noise, and conversion gain.

Roughly speaking the operation of a mixer can be visualized as a multiplication between two input signals [5]. The most common and attractive circuit solution is the Jones mixer

(see Figure 3.1), often confused with the Gilbert Cell (see Figure 3.4). These circuits will be discussed in Section 3.

The most important Figure of Merits (FOMs) of a Mixer are the following ones:

- Conversion Gain is the ratio between the power delivered to the load at the frequency $\omega_{IN} \pm \omega_{LO}$and the input power delivered to the mixer at the frequency ω_{IN}.
- 1dB Compression Point is the input power at frequency ω_{IN} at which the output power at frequency $\omega_{IN} \pm \omega_{LO}$ deviates of 1 dB from the linearity;
- Third order product intercept point is the input power at the input frequencies ω_{IN1} and ω_{IN2} for which the output power at the output frequencies $2\omega_{IN2} - \omega_{IN1} \pm \omega_{LO}$ equals the one at $\omega_{IN1} \pm \omega_{LO}$ and $\omega_{IN2} \pm \omega_{LO}$. It is an extrapolated power point;

Because of image frequency issue, a mixer exhibits two Noise Factor (NF):

- The Single-Side Band (SSB) NF is defined as the ratio between the total noise power at the output at IF de-embedded from the load contribution at IF and the noise at the output due to input at RF only;
- The Double-Side Band (DSB) NF is defined as the ratio between the total noise power at the output at IF de-embedded from the load contribution at IF and the noise output power at both RF and IM frequencies;
- Port isolation: it's the amount of leakage between any two mixers port.

Another key metrics important for the mixer is the SFDR (Spurious Free Dynamic Range) that describe how much the Output first order harmonic is larger than the highest higher order one. Its value is usually denoted in dBc.
To operate in cryogenic environment on qubits, the output tones generated from the mixer must have a very low noise, high SFDR and very low power consumption.

1.3 HBT SiGe 4K characterization

The bipolar junction transistor (BJT) has long served as a foundational active device in analog and RF integrated circuits due to its high transconductance, predictable exponential current-voltage relation, and favorable noise performance. It is formed by two pn junctions sharing one doped semiconductor region called base, being the other two semiconductors regions called emitter and collector. You have thus the base-emitter junction and the base-collector junction.
In its conventional Silicon implementation, the BJT is formed entirely from a single semicon-

ductor material, so that these junctions are homojunction. The charge transport in a BJT occurs essentially in three main phases. For instance, in an NPN transistor, electrons are first injected from the emitter into the base through the forward-biased base–emitter junction. They then diffuse across the base due to the charge gradient created by this injection. Once they reach the edge of the base, they are swept into the collector by the electric field in the depletion region of the reverse-biased base–collector junction. The role of the base-emitter junction is thus to launch electrons toward the base-collector junction. For this reason it is important, unlike for the pn junction in a generic diode, that the base-emitter junction emits electrons better than holes. This ability is quantified by the microscopic parameter called electron efficiency γ_E defined as the ratio between the current of electrons to the total current (electrons plus holes) flowing through the forward biased junction. It is desiderable that γ_E is close to one as much as possible. In a BJT, the main solution is to dope the emitter more heavily than the base. However, this increases the base resistivity, which in turn slows down the transistor due to the larger time constant associated with the parasitic base resistance and the base–emitter capacitance. Another solution is fabricating emitter and base with two different semiconductor. In this case the base-emitter junction is an heterojunction and the resulting transistor takes the name of Heterojunction Bipolar Transistor (HBT). In the silicon Microelectronics technology, the base is made of SiGe and the emitter of Silicon. The SiGe semiconductor exhibits a narrow bandgap than Silicon. At room temperature, Silicon has a bandgap of about 1.12 eV, while Germanium is about 0.66 eV, so a SiGe alloy lies between these two values depending on the Ge fraction[16]. The resulting bandgap discontinuity ΔE_g distributed between a discontinuity ΔE_v in the valence band and a discontinuity ΔE_c in the conduction band with $\Delta E_g = \Delta E_c + \Delta E_v$.

The interesting point is that $\Delta E_v > \Delta E_c$. In this way the heterojunction is more hard to be thermoionically overcome for the holes. The heterojunction results therefore intrinsically by nature, once forwarded biased, able to inject better electrons than holes. This brakes the trade-off between γ_E and the ratio between emitter and base doping levels, paving the way to the capability of higher doping the base layer without sacrifying γ_E. In its terms, this leads to lower base parasitic resistance, lower constant time and thus higher operation speed. Summarizing, in a SiGe bipolar transistor, this bandgap reduction is not just a material-property change; it reshapes directly carrier injection. A smaller base bandgap lowers the hole barrier at the emitter-base junction, which increases electron injection efficiency from the emitter into the base and therefore improves current gain [16]. The SiGe HBTs outperform therefore conventional silicon BJTs in high-frequency operation [21]. Using the Wentzel-Kramer-Brilluoin (WKB) approximation in the Schrodinger equation the tunneling

transmission probability is:

$$T_t = e^{-2\int_0^{x_0} k_x dx} \tag{1.3.1}$$

where x_0 is the width of the Emitter-Base depletion region, and k_x the electron-wave vector in the tunneling direction given by:

$$k_x = \sqrt{\frac{2m^* E_x}{\hbar^2}} \tag{1.3.2}$$

where E_x is the position dependent electron energy barrier for tunneling, m^* the tunneling mass, and $\hbar$ the reduced Planck's constant. In the case of a rectangular shaped potential barrier Equation 1.3.2, yields:

$$T_t \approx e^{-\frac{4\sqrt{2m^*}}{3q\hbar}\frac{E_0^{3/2}(T)}{\epsilon_{avg}(T)}} \tag{1.3.3}$$

where $\hbar$ is the reduced Planck's constant, E_0 is the electron barrier energy, m^* is the electron tunneling mass and $\epsilon_{avg}(T)$ is the effective average value of the emitter-base electric field. Equation 1.3.3 shows clearly that T_t depends on the temperature. Assuming collector current density $J_C \propto T_t$, J_C changes accordngly to the tunnelling mechanism. The equation shows also that the tunnelling probability is also exponentially proportional to the electron barrier energy at $x = 0$ (E_0). An increase of the barrier energy reduces therefore the tunnelling probability [16].

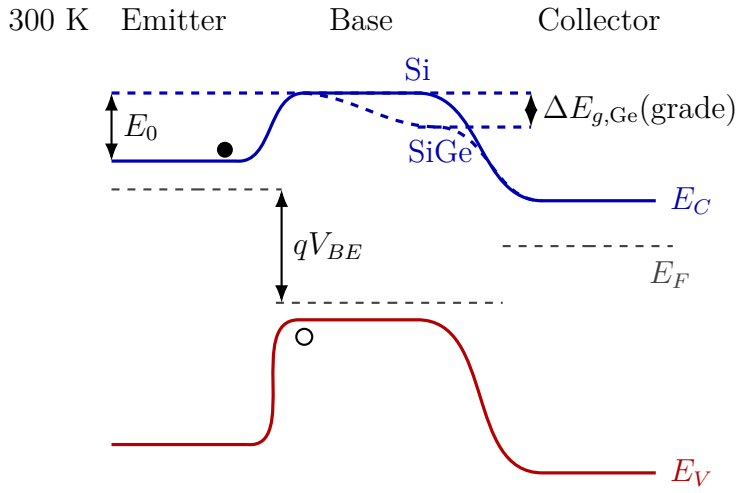


Figure 1.3.1: Qualitative band diagram of an HBT.

In the cryogenic regime, the drift–diffusion transport mechanism is strongly suppressed, because the charge carriers do not have energy enough to cross over the potential barrier at the base-emitter junction [22][16]. In advanced bipolar transistors, the base width is their enough

that at 4 K. The presence of defect related energy levels within the forbidden bandgap of the base semiconductor can sustain a flow of electrons from the emitter to the collector via the tunnelling mechanism.
At 4 K the phonon density is so low in the crystal that the elctrons do not loss energy by scattering.

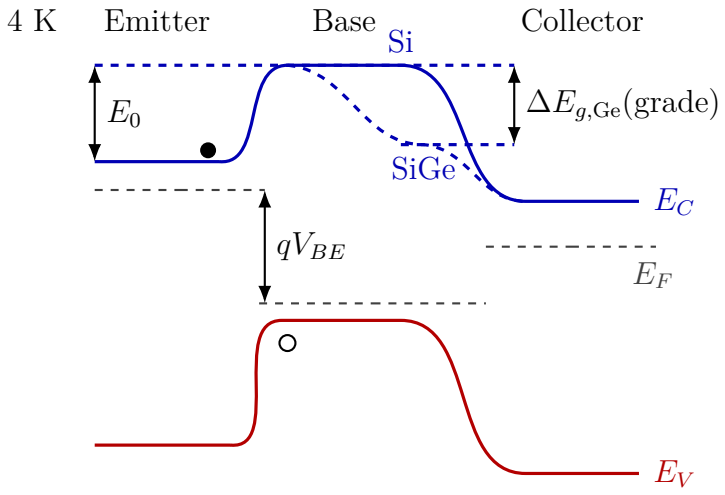


Figure 1.3.2: Qualitative band diagram of an HBT.

Table 1.1 collects the cryogenic main characteristics of SiGe HBT claimed in the literature.

Technology	Temp. [K]	$V_{BE_{ON}}$ [mV]	β_{CT}	β_{RT}	η	Kink effect	Early effect	A_E [μm^2]
130 nm SiGe BiCMOS[23]	4.3	-	3369	1000	-	-	-	-
SG13G2 IHP[24]	4	0.89	-	-	1,8538	N	N	-
IBM 5AM SiGe HBT[25]	43	-	-	-	2	Y	Y	0.5×2.5
IBM 8HP[26]	18	0.91	-	-	1.75	-	-	-
SG13G2 IHP[27]	4	0,91	2750	1000	30	N	Y	-
SSMC 160-nm 1P5M CMOS[28]	7	-	0,1	60	100	-	-	5×5
SiGe BiCMOS-8XP[29]	12	-	1250	-	96	N	N	0.12×8
NA[30]	77	1,02	0,2	3	-	N	Y	0.46×0.46
NA[31]	2	0,95	10000	-	-	Y	N	0.1×4.5
SG13G2 IHP[32]	10	0,9125	50000	8000	10	N	Y	0.12×0.96
Mextram 504.6 and VBIC[33]	93,15	1,2	200	200	7,25	N	Y	-
HBT0.8[34]	4	-	30	70	-	Y	N	4.8
HBT0.5[34]	4	-	1000	200	-	-	-	2.8
IBM's SiGe 5AM[35]	1.4	-	-	-	-	N	N	0.5×2.5
NA[36] (HS)	77	-	250	200	-	N	Y	0.6×10.16
NA[36] (STD)	77	-	267	200	-	N	Y	0.6×6.0
NA[36] (HV)	77	-	250	183	-	N	Y	0.6×1.7
IBM BiCMOS-8HP[37]	15	-	8000	500	-	N	Y	18×0.12
NA[38]	84	0.8	120	95	-	N	Y	1.0×4.6
NA[39]	4.5	-	7.693	827	-	N	N	0.5×2.5

Y: means that the effect is present, *N*: means that the effect is not present,

-: means that this technology does not provide the neccessary curve to evaluate this type of information *NA*: means that the technology is not available

Table 1.1: Summary of the main electrical parameters of the cryogenic devices analyzed.

In this table $V_{BE_{ON}}$ is the turn-on voltage of the transistor at temperature Temp, β_{CT} and β_{RT} are the current gain at cryogenic and room temperature (300 K) respectively, η is the ideality factor at CT, A_E is the emitter area. The β value at CT shows an increasing respect to the RT one. This increment is linked to the doping profile induced by the germanium gradings present in the HBT ($\Delta E_{g,Ge}(grade)$) [16]. The Early effect is an effect that appear in the BJT transistor in which for a increasing of the reverse bias voltage V_{CB}, we have a reduction on the effective base width. This reduction causes a slightly increases in the current [40]. The Kink effect is an undesired device phenomenon observed in cryogenic transistors, typically below 100 K, and is often associated with high-injection conditions. In the output characteristics, it manifests as a negative differential resistance region in the I_C–V_{CE} curve, followed by an anomalous increase of the collector current I_C at a given base–emitter voltage V_{BE}. In the Gummel plot, the effect may appear as a sharp enhancement of both I_C and I_B for a fixed V_{BE}. From a physical standpoint, this behavior has been attributed to an additional drift-current contribution arising from charge accumulation and the enhanced positive feedback induced by the heterojunction barrier, which modifies carrier transport under cryogenic operation [26][16].

1.3.1 IHP HBT SG13G2

In the present work, the SiGe HBT from IHP SG13G2 130 nm BiCMOS technology has been used. Purpose of this section is to investigate by simulation the behaviour of the HBT provided by the Design kit of this technology.
Table 3.3 reports the used device parameters:

Temp [K]	W $[nm]$	L $[nm]$	m_1	V_{BE}	V_{CE}
300	900	70	7	1.2	1.2
4	900	70	7	1.2	1.2

Table 1.2: HBT parameters at different temperature. **m1** refer to the number of emitter, the effectively area emitter is defined as $m1 \times W \times L$

The simulated device features an emitter area (A_E) upscaled by a factor of 7 relative to the unit transistor. This configuration implements a parallel topology of 7 unit HBTs, maintaining unchanged current densities (J_C, J_B) and specific characteristics per unit area, while increasing the total current capability of the device.
Figures 1.3.3a and 1.3.3b depicts the Gummel plots.

At RT, both collector and base currents exhibits an almost exponential dependence on V_{BE} according to the following equations:

$$I_C = I_{CS}\left(e^{\frac{V_{BE}}{\eta_C Vth}} - 1\right) \tag{1.3.4}$$

$$I_B = I_{CS}\left(e^{\frac{V_{BE}}{\eta_B Vth}} - 1\right) \tag{1.3.5}$$

A value of η_C and η_B around 1 indicates that DD is the dominant charge transport mechanism with ideally condition of negligible recombination mechanism. A value of η_B higher than 1 suggest the presence of recombination mechanism ($\eta_B = 2$), tunneling mechanism ($\eta_B > 2$) occurring in the space-charge region of the base-emitter junction. On the other hand, a value of $\eta_C > 1$ can be justified only by involving a dominant charge transport tunneling mechanism, as described above.

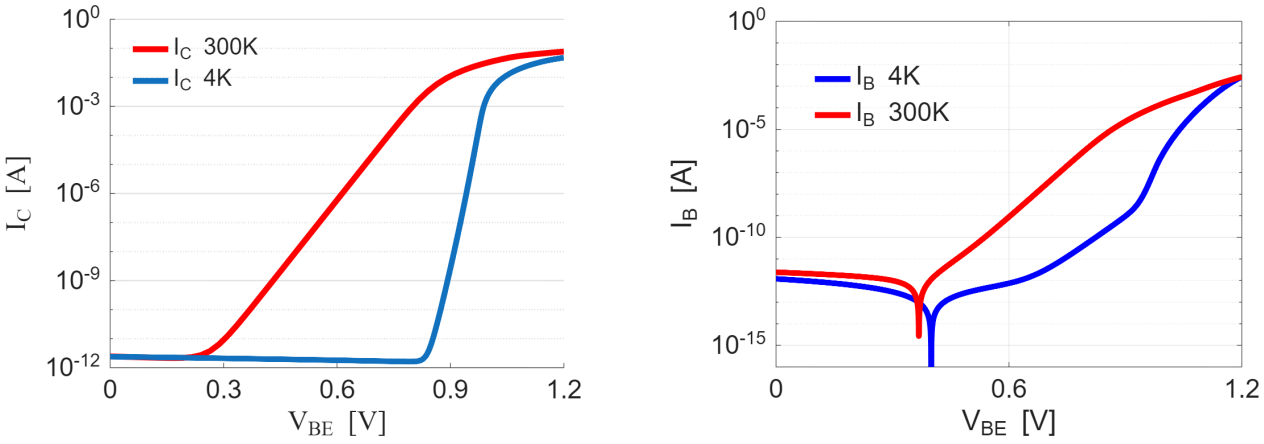


Figure 1.3.3: Simulated $I_C - V_{BE}$ (**a**) and $I_B - V_{BE}$ (**b**) plot for the HBT (IHP), for 300K and 4K.

From Figure 1.3.3a, it is evident at 4 K the increase of the turn-on voltage and of the slope of the collector current.

Figure 1.3.4 depicts the output characteristics. At $300K$ a self-heating effect is manifest. The curve shows a negative slope dependence between current and voltage in the whole temperature range simulated. In the cryogenic model, instead, self-heating effect is not present; the output I_C current is constant on the whole range of V_{CE} voltage.

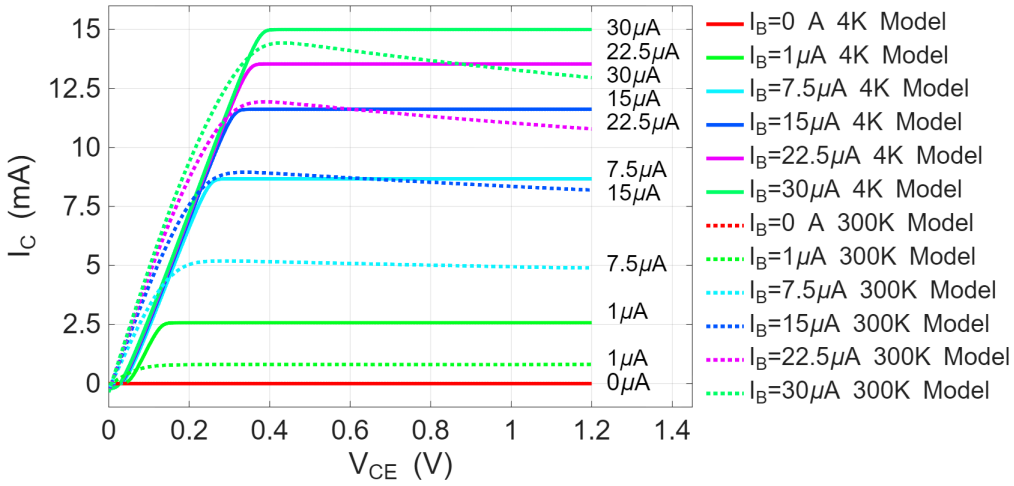


Figure 1.3.4: Output characteristics for the HBT (IHP).

Figure 1.3.5 plots β versus the collector current. At $300K$ the current is flat on the whole range of current I_C. In the cryogenic device, instead, the β gain exhibits a peak of 2680 for $I_C = 1.5mA$ ($J_C = 3.4\mu m^2$).

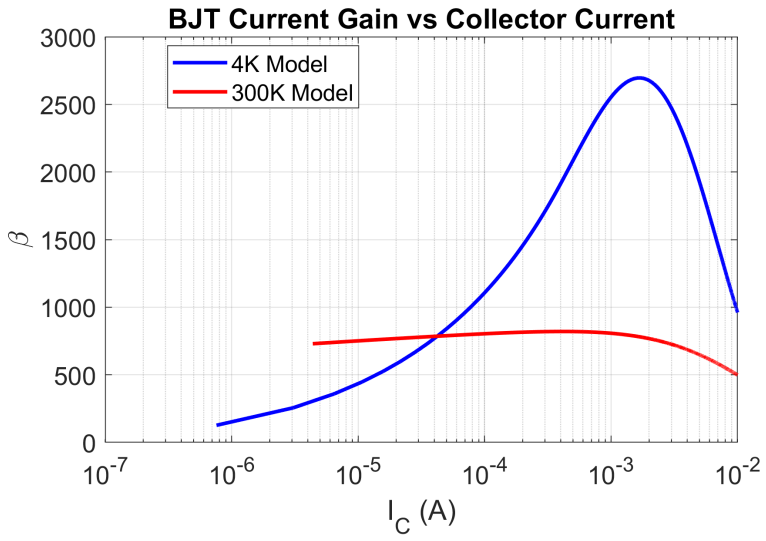


Figure 1.3.5: β plotted versus I_C for the HBT (IHP).

η parameter

From Equation 1.3.4, the ideality factor η_C can be evaluated as follows:

$$\eta_C = \frac{1}{\frac{d(\ln(I_c))}{dV_{BE}}} \frac{1}{V_{th}} \tag{1.3.6}$$

Figure 1.3.6 shows the obtained values of η:

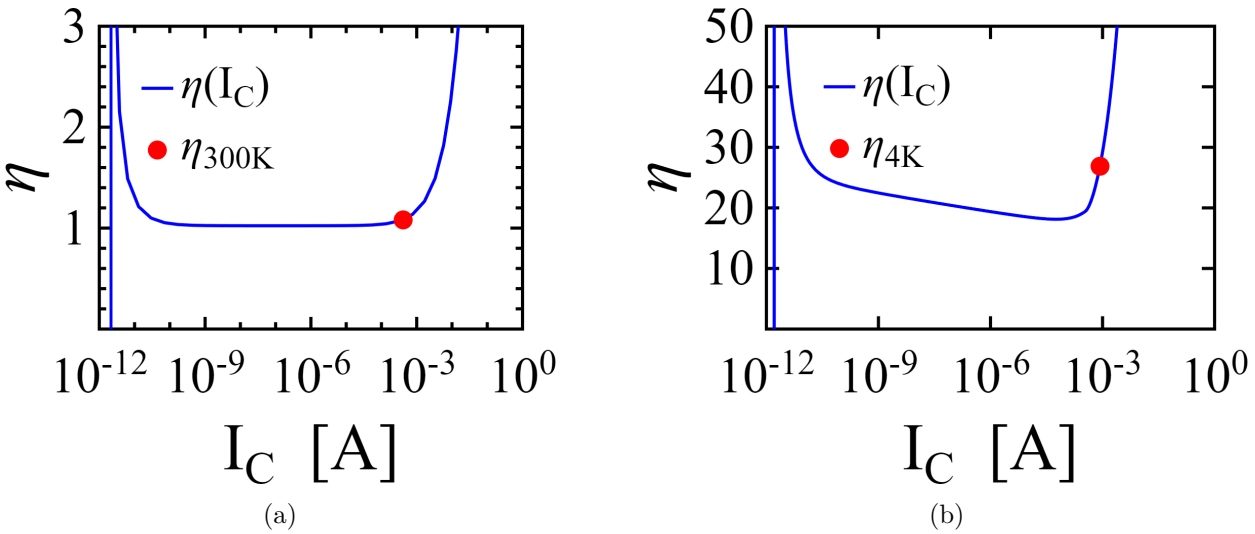


Figure 1.3.6: η_C vs I_C at 300 K (**a**) and 4 K **b**

Table 1.3 points out a couple of values of η_C obtained for a specific value of I_C

Temperature	I **[A]**	η
300 K	410×10^{-6}	1.08
4 K	850×10^{-6}	26.37

Table 1.3: Specific values of η_C.

The chosen value of collector current has to be inteded as the tail current flow in a single transistor under steady state operation, with the device parameters listed in Table 1.2. For smaller emitter area dimension, obtained by reducing the m_1 factor, the current should be scaled proportionally to preserve the same current density. The value of I_C current is chosen close to the maximum β region at 4 K device, while remaining slightly below the optimum to limit power consumption.

1.4 Cryo-CMOS differences and improvement

Cryo-CMOS refers to CMOS circuits and systems designed to operate at cryogenic temperatures, typically from 77 K down to a few Kelvin degrees, with the goal of placing classical control and readout electronics closer to quantum processors and reducing the wiring overhead between room temperature and the cold stage [41, 42].
From a circuit perspective, these changes affect key design figures of merit such as on-current, subthreshold slope, output resistance, noise performance, and power consumption, making dedicated compact models and temperature-aware design methodologies essential for reliable operation [43, 44, 45]. Despite these challenges, Cryo-CMOS is considered a promising technology for scalable quantum computing because it enables compact, low-power, and potentially monolithically integrated blocks such as low-noise amplifiers, oscillators, multiplexers, and control/readout interfaces operating in close proximity to qubits [42, 46, 47].

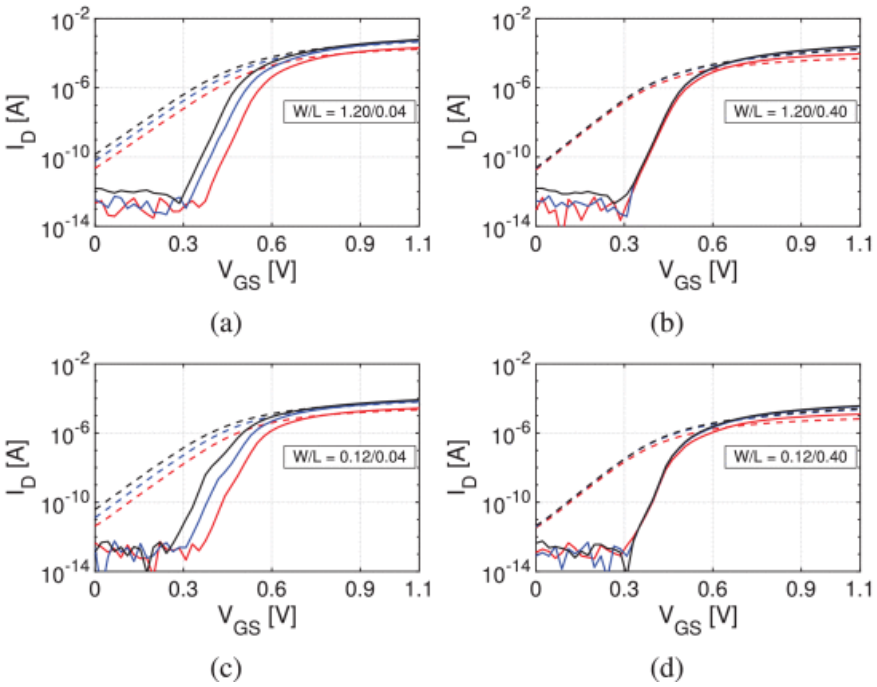


Figure 1.4.1: "Measured $I_D(V_{GS})$ characteristics of thin-oxide NMOS in 40-nm CMOS. V_{DS} = [0.1 V; 0.6 V; 1.1 V]. Solid line: 4 K; dashed line: 300 K."[48]

MOSFETs operating at cryogenic temperatures generally exhibit an increased threshold voltage and, under suitable bias conditions, a higher drain current. Their subthreshold swing decreases, while the lower off-state current reduces leakage power. In addition, their output resistance may increase, depending on the device and operating conditions. Cryogenic temperatures affects HBTs and MOSFET differently: HBTs mainly exhibit changes in current gain, whereas CMOS devices mainly show variations in mobility.

Both HBT and MOSFET exhibits an increase of the voltage required for the turning on: $V_{be,on}$ for the HBT and V_{TN}, V_{TP} for the MOSFET.

2 Analytical modelization of a degenerated differential couple

This chapter focuses on static and dynamic behavior, harmonic content, and linearity performance of the differential amplifier stage depicted in Figure 2.1.1.

2.1 DC Transfer Function

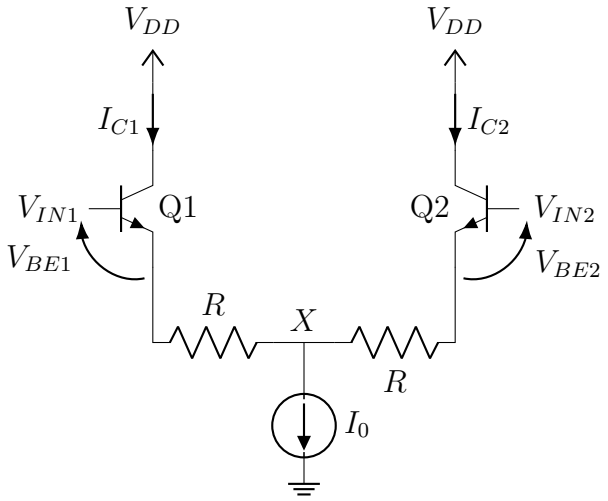


Figure 2.1.1: Differential amplifier stage

DC voltages V_{IN1} and V_{IN2} bias the two identical transistors $Q1$ and $Q2$ in the forward active region, so that you have the inequality $\frac{RI_0}{2} + V_X < V_{IN1} < V_{DD}$. The goal of the following analysis is to obtain the current-voltage transfer function which describes the dependence ofthe DC differential output current $\Delta I_{OUT} \triangleq I_{C2} - I_{C1}$ on the DC differential input voltage $V_{IN} \triangleq V_{IN1} - V_{IN2}$.
The following DC transcharacteristic of the BJT (Bipolar Junction Transistor), is the starting point of the analysis:

$$I_C = I_{sc}\left(e^{\frac{V_{BE}}{\eta V_{th}}} - 1\right) \approxeq I_{sc}e^{\frac{V_{BE}}{\eta V_{th}}} \tag{2.1.1}$$

where η is the ideality factor, I_{sc} the saturation current, V_{th} the thermal voltage defined as $V_{th} = \frac{K_B T}{q}$ where K_B is the Boltzmann constant, q the charge of the electrons and T is the absolute temperature in Kelvin $[K]$.

From Figure 2.1.1, by assuming $I_E = I_C$, the V_{BE1} and V_{BE2} voltages can be expressed as follows:

$$V_{BE1} = V_{IN1} - (R \cdot I_{C1} + V_X) \tag{2.1.2}$$

$$V_{BE2} = V_{IN2} - (R \cdot I_{C2} + V_X) \tag{2.1.3}$$

The substitution of Equations (2.1.2) and (2.1.3) into Equation(2.1.1) yields:

$$I_{C1} = I_{sc} e^{\frac{V_{IN1} - (R \cdot I_{C1} + V_X)}{\eta V_{th}}} \tag{2.1.4}$$

$$I_{C2} = I_{sc} e^{\frac{V_{IN2} - (R \cdot I_{C2} + V_X)}{\eta V_{th}}} \tag{2.1.5}$$

Due to the assumption $I_E = I_C$, we can also observe that $I_0 = I_{C2} + I_{C1}$, and we can normalize each collector current respect to I_0:

$$\frac{I_{C1}}{I_0} = \frac{I_{C1}}{I_{C1} + I_{C2}} = \frac{I_{sc} e^{\frac{V_{IN1} - (RI_{C1} + V_X)}{\eta V_{th}}}}{I_{sc} e^{\frac{V_{IN1} - (RI_{C1} + V_X)}{\eta V_{th}}} + I_{sc} e^{\frac{V_{IN2} - (RI_{C2} + V_X)}{\eta V_{th}}}} \tag{2.1.6}$$

$$\frac{I_{C2}}{I_0} = \frac{I_{C2}}{I_{C1} + I_{C2}} = \frac{I_{sc} e^{\frac{V_{IN2} - (RI_{C2} + V_X)}{\eta V_{th}}}}{I_{sc} e^{\frac{V_{IN1} - (RI_{C1} + V_X)}{\eta V_{th}}} + I_{sc} e^{\frac{V_{IN2} - (RI_{C2} + V_X)}{\eta V_{th}}}} \tag{2.1.7}$$

and by simplifying by I_{sc}:

$$\frac{I_{C1}}{I_0} = \frac{e^{\frac{V_{IN1} - (RI_{C1} + V_X)}{\eta V_{th}}}}{e^{\frac{V_{IN1} - (RI_{C1} + V_X)}{\eta V_{th}}} + e^{\frac{V_{IN2} - (RI_{C2} + V_X)}{\eta V_{th}}}} \tag{2.1.8}$$

$$\frac{I_{C2}}{I_0} = \frac{e^{\frac{V_{IN2} - (RI_{C2} + V_X)}{\eta V_{th}}}}{e^{\frac{V_{IN1} - (RI_{C1} + V_X)}{\eta V_{th}}} + e^{\frac{V_{IN2} - (RI_{C2} + V_X)}{\eta V_{th}}}} \tag{2.1.9}$$

The mathematical expression for $\frac{\Delta I_{OUT}}{I_0}$ is thus:

$$\frac{I_{C1} - I_{C2}}{I_0} = \frac{\Delta I_{OUT}}{I_0} = \frac{I_{C1}}{I_0} - \frac{I_{C2}}{I_0} = \frac{e^{\frac{V_{IN1} - (RI_{C1} + V_X)}{\eta V_{th}}} - e^{\frac{V_{IN2} - (RI_{C2} + V_X)}{\eta V_{th}}}}{e^{\frac{V_{IN1} - (RI_{C1} + V_X)}{\eta V_{th}}} + e^{\frac{V_{IN2} - (RI_{C2} + V_X)}{\eta V_{th}}}} \tag{2.1.10}$$

By gathering the term $e^{\frac{V_{IN2}-(RI_{C2}+V_X)}{\eta V_{th}}}$, we obtain the following mathematical expression:

$$\frac{\Delta I_{OUT}}{I_0} = \frac{e^{\frac{V_{IN1}-V_{IN2}-(RI_{C1}-RI_{C2})}{\eta V_{th}}} - 1}{e^{\frac{V_{IN1}-V_{IN2}-(RI_{C1}-RI_{C2})}{\eta V_{th}}} + 1} \tag{2.1.11}$$

$$= \frac{e^{\frac{\Delta V_{IN}-(R\Delta I_{OUT})}{\eta V_{th}}} - 1}{e^{\frac{\Delta V_{IN}-R\Delta I_{OUT}}{\eta V_{th}}} + 1} = \frac{e^{\frac{\Delta V_{IN}-R\Delta I_{OUT}}{2\eta V_{th}}} - e^{-\frac{\Delta V_{IN}-R\Delta I_{OUT}}{2\eta V_{th}}}}{e^{\frac{\Delta V_{IN}-(R\Delta I_{OUT}}{\eta V_{th}}} + e^{-\frac{\Delta V_{IN}-R\Delta I_{OUT}}{2\eta V_{th}}}} \tag{2.1.12}$$

and thus by reminding that $\frac{e^x-e^{-x}}{e^x+e^{-x}} \triangleq \tanh(x)$, we can put the final Equationin the following form:

$$\Delta I_{OUT} = I_0 \tanh\left(\frac{\Delta V_{IN} - R\Delta I_{OUT}}{2\eta V_{th}}\right) \tag{2.1.13}$$

Reminding that the term ΔI_{OUT} is a function of ΔV_{IN} it may be useful rewriting the Equation (2.1.13) as follows:

$$\Delta I_{OUT} = I_0 \tanh\left[\frac{\Delta V_{IN} - R\Delta I_{OUT}\left(\Delta V_{IN}\right)}{2\eta V_{th}}\right] \tag{2.1.14}$$

Equation (2.1.13) is a trascendent Equationin the argument ΔI_{OUT} It is without closed form solution and it can be solved by numerical iteration only. Neverthless, it is a typical Fermi problem[49] and thus we can spend effort to going on an approximated closed form solution by applying a Taylor series expansion whose general form is:

$$f(x) \triangleq \sum_{n=0}^{\infty} \frac{f^{(n)}(x_0)}{n!}(x - x_0)^n \tag{2.1.15}$$

where the $f^{(n)}(x_0) = \left.\frac{df^{(n)}(x)}{d\Delta V_{IN}}\right|_{x=x_0}$. For sake of simplicity, we choose to stop the expansion at the third order:

$$\Delta I_{OUT} \approx \Delta I_{OUT}(\Delta V_{IN} = \Delta V_{IN0}) + \left.\frac{d\Delta I_{OUT}}{d\Delta V_{IN}}\right|_{\Delta V_{IN}=\Delta V_{IN0}} (\Delta V_{IN} - \Delta V_{IN0}) \tag{2.1.16}$$

$$+ \frac{1}{2}\left.\frac{d^2\Delta I_{OUT}}{d\Delta V_{IN}^2}\right|_{\Delta V_{IN}=\Delta V_{IN0}} (\Delta V_{IN} - \Delta V_{IN0})^2 + \frac{1}{6}\left.\frac{d^3\Delta I_{OUT}}{d\Delta V_{IN}^3}\right|_{\Delta V_{IN}=\Delta V_{IN0}} (\Delta V_{IN} - \Delta V_{IN0})^3$$

In particular we desire to calculate this series by expanding around the origin, so that we have $\Delta V_{IN0} = 0$:

$$\Delta I_{OUT} \approx \Delta I_{OUT}(\Delta V_{IN} = 0) + \left.\frac{d\Delta I_{OUT}}{d\Delta V_{IN}}\right|_{\Delta V_{IN}=0} \Delta V_{IN} + \frac{1}{2}\left.\frac{d^2\Delta I_{OUT}}{d\Delta V_{IN}^2}\right|_{\Delta V_{IN}=0} \Delta V_{IN}^2 + \frac{1}{6}\left.\frac{d^3\Delta I_{OUT}}{d\Delta V_{IN}^3}\right|_{\Delta V_{IN}=0} \Delta V_{IN}^3 \tag{2.1.17}$$

Since $\Delta I_{OUT} = 0$ for $\Delta V_{IN} = 0$ (balanced distribution of current on the two branches of the circuit in Figure 2.1.1), we can conclude immediately that $\Delta I_{OUT}\,(\Delta V_{IN} = 0) = 0$.
The following subsection address the calculation of the remaining terms.

First derivative $\left.\dfrac{d\Delta I_{OUT}}{d\Delta V_{IN}}\right|_{V_{IN}=0}$

From Eq. (2.1.14), after having defined $u = \frac{\Delta V_{IN} - R\Delta I_{OUT}}{2\eta V_{th}}$ we got:

$$\frac{d\Delta I_{OUT}}{d\Delta V_{IN}} = I_0 \frac{d\tanh(u)}{du}\frac{du}{d\Delta V_{IN}} \tag{2.1.18}$$

From the definition of u we get:

$$\frac{du}{d\Delta V_{IN}} = \frac{d\frac{\Delta V_{IN} - R\Delta I_{OUT}}{2\eta V_{th}}}{d\Delta V_{IN}} = \frac{1}{2\eta V_{th}}\frac{d(\Delta V_{IN} - R\Delta I_{OUT})}{d\Delta V_{IN}} = \frac{1}{2\eta V_{th}}\left(1 - R\frac{d\Delta I_{OUT}}{d\Delta V_{IN}}\right) \tag{2.1.19}$$

Substituting Equation (2.1.19) into Equation (3.3.10) we got:

$$\frac{d\Delta I_{OUT}}{d\Delta V_{IN}} = \frac{I_0}{2\eta V_{th}}\frac{d\tanh(u)}{du}\left(1 - R\frac{\Delta I_{OUT}}{d\Delta V_{IN}}\right) \tag{2.1.20}$$

and by reminding that $\frac{d\tanh(u)}{du} = \operatorname{sech}^2(u)$:

$$\frac{d\Delta I_{OUT}}{d\Delta V_{IN}} = \frac{I_0}{2\eta V_{th}}\operatorname{sech}^2(u)\left(1 - R\frac{d\Delta I_{OUT}}{d\Delta V_{IN}}\right) \tag{2.1.21}$$

which, once solved for $\frac{d\Delta I_{OUT}}{d\Delta V_{IN}}$, provides:

$$\frac{d\Delta I_{OUT}}{d\Delta V_{IN}} = \frac{\frac{I_0}{2\eta V_{th}}\operatorname{sech}^2(u)}{\left(1 + R\frac{I_0}{2\eta V_{th}}\operatorname{sech}^2(u)\right)} \tag{2.1.22}$$

Since $\Delta I_{OUT} = 0$ for $\Delta V_{IN} = 0$, as pointed out above, from the definition of $u = \frac{\Delta V_{IN} - R\Delta I}{2\eta V_{th}}$ leads to $u = 0$. For $\Delta V_{IN} = 0$ we obtain therefore:

$$\left.\frac{d\Delta I_{OUT}}{d\Delta V_{IN}}\right|_{\Delta V_{IN}=0} = \frac{I_0}{2\eta V_{th}} \frac{\operatorname{sech}^2(u)}{\left(1 + R\frac{I_0}{2\eta V_{th}}\operatorname{sech}^2(u)\right)} = \frac{\frac{I_0}{2\eta V_{th}}}{1 + \frac{RI_0}{2\eta V_{th}}} \tag{2.1.23}$$

where it has been reminded that $\operatorname{sech}(0) = 1$

Second derivative $\left.\frac{d^2\Delta I_{OUT}}{d\Delta V_{IN}^2}\right|_{V_{IN}=0}$

The second derivative of Equation (2.1.14) is the first derivative of Equation (2.1.22). So we can derive further Equation (2.1.22). We start by calculating the derivative of $\operatorname{sech}^2(u)$, by reminding that $u = \frac{\Delta V_{IN} - R\Delta I_{OUT}}{2\eta V_{th}}$:

$$\begin{aligned}\frac{d\operatorname{sech}^2\left(\frac{\Delta V_{IN} - R\Delta I_{OUT}}{2\eta V_{th}}\right)}{d\Delta V_{IN}} = & -2\operatorname{sech}^2\left(\frac{\Delta V_{IN} - R\Delta I_{OUT}}{2\eta V_{th}}\right) \\ & \times \tanh\left(\frac{\Delta V_{IN} - R\Delta I_{OUT}}{2\eta V_{th}}\right)\frac{1 - R\frac{d\Delta I_{OUT}}{d\Delta V_{IN}}}{2\eta V_{th}}\end{aligned} \tag{2.1.24}$$

Now rewriting Equation(2.1.22) and substituting $\frac{I_0}{2V_{th}}\operatorname{sech}^2\left(\frac{\Delta V_{IN} - R\Delta I_{OUT}}{2\eta V_{th}}\right)$ with A, where $A^{(1)}$ denotes the first derivative, we obtain the following equation:

$$\frac{d}{d\Delta V_{IN}}\left(\frac{A}{1 + RA}\right) = \frac{A^{(1)}(1 + RA) - RA^{(1)}A}{(1 + RA)^2} = \frac{A^{(1)}}{(1 + RA)^2} \tag{2.1.25}$$

But $A^{(1)}$ is equal to Equation(2.1.24), so you get :

$$\frac{A^{(1)}}{(1 + RA)^2} = \frac{I_0\left(1 - R\frac{d\Delta I_{OUT}}{d\Delta V_{IN}}\right)}{(2\eta V_{th})^2} \frac{-2\operatorname{sech}^2\left(\frac{\Delta V_{IN} - R\Delta I_{OUT}}{2\eta V_{th}}\right)\tanh\left(\frac{\Delta V_{IN} - R\Delta I_{OUT}}{2\eta V_{th}}\right)}{\left[1 + \frac{RI_0}{2\eta V_{th}}\operatorname{sech}^2\left(\frac{\Delta V_{IN} - R\Delta I_{OUT}}{2\eta V_{th}}\right)\right]^2} \tag{2.1.26}$$

In the Equation the term $\frac{d\Delta I_{OUT}}{d\Delta V_{IN}}$ appears, that we can substitute with the Equation (2.1.22) to obtain:

$$\begin{aligned}\frac{d^2\Delta I_{OUT}}{d\Delta V_{IN}^2} &= \left[1 - \frac{RI_0 \operatorname{sech}^2\left(\frac{\Delta V_{IN}-R\Delta I_{OUT}}{2\eta V_{th}}\right)}{2\eta V_{th}\left[1+\frac{RI_0}{2\eta V_{th}}\operatorname{sech}^2\left(\frac{\Delta V_{IN}-R\Delta I_{OUT}}{2\eta V_{th}}\right)\right]}\right] \\ &\quad \times \frac{-2I_0 \operatorname{sech}^2\left(\frac{\Delta V_{IN}-R\Delta I_{OUT}}{2\eta V_{th}}\right)\tanh\left(\frac{\Delta V_{IN}-R\Delta I_{OUT}}{2\eta V_{th}}\right)}{(2\eta V_{th})^2\left[1+\frac{RI_0}{2\eta V_{th}}\operatorname{sech}^2\left(\frac{\Delta V_{IN}-R\Delta I_{OUT}}{2\eta V_{th}}\right)\right]^2} \\ &= -\frac{2I_0}{(2\eta V_{th})^2}\frac{\operatorname{sech}^2\left(\frac{\Delta V_{IN}-R\Delta I_{OUT}}{2\eta V_{th}}\right)\tanh\left(\frac{\Delta V_{IN}-R\Delta I_{OUT}}{2\eta V_{th}}\right)}{\left[1+\frac{RI_0}{2\eta V_{th}}\operatorname{sech}^2\left(\frac{\Delta V_{IN}-R\Delta I_{OUT}}{2\eta V_{th}}\right)\right]^3}\end{aligned} \tag{2.1.27}$$

Calculating this Equation for $\Delta V_{IN} = 0$ into this Equation gives 0, since the presence of the tanh term in the numerator.
This makes sense because, for continuity principle applied to R, the $\Delta I_{OUT} = \Delta I_{OUT}(\Delta V_{IN})$ curve is expected to exhibit an odd simmetry around the origin.

Third derivative $\left.\dfrac{d^3\Delta I_{OUT}}{d\Delta V_{IN}^3}\right|_{V_{IN}=0}$

Starting from the Equation (2.1.27), we can substitute the following parameters:

$$\begin{aligned} u = \frac{\Delta V_{IN} - R\Delta I_{OUT}}{2\eta V_{th}}, \qquad Z = \frac{d^2\Delta I_{OUT}}{d\Delta V_{IN}^2}, \\ \frac{du}{d\Delta V_{IN}} = \frac{d}{d\Delta V_{IN}}\left(\frac{\Delta V_{IN} - R\Delta I_{OUT}}{2\eta V_{th}}\right)\end{aligned} \tag{2.1.28}$$

This allow to rewrite easily the third derivative in function of the second derivative. The third derivative become $\dfrac{d^3\Delta I_{OUT}}{d\Delta V_{IN}^3} = \dfrac{dZ}{du}\dfrac{du}{d\Delta V_{IN}}$. We can also define

$$F_1 = \operatorname{sech}^2(u)\,\tanh(u), \qquad F_2 = \left(1 + \frac{I_0 R}{2\eta V_{th}}\operatorname{sech}^2(u)\right)^{-3} \tag{2.1.29}$$

so that $Z = -\dfrac{I_0}{2\eta V_{th}^2}\,F_1\,F_2$. Applying the product rule, the third derivative takes the following form:

$$\frac{dZ}{du} = -\frac{I_0}{2\eta V_{th}^2}\left(\frac{dF_1}{du}\frac{du}{d\Delta V_{IN}}\,F_2 + F_1\,\frac{dF_2}{du}\frac{du}{d\Delta V_{IN}}\right). \tag{2.1.30}$$

Using the chain rule and recalling from Eq.2.1.24 the derivative of $\text{sech}^2(u)$:

$$\frac{dF_1}{d\Delta V_{IN}} = \frac{d}{d\Delta V_{IN}}\big[\,\text{sech}^2(u)\tanh(u)\big] = \Big[-2\,\text{sech}^2(u)\tanh^2(u) + \text{sech}^4(u)\Big]\frac{du}{d\Delta V_{IN}}. \quad (2.1.31)$$

For F_2, let $G(u) = 1 + \frac{I_0 R}{2\eta V_{th}}\,\text{sech}^2(u)$, so $F_2 = [G(u)]^{-3}$. Then

$$\begin{aligned}\frac{dF_2}{d\Delta V_{IN}} =& -3[G(u)]^{-4}\,\frac{dG}{d\Delta V_{IN}} = \\ =& 3\frac{I_0 R}{V_{th}}\,\text{sech}^2(u)\tanh(u)\,\frac{du}{d\Delta V_{IN}}\,[G(u)]^{-4}.\end{aligned} \quad (2.1.32)$$

From the Eq.2.1.28 and substituting also the Eq. (2.1.22):

$$\begin{aligned}\frac{du}{d\Delta V_{IN}} &= \frac{1}{2\eta V_{th}}\,\frac{1}{1+\dfrac{I_0 R}{2\eta V_{th}}\,\text{sech}^2(u)} = \\ &= \frac{1}{2\eta V_{th}}\,[G(u)]^{-1}\end{aligned} \quad (2.1.33)$$

Substituting into the product rule expression and factoring $\dfrac{du}{d\Delta V_{IN}}$ with the denominator $[G(u)]^{-5}$:

$$\begin{aligned}\frac{dZ}{d\Delta V_{IN}} = -\frac{I_0}{2\eta V_{th}^2}\,\frac{du}{d\Delta V_{IN}}\,[G(u)]^{-4}\Bigg\{&\Big[-2\,\text{sech}^2(u)\tanh^2(u) + \text{sech}^4(u)\Big]G(u) \\ &+ 3\frac{I_0 R}{V_{th}}\,\text{sech}^4(u)\tanh^2(u)\Bigg\}.\end{aligned} \quad (2.1.34)$$

Substituting $\dfrac{du}{d\Delta V_{IN}}$ cancels one factor of $G(u)$ in the denominator, passing from power of -4 to power of -5:

$$\begin{aligned}\frac{dZ}{d\Delta V_{IN}} = -\frac{I_0}{4(\eta V_{th})^3}[G(u)]^{-5}\Bigg\{&\Big[-2\,\text{sech}^2(u)\tanh^2(u) + \text{sech}^4(u)\Big]G(u) \\ &+ 3\frac{I_0 R}{V_{th}}\,\text{sech}^4(u)\tanh^2(u)\Bigg\}\end{aligned} \quad (2.1.35)$$

Expanding the bracket and collecting $\operatorname{sech}^4(u)\tanh^2(u)$ terms:

$$\begin{aligned}\frac{dZ}{d\Delta V_{IN}} = & -\frac{I_0}{4(\eta V_{th})^3}[G(u)]^{-5}\Bigg\{ \quad \Big[-2\operatorname{sech}^2(u)\tanh^2(u)+\operatorname{sech}^4(u)\Big]G(u) \\ & +3\frac{I_0R}{V_{th}}\operatorname{sech}^4(u)\tanh^2(u)\Bigg\}.\end{aligned} \tag{2.1.36}$$

Multiplying through by the minus sign:

$$\frac{d^3(\Delta I_{OUT})}{d\Delta V_{IN}^3} = \frac{I_0}{4(\eta V_{th})^3}\frac{\begin{array}{c}2\operatorname{sech}^2(u)\tanh^2(u)-\operatorname{sech}^4(u) \\ -2\dfrac{I_0R}{V_{th}}\operatorname{sech}^4(u)\tanh^2(u)-\dfrac{I_0R}{2\eta V_{th}}\operatorname{sech}^6(u)\end{array}}{\left(1+\dfrac{I_0R}{2\eta V_{th}}\operatorname{sech}^2(u)\right)^5} \tag{2.1.37}$$

with

$$u = \frac{\Delta V_{IN}-R\Delta I_{OUT}}{2\eta V_{th}}. \tag{2.1.38}$$

Equivalently, in explicit form:

$$\begin{aligned}\frac{d^3(\Delta I_{OUT})}{d\Delta V_{IN}^3} = & -\frac{I_0}{4(\eta V_{th})^3}\frac{2\operatorname{sech}^2\left(\dfrac{\Delta V_{IN}-R\Delta I_{OUT}}{2\eta V_{th}}\right)\tanh^2\left(\dfrac{\Delta V_{IN}-R\Delta I_{OUT}}{2\eta V_{th}}\right)-\operatorname{sech}^4\left(\dfrac{\Delta V_{IN}-R\Delta I_{OUT}}{2\eta V_{th}}\right)}{\left(1+\dfrac{I_0R}{2\eta V_{th}}\operatorname{sech}^2\left(\dfrac{\Delta V_{IN}-R\Delta I_{OUT}}{2\eta V_{th}}\right)\right)^5} \\ & -\frac{I_0}{4(\eta V_{th})^3}\frac{2\frac{I_0R}{V_{th}}\operatorname{sech}^4\left(\dfrac{\Delta V_{IN}-R\Delta I_{OUT}}{2\eta V_{th}}\right)\tanh^2\left(\dfrac{\Delta V_{IN}-R\Delta I_{OUT}}{2\eta V_{th}}\right)+\frac{I_0R}{2\eta V_{th}}\operatorname{sech}^6\left(\dfrac{\Delta V_{IN}-R\Delta I_{OUT}}{2\eta V_{th}}\right)}{\left(1+\dfrac{I_0R}{2\eta V_{th}}\operatorname{sech}^2\left(\dfrac{\Delta V_{IN}-R\Delta I_{OUT}}{2\eta V_{th}}\right)\right)^5}\end{aligned} \tag{2.1.39}$$

Then we can calculate the coefficient of the third term that is :

$$\begin{aligned}\left.\frac{d^3\Delta I_{OUT}}{dV_{IN}^3}\right|_{\Delta V_{IN}=0} &= -\frac{I_0}{4(\eta V_{th})^3}\frac{1+\frac{I_0R}{2\eta V_{th}}}{\left(1+\dfrac{I_0R}{2\eta V_{th}}\right)^5} \\ &= -\frac{I_0}{4(\eta V_{th})^3}\frac{1}{\left(1+\dfrac{I_0R}{2\eta V_{th}}\right)^4}\end{aligned} \tag{2.1.40}$$

2.1.1 Harmonic Analysis

Substituting Equations (2.1.23) and (2.1.40) into Equation (2.1.17), we obtain the approximated closed form of Equation (2.1.14):

$$\Delta I_1 = \frac{\frac{I_0}{2\eta V_{th}}}{1+\frac{RI_0}{2\eta V_{th}}}\Delta V_{IN}(t) - \frac{I_0}{24(\eta V_{th})^3}\frac{1}{\left(1+\frac{I_0 R}{2\eta V_{th}}\right)^4}\left[\Delta V_{IN}(t)\right]^3 \tag{2.1.41}$$

To analyze the behaviour of the circuit a single tone excitation is considered. It is assumed $\Delta V_{IN}(t) = \Delta V_{IN}\cos(\omega t)$ where ΔV_{IN} is the amplitude of the differential signal and ω its angular frequency.
From Equation (2.1.41) we got:

$$\Delta I_1 = \frac{\frac{I_0}{2\eta V_{th}}}{1+\frac{RI_0}{2\eta V_{th}}}\Delta V_{IN}\cos(\omega t) - \frac{I_0}{24(\eta V_{th})^3}\frac{1}{\left(1+\frac{I_0 R}{2\eta V_{th}}\right)^4}\left[\Delta V_{IN}\cos(\omega t)\right]^3 \tag{2.1.42}$$

By applying the trigonometric identity $\cos^3(x) = \frac{\cos(3x)+3\cos(x)}{4}$ we obtain:

$$\begin{aligned}\Delta I_{OUT} &= \frac{\frac{I_0}{2\eta V_{th}}}{1+\frac{RI_0}{2\eta V_{th}}}\Delta V_{IN}\cos(\omega t) - \frac{I_0}{24(\eta V_{th})^3}\frac{1}{\left(1+\frac{I_0 R}{2\eta V_{th}}\right)^4}\Delta V_{IN}^3\frac{\cos(3\omega t)+3\cos(\omega t)}{4} \\ &= \frac{\frac{I_0}{2\eta V_{th}}}{1+\frac{RI_0}{2\eta V_{th}}}\Delta V_{IN}\cos(\omega t) - 3\frac{I_0}{24(\eta V_{th})^3}\frac{1}{\left(1+\frac{I_0 R}{2\eta V_{th}}\right)^4}\Delta V_{IN}^3\frac{\cos(\omega t)}{4} \\ &\quad - \frac{I_0}{24(\eta V_{th})^3}\frac{1}{\left(1+\frac{I_0 R}{2\eta V_{th}}\right)^4}\Delta V_{IN}^3\frac{\cos(3\omega t)}{4}\end{aligned} \tag{2.1.43}$$

By gathering the contributions according to the harmonics the ampitude a_1 of the fundamental harmonic and the amplitude a_3 of the third harmonic are, respectively:

$$a_1 = \frac{\frac{I_0}{2\eta V_{th}}}{1+\frac{RI_0}{2V_{th}}}\Delta V_{IN} - 3\frac{I_0}{96(\eta V_{th})^3}\frac{1}{\left(1+\frac{I_0 R}{2\eta V_{th}}\right)^4}\Delta V_{IN}^3 \tag{2.1.44}$$

$$a_3 = -\frac{I_0}{96(\eta V_{th})^3}\frac{1}{\left(1+\frac{I_0 R}{2\eta V_{th}}\right)^4}\Delta V_{IN}^3 \tag{2.1.45}$$

As expected the third order non-linear coefficent a_3 is negative. It result in a reduction of the first order coefficient $a1$. Substituting the Equations 2.1.44 and 2.1.45 in the expression of ΔI_{OUT} you get:

$$\Delta I_{OUT} = a_1 \cos(\omega t) + a_3 \cos(3\omega t) \tag{2.1.46}$$

Now, defining the Spurious Free Dynamic Range (SFDR) as the ratio between the power of the output desires tone and the power highest harmonic distortion in the output spectrum, reported in dBc (dB respect to the carrier). In that case become:

$$SFDR = 20\log_{10}\left[\left|\frac{a_1}{a_3}\right|\right] \tag{2.1.47}$$

where a_1 refer to the equation 2.1.44 and a_3 refer to 2.1.45, the equation lead to the following mathematical equation:

$$SFDR = 20\log_{10}\left|\frac{a_1}{a_3}\right| = 20\log_{10}\left|-6\frac{(2\eta V_{th}+RI_0)^3}{\eta V_{th}\Delta V_{IN}^2}+3\right| \tag{2.1.48}$$

The SFDR is a positive number if $-6\frac{(2\eta V_{th}+RI_0)^3}{\eta V_{th}\Delta V_{IN}^2} > -4$ or $-6\frac{(2\eta V_{th}+RI_0)^3}{\eta V_{th}\Delta V_{IN}^2} > -2$. Soving the expression for ΔV_{IN}, the result is:

$$\Delta V_{IN} > \sqrt{\frac{3(2\eta V_{th}+RI_0)^3}{\eta V_{th}}} \tag{2.1.49}$$

$$0 < \Delta V_{IN} < \sqrt{\frac{3(2\eta V_{th}+RI_0)^3}{2\eta V_{th}}} \tag{2.1.50}$$

Outside these two interval the SFDR is negative, so the a_1 term is lower than a_3.

2.1.2 Application

The amplitudes of fundamental and third harmonics provided by Equations (2.1.44) and (2.1.45) have been computed for the value of I_0, R, ΔV_{IN} and η reported in Table 2.1:

Temperature [K]	I_0 [A]	R [Ω]	ΔV_{IN} [mV]	η	V_{th} [mV]
300	117×10^{-6}	800	100	1.08	26
4	243×10^{-6}	800	100	26.37	0.347

Table 2.1: Circuit parameters at different temperature.

where the I_0 value chosen is the sum of the collector current for each transitor in which the $\beta >> 1$, the value of R is chosen to have the low votage drop to keep the transistor polarized in the correct region and ΔV_{IN} is chosen to be large enough to completely steer the tail current. The η value were calculated from simulation results. Table 2.2 reports the obtained values:

Temperature	**300 K**		**4 K**	
Harmonics	1^{st} tone (a_1) [A]	3^{rd} tone (a_3)[A]	1^{st} tone (a_1)[A]	3^{rd} tone (a_3) [A]
Results	7.490 10^{-5}	1.090 10^{-6}	1.137 10^{-4}	1.811 10^{-7}

Table 2.2: Harmonic amplitudes — Analytical (Taylor) model

2.2 Validation of the Analytical Model

For sake of validation of the obtained analytical model the numerical values of a_1 and a_3 have been obtained also by a recursive numerical approach, by circuit simulation and analytical evaluation of the taylor series using Equation (2.1.41).

2.2.1 DC behaviour

For the parameters in Table 2.1, and for ΔV_{IN} spanning from $-0.6V$ to $0.6V$, Equation (2.1.14) has been solved numerically by an iteration algorithm implemented in Matlab.

Figure (2.2.1)shown the obtained $\Delta I_{OUT} = \Delta I_{OUT}(\Delta V_{IN})$:

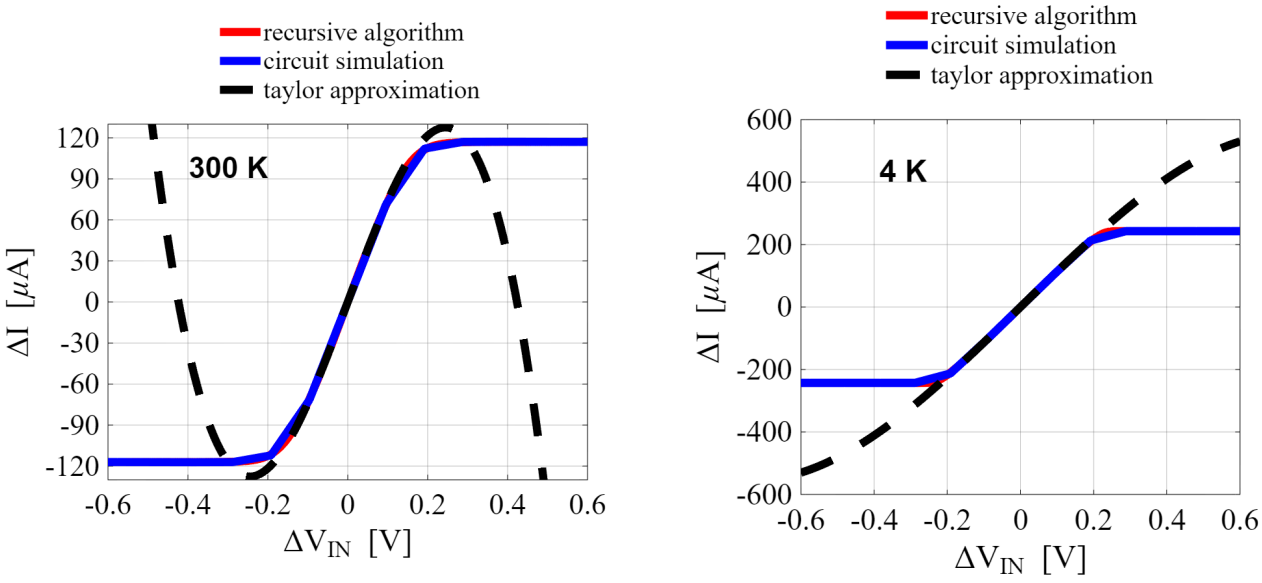


Figure 2.2.1: Linear Sweep of V_{IN} for 300K and 4K

The resulting curve exhibits an odd simmetry around the origin as expected. The circuit simulation and the recursive algorithm exhibits also an excellent agreement at both the temperature. The Taylor series, however, provides a very accurate approximation only in the vicinity of the origin; as one moves away from this point, the approximation becomes progressively less valid.
Defined the differential input knee voltage $\Delta V_{IN_{\text{knee}}}$ as the input differential voltage ΔV_{IN} corresponding to the saturation currents $\Delta I_{OUT} = \pm I_0$.

To derive this value, Equation (2.1.23) can be used, as it represents the slope of the tangent at the origin. The tangent Equation is given by:

$$\Delta I_{OUT} = \frac{\frac{I_0}{2\eta V_{th}}}{1 + \frac{RI_0}{2\eta V_{th}}} \Delta V_{IN} \tag{2.2.1}$$

The maximum value of ΔI_{OUT} is obtained when $\Delta I_{OUT} = I_0$.

By substituting this condition into the previous Equation and solving for ΔV_{IN}, the following result is obtained:

$$I_0 = \frac{\frac{I_0}{2\eta V_{th}}}{1+\frac{RI_0}{2\eta V_{th}}}\Delta V_{IN_{\text{knee}}}, \quad 1 = \frac{\frac{1}{2\eta V_{th}}}{1+\frac{RI_0}{2\eta V_{th}}}\Delta V_{IN_{\text{knee}}}$$

$$\Delta V_{IN_{\text{knee}}} = \frac{1+\frac{RI_0}{2\eta V_{th}}}{\frac{1}{2\eta V_{th}}} = 2\eta V_{th} + RI_0 \tag{2.2.2}$$

therefore corresponds to the input differential voltage for which ΔI_{OUT} reaches its maximum value, according to the first-order Taylor approximation of the curve.

The values for the 300 K and 4 K circuit models are evaluated using the parameter set reported in Table 2.1. The contributions of each term and the resulting knee voltage are reported in Table 2.3.

Temperature [K]	RI_0 [mV]	ηV_{th} [mV]	$\Delta V_{IN_{\text{knee}}}$ [mV]
300	93.6	27.9	149.4
4	194.4	9.1	212.6

Table 2.3: Knee voltage estimated by the analytical Taylor-based model.

These results show that the input voltage at which the output current saturates is mainly determined by the degeneration resistance and the tail current. In particular, lowering the temperature reduces the thermal voltage and increases the relative weight of the resistive contribution. Now, a sinusoidal input voltage $\Delta V_{IN}(t) = \Delta V_{IN}\cos(\omega t)$, with amplitude $\Delta V_{IN} = 100\,\text{mV}$, as in Table 2.1 is applied to the transfer characteristic derived in the previous section. Even in the present case both Matlab and circuit simulation has been carried out. For the Matlab smulation, each instantaneous value of ΔV_{IN} corresponds to a point on the characteristic shown in Figure 2.2.1, and the resulting output waveform $\Delta I_1(t)$ is subsequently processed via Fast Fourier Transform (FFT) to extract the individual spectral components, which are then compared against the predictions of the analytical model. For the numerical evaluation, the input signal is sampled at n discrete time instants, producing a sequence of samples ΔV_{IN_k}, with $k = 0, 1, \ldots, n-1$. For each sample, the corresponding output current ΔI_{1_k} is determined by solving the following equation:

$$\Delta I_{1_k} - I_0 \tanh\left(\frac{\Delta V_{IN_k} - R\,\Delta I_{1_k}}{2\,\eta\,V_{th}}\right) = 0 \tag{2.2.3}$$

This Equation is implicit. The solution is obtained iteratively. For each sampled input ΔV_{IN_k}, an initial guess $\Delta I_{1_{in,0}}$ is assumed, and the following update rule is applied:

$$\Delta I_{1_{out,j+1}} = I_0 \tanh\left(\frac{\Delta V_{IN_k} - R\,\Delta I_{1_{in,j}}}{2\,\eta\,V_{th}}\right) \tag{2.2.4}$$

where the output of each iteration is used to re-compute the value of $\Delta I_{1_{out,j+1}}$, keeping ΔV_{IN_k} fixed. The iteration is considered converged when:

$$\left|\Delta I_{1_{out,j+1}} - \Delta I_{1_{in,j}}\right| < \varepsilon \tag{2.2.5}$$

In the Matlab implementation, this procedure is computed numerically using a nonlinear solver, with the same tolerance criterion applied.
Once the full output sequence $\{\Delta I_{1_k}\}_{k=0}^{n-1}$ is obtained, the output spectrum is computed via the Matlab FFT function. Considering $\varepsilon = 10^{-14}$, the output spectrum of the FFT process at different temperature yields:

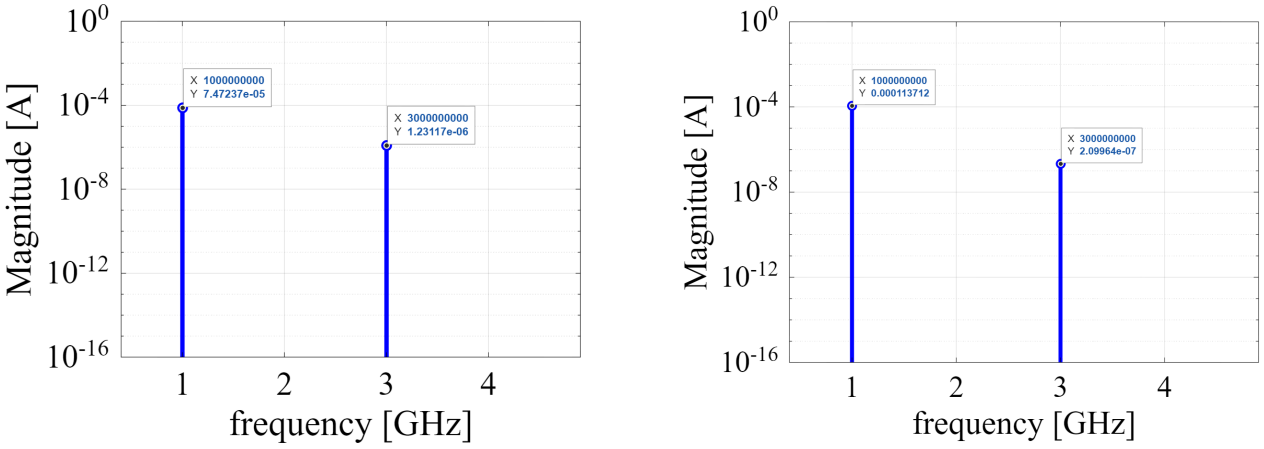


Figure 2.2.2: Matlab spectrum obtained for 300K (on the left) and 4K (on the right) calculated from Equation 2.1.13

Table 2.4 shows the resulting amplitudes:

Temperature	**300 K**		**4 K**	
Harmonics	1^{st} Harmonics [A]	3^{rd} Harmonics [A]	1^{st} Harmonics [A]	3^{rd} Harmonics [A]
Results	7.472410^{-5}	1.231210^{-6}	1.135110^{-4}	2.124110^{-7}

Table 2.4: Tones of the FFT Matlab spectrum

As far as the circuit simulation, were carried out in the time domain (transient simulation). Plotting the output differential signal current and using the Spectrum tools in cadence we plot the spectrum of the differential current. Figure 2.2.3 shows the obtained spectrum.

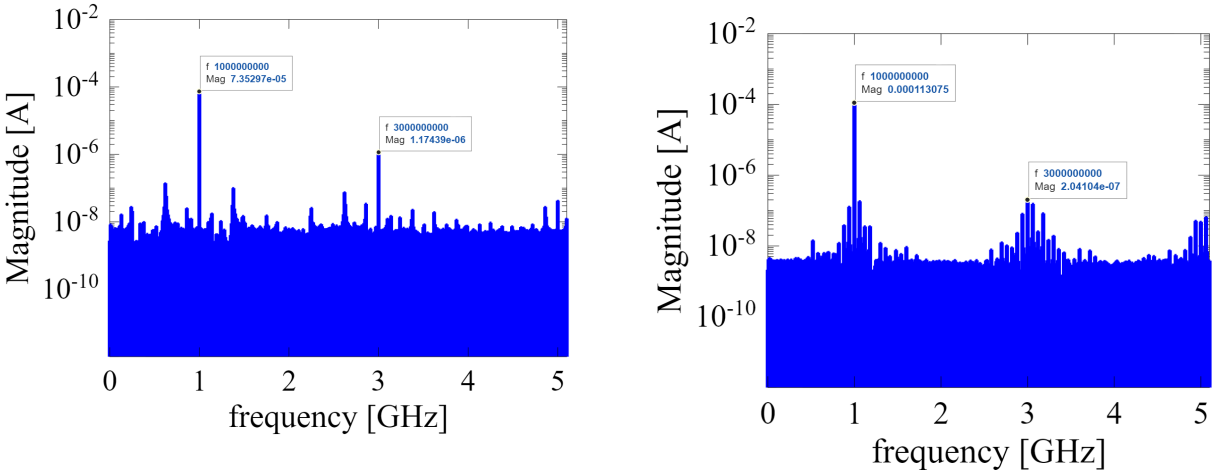


Figure 2.2.3: FFT spectrum for 300K (on the left) and 4K (on the right) from circuit simulation

Temperature	**300 K**		**4 K**	
Harmonics	1^{st} Harmonics [A]	3^{rd} Harmonics [A]	1^{st} Harmonics [A]	3^{rd} Harmonics [A]
Results	7.35310^{-5}	1.174410^{-6}	1.130710^{-4}	2.041110^{-7}

Table 2.5: Harmonic amplitudes — Circuit Model

2.3 Overall Comparison

The following Table 2.6 provides as overall comparisons of the fundamental and third order harmonic obtained from the analytical model, from Matlab simualtion and from circuit simulation.

Parameters		**Circuit Simulation**	**Matlab Simulation**		**Analitical Model**	
T[K]	**Tone**	**Value[A]**	**Value[A]**	**Error[%]**	**Value[A]**	**Error [%]**
300	1^{st}	7.353×10^{-5}	7.4724×10^{-5}	-1.6	7.5003×10^{-5}	-2
	3^{rd}	1.1744×10^{-6}	1.2312×10^{-6}	-4.8	1.0914×10^{-6}	7
4	1^{st}	1.1307×10^{-4}	1.1351×10^{-4}	-0.39	1.1334×10^{-4}	-0.24
	3^{rd}	2.0411×10^{-7}	2.1241×10^{-7}	-4.1	2.0171×10^{-7}	1.2

Table 2.6: Overall comparison with relative error for the tones evaluated at 300 K and 4 K

In the overall comparison the result is very satisfying. The relative error:

$$Error[\%] \triangleq 100\frac{A_{circuit} - A_{simulation}}{A_{circuit}} \tag{2.3.1}$$

where $A_{circuit}$ is the amplitude from the circuit simulation and A_{model} the amplitude from the analytical or Matlab simulation.

2.4 Comparing the two configuration for same transconductance value

Assume to change the value of the I_0 value at 300k, to have the same transconductance value as in the 4k. To equate the transconductances values at both the temperature we must realize that the current at 300K must be $\frac{300\eta_{300K}}{4\eta_{4K}} I_{0_{4k}}$. The resulting value is $I_0 = 735uA$. Simulating for that current value the resulting spectrum is:

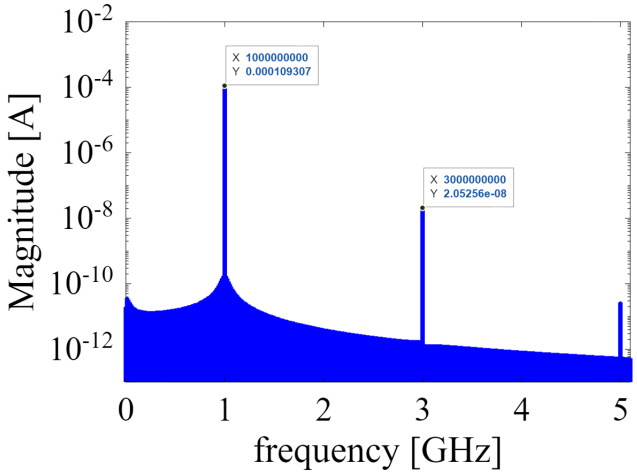


Figure 2.4.1: Spectrum evaluation for current value of $735uA$

If we compare the result with the one calculate using the Taylor series, after recover the value of η, that for this current value is equal to $\eta = 1.38$ we obtain the following table:

Parameters		**Circuit Model**	**Matlab Model**		**Analitical Model**	
T[K]	**Tone**	**Value[A]**	**Value[A]**	**Error[%]**	**Value[A]**	**Error [%]**
300	1^{st}	1.0937×10^{-4}	1.1409×10^{-04}	-4.316	1.1147×10^{-4}	-4.873
	3^{rd}	2.0525×10^{-8}	2.3141×10^{-8}	13	2.3129×10^{-8}	12.9

Table 2.7: Harmonic amplitudes - 300k values with transconductance value equal to the one at 4K

Comparing the 4K circuit (see table 2.7) with the 300K one, the value of the fundamental component are very close each other. The third Harmonic, instead is much lower than the 4K ones probably due to the fact that the factor deacreases with $\frac{1}{V_{th}^2}$

2.5 Conclusions

Figure 2.2.1, Tables 2.5 and 2.6 give evidence of the correctness of the analytical model developed in the present chapter by Taylor approximation. This model will be thus applied in the next chapter to address more involved circuits, that can be used for frequency conversion purposes.

3 Gilbert multiplier vs Jones demodulator

3.1 Introduction

This section proposes an analytical modelization of the Gilbert multiplier and the Jones demodulator, aimed to comparing them in terms of harmonic and intermodulation products generation. Before addressing the analysis of these circuits, it is binding pointing out that practically all textbooks and papers refer to the Jones demodulator as the Gilbert cell. Despite current practice, this is an erroneous designation, because even if both the two circuits perform frequency translation, that is they operate as a mixer, nevertheless they leverage on different principles. The Jones demodulator leverages on the time variance using some transistors as switches [50], that is in a digital way, while the Gilbert cell on a very smart and strictly analog use of transistor non-linearities, in order to implement a product of signals; under an algebraic point of view, multiplication is indeed a non-linear operation [51] [52].

3.2 Gilbert multiplier

Figure 3.2.1 shows that the circuit is composed by two subcircuits: an input differential amplifier and a Gilbert cell. The figure shows also that four differential pairs, as that investigated in Section 2.3, are present in the circuit. In particular the differential pair formed by the transistor Q3 and Q4 (Q5 and Q6) is a differential pair without resistive degeneration and it exploits the collector current I_{C1} (I_{C2}) of Q1 (Q2) as tail current.

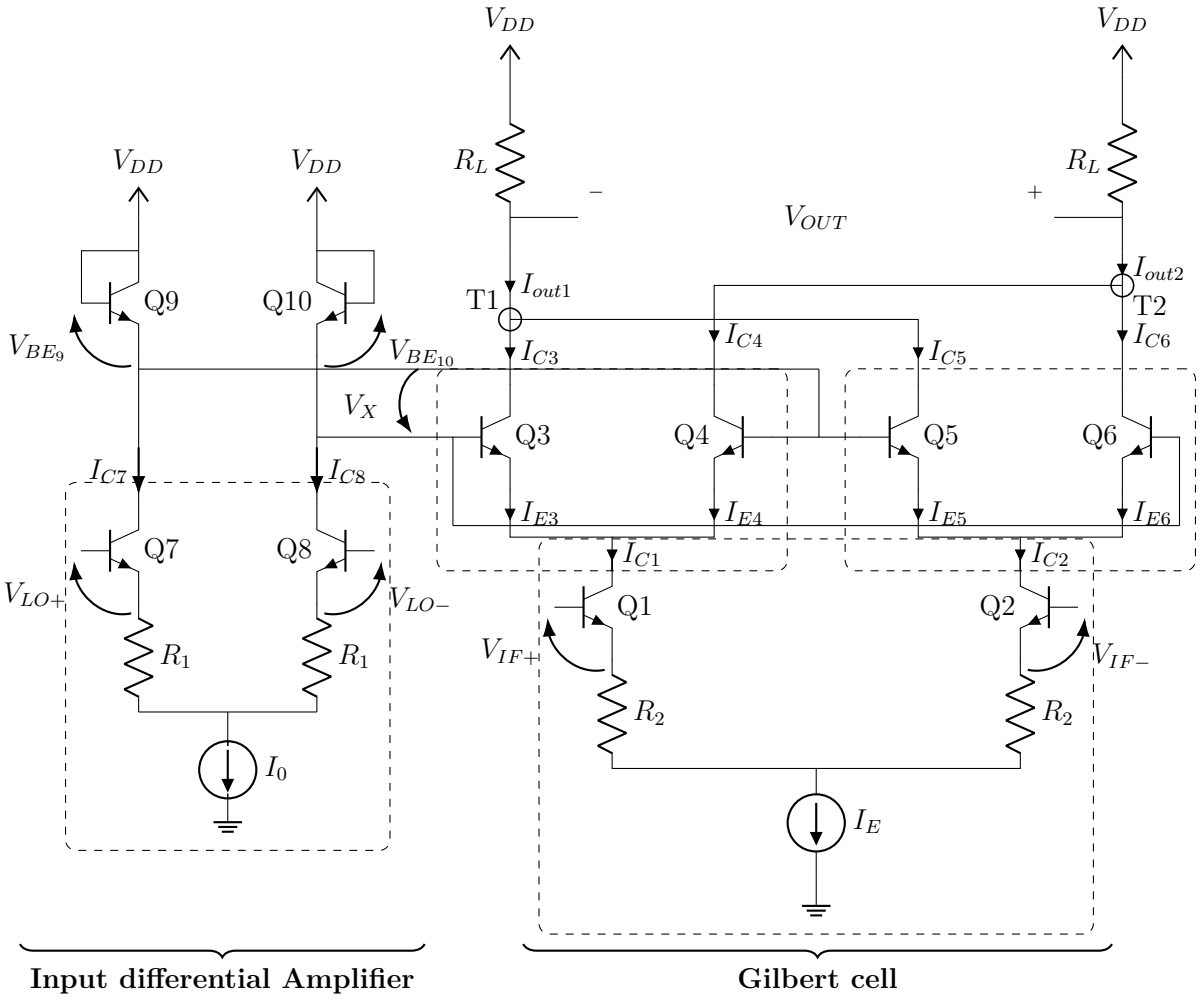


Figure 3.2.1: Schematic of the Gilbert multiplier

3.3 Circuit Analysis

According to Section 2.1, collector and emitter currents can be assumed identical ($I_{C_i} = I_{E_i},\ i = 1, ...10$) and the following equation are written down:

$$\Delta I_{78} = I_0 \tanh\left(\frac{\Delta V_{LO} - R_1 \Delta I_{78}}{2\eta V_{th}}\right) \tag{3.3.1}$$

$$\Delta I_{12} = I_E \tanh\left(\frac{\Delta V_{IF} - R_2 \Delta I_{12}}{2\eta V_{th}}\right) \tag{3.3.2}$$

with $\Delta I_{78} \triangleq I_{C7} - I_{C8}$, $\Delta I_{12} \triangleq I_{C1} - I_{C2}$, $\Delta V_{LO} \triangleq V_{LO+} - V_{LO-}$ and $\Delta V_{IF} \triangleq V_{IF+} - V_{IF-}$. The differential pair Q7-Q8 is loaded by the transistors Q9-Q10 in diode configuration. The output voltage V_X is thus:

$$\begin{aligned} V_X &= (V_{DD} - V_{BE_{10}}) - (V_{DD} - V_{BE_9}) = V_{BE_9} - V_{BE_{10}} \\ &= \eta V_{th} \ln\left(\frac{I_{C7}}{I_{sc}}\right) - V_{th} \ln\left(\frac{I_{C8}}{I_{sc}}\right) = \eta V_{th} \ln\left(\frac{I_{C7}}{I_{C8}}\right) \end{aligned} \tag{3.3.3}$$

From the definition of the differential current ΔI_{78} and the relation $I_0 = I_{C7} + I_{C8}$ we can rewrite both I_{C7} and I_{C8} as:

$$I_{C7} = \frac{I_0 + \Delta I_{78}}{2} \tag{3.3.4}$$

$$I_{C8} = \frac{I_0 - \Delta I_{78}}{2} \tag{3.3.5}$$

By substituting Equations (3.3.4) and (3.3.5) into Equation (3.3.3) we can write:

$$V_X = \eta V_{th} \ln\left(\frac{\frac{I_0 + \Delta I_{78}}{2}}{\frac{I_0 - \Delta I_{78}}{2}}\right) = \eta V_{th} \ln\left(\frac{1 + \frac{\Delta I_{78}}{I_0}}{1 - \frac{\Delta I_{78}}{I_0}}\right) \tag{3.3.6}$$

By reminding that atanh(x) $= \frac{1}{2}\ln\left(\frac{1+x}{1-x}\right)$, the previous equation can be reformulated as follows:

$$V_X = 2\eta V_{th} \frac{1}{2} \ln\left(\frac{1 + \frac{\Delta I_{78}}{I_0}}{1 - \frac{\Delta I_{78}}{I_0}}\right) = 2\eta V_{th} \operatorname{atanh}\left(\frac{\Delta I_{78}}{I_0}\right) \tag{3.3.7}$$

The differential output voltage V_{OUT} can be calculated as:

$$V_{OUT} = V_{CC} - I_{out2} R_L - (V_{CC} - I_{out1} R_L) = R_L (I_{out1} - I_{out2}) \tag{3.3.8}$$

Current balance at node $T1$ and $T2$ yields $I_{out1} = I_{C3} + I_{C5}$ and $I_{out2} = I_{C4} + I_{C6}$, respectively, so that you can write:

$$V_{OUT} = R_L[I_{C3} + I_{C5} - (I_{C4} + I_{C6})] = R_L[(I_{C3} - I_{C4}) + (I_{C5} - I_{C6})] \tag{3.3.9}$$

The results in Section 2.3 can be applied also to the Q3-Q4 and Q5-Q6 transistor pair but with $R = 0$:

$$I_{C3} - I_{C4} = I_{C1} \tanh\left(\frac{V_X}{2\eta V_{th}}\right) \tag{3.3.10}$$

$$I_{C5} - I_{C6} = I_{C2} \tanh\left(-\frac{V_X}{2\eta V_{th}}\right) = -I_{C2} \tanh\left(\frac{V_X}{2\eta V_{th}}\right) \tag{3.3.11}$$

By substituting Equations (3.3.10) and (3.3.11) into Equation (3.3.9) the output voltage results to be:

$$\begin{aligned} V_{OUT} &= R_L \left[I_{C1} \tanh\left(\frac{V_X}{2\eta V_{th}}\right) - I_{C2} \tanh\left(\frac{V_X}{2\eta V_{th}}\right)\right] = \\ &= R_L \tanh\left(\frac{V_X}{2\eta V_{th}}\right)(I_{C1} - I_{C2}) = R_L \tanh\left(\frac{V_X}{2\eta V_{th}}\right)\Delta I_{12} \end{aligned} \tag{3.3.12}$$

By reminding Equations (3.3.2) and (3.3.7) the Equation (3.3.12) yields:

$$\begin{aligned} V_{OUT} &= R_L \Delta I_{12} \tanh\left[\frac{2\eta V_{th}\, \mathrm{atanh}\left(\frac{\Delta I_{78}}{I_0}\right)}{2\eta V_{th}}\right] \\ &= R_L \Delta I_{12} \frac{\Delta I_{78}}{I_0} \end{aligned} \tag{3.3.13}$$

It is worth reminding that, according to the results obtained in Chapter 2, ΔI_{12} and ΔI_{78} are recursively defined functions in the two variables ΔV_{LO} and ΔV_{RF}, respectively. Because of Equation (3.3.13) V_{OUT} results thus recursevely defined in ΔV_{LO} and ΔV_{RF}, as well. With $x \triangleq V_{RF}$ and $y \triangleq V_{LO}$ from Chapter 2 you get:

$$g(x) = I_E \tanh\left[\frac{x - R_2 g(x)}{2\eta V_{th}}\right] \tag{3.3.14}$$

and

$$h(y) = I_0 \tanh\left[\frac{x - R_1 h(y)}{2\eta V_{th}}\right] \tag{3.3.15}$$

and thus Equation (3.3.13) becomes:

$$V_{OUT} = \frac{R_L}{I_0} g(x)h(y) = \frac{R_L}{I_0} f(x,y) \tag{3.3.16}$$

with $f(x,y) \triangleq g(x)h(y)$.
By extension of the approach used in Chapter 2, in the present case we provide an approximated closed form of $f(x,y)$ by means of a bidimensional Taylor series:

$$f(x,y) = f(x_0,y_0) + \sum_{n=1}^{\infty} \left\{ \sum_{k=0}^{n} \frac{1}{k!(n-k)!} \frac{\delta^n f}{\delta^{n-k} x \delta^k y}\bigg|_{x_0,y_0} (x-x_0)^{n-k}(y-y_0)^k \right\} \tag{3.3.17}$$

Since we are interested in approximating V_{OUT} around $\Delta V_{IF} = 0$ and $\Delta V_{LO} = 0$, for which $\Delta I_{12} = 0$ and $\Delta I_{78} = 0$, you have $x_0 = 0$, $y_0 = 0$, and $f(x_0,y_0) = 0$.
Thus you can write:

$$f(x,y) = \sum_{n=1}^{\infty} \left\{ \sum_{k=0}^{n} \frac{1}{k!(n-k)!} \frac{\delta^n f}{\delta^{n-k} x \delta^k y}\bigg|_{0,0} (x)^{n-k}(y)^k \right\} \tag{3.3.18}$$

By defining $Q_n = \frac{R_L}{I_0} \sum_{k=0}^{n} \frac{1}{k!(n-k)!} \frac{\delta^n f}{\delta^{n-k} x \delta^k y}\Big|_{0,0} x^{n-k} y^k$ from Equation (3.3.16) we get $V_{OUT} = \sum_{i=1}^{4} Q_i$ with:

$$Q_1 = \frac{R_L}{I_0} \left[\frac{\delta f}{\delta x}\bigg|_{(0,0)} x + \frac{\delta f}{\delta y}\bigg|_{(0,0)} y \right] \tag{3.3.19}$$

$$Q_2 = \frac{R_L}{I_0} \left[\frac{1}{2}\frac{\delta^2 f}{\delta^2 x}\bigg|_{(0,0)} x^2 + \frac{\delta^2 f}{\delta x \delta y}\bigg|_{(0,0)} xy + \frac{1}{2}\frac{\delta^2 f}{\delta^2 y}\bigg|_{(0,0)} y^2 \right] \tag{3.3.20}$$

$$Q_3 = \frac{R_L}{I_0} \left[\frac{1}{6}\frac{\delta^3 f}{\delta x^3}\bigg|_{(0,0)} x^3 + \frac{1}{2}\frac{\delta^3 f}{\delta x^2 \delta y}\bigg|_{(0,0)} x^2 y + \frac{1}{2}\frac{\delta^3 f}{\delta x \delta y^2}\bigg|_{(0,0)} xy^2 + \frac{1}{6}\frac{\delta^3 f}{\delta y^3}\bigg|_{(0,0)} y^3 \right] \tag{3.3.21}$$

$$\begin{aligned} Q_4 = \frac{R_L}{I_0} \Big[& \frac{1}{24}\frac{\delta^4 f}{\delta x^4}\bigg|_{(0,0)} x^4 + \frac{1}{6}\frac{\delta^4 f}{\delta x^3 \delta y}\bigg|_{(0,0)} x^3 y + \frac{1}{4}\frac{\delta^4 f}{\delta x^2 \delta y^2}\bigg|_{(0,0)} x^2 y^2 + \frac{1}{6}\frac{\delta^4 f}{\delta x \delta y^3}\bigg|_{(0,0)} xy^3 \\ & + \frac{1}{24}\frac{\delta^4 f}{\delta y^4}\bigg|_{(0,0)} y^4 \Big] \end{aligned} \tag{3.3.22}$$

Because of Equation (3.3.16) the mathematical expression above can be further calculated as follows:

$$Q_1 = \frac{R_L}{I_0}\left[\frac{\delta g(x)}{\delta x}\bigg|_{x=0} h(0)x + g(0)\frac{\delta h(y)}{\delta y}\bigg|_{y=0} y\right] \tag{3.3.23}$$

$$Q_2 = \frac{R_L}{I_0}\left[\frac{1}{2}\frac{\delta^2 g(x)}{\delta x^2}\bigg|_{x=0} h(0)x^2 + \frac{\delta g(x)}{\delta x}\bigg|_{x=0}\frac{\delta h(y)}{\delta y}\bigg|_{y=0} xy + \frac{1}{2}\frac{\delta^2 h(y)}{\delta y^2}\bigg|_{y=0} g(0)y^2\right] \tag{3.3.24}$$

$$\begin{aligned} Q_3 = \frac{R_L}{I_0}\Bigg[&\frac{1}{6}\frac{\delta^3 g(x)}{\delta x^3}\bigg|_{x=0} h(0)x^3 + \frac{1}{2}\frac{\delta^2 g(x)}{\delta x^2}\bigg|_{x=0}\frac{\delta h(y)}{\delta y}\bigg|_{y=0} x^2 y \\ &+\frac{1}{2}\frac{\delta g(x)}{\delta x}\bigg|_{x=0}\frac{\delta^2 h(y)}{\delta y^2}\bigg|_{y=0} xy^2 + \frac{1}{6}\frac{\delta^3 h(y)}{\delta y^3}\bigg|_{y=0} g(0)y^3\Bigg] \end{aligned} \tag{3.3.25}$$

$$\begin{aligned} Q_4 = \frac{R_L}{I_0}\Bigg[&\frac{1}{24}\frac{\delta^4 g(x)}{\delta x^4}\bigg|_{x=0} h(0)x^4 + \frac{1}{6}\frac{\delta^3 g(x)}{\delta x^3}\bigg|_{x=0}\frac{\delta h(y)}{\delta y}\bigg|_{y=0} x^3 y + \frac{1}{4}\frac{\delta^2 g(x)}{\delta x^2}\bigg|_{x=0}\frac{\delta^2 h(y)}{\delta y^2}\bigg|_{y=0} x^2 y^2 \\ &+\frac{1}{6}\frac{\delta g(x)}{\delta x}\bigg|_{x=0}\frac{\delta^3 h(y)}{\delta y^3}\bigg|_{y=0} xy^3 + \frac{1}{24}\frac{\delta^4 h(y)}{\delta y^4}\bigg|_{y=0} g(0)y^4\Bigg] \end{aligned} \tag{3.3.26}$$

Now, the derivative of the Equations $g(x)$ and $h(y)$ correspond to the derivatives obtained in Section 2.1. So, taking each derivative and evaluating it in the origin, we can observe that $g(0) = h(0) = 0$.
We can notice that also the second derivative of both functions, $\frac{\delta^2 g(x)}{\delta x^2}$ and $\frac{\delta^2 h(y)}{\delta y^2}$ are equal to zero, because the functions are symmetric the origin point.
In this way, we get:

$$Q_1 = 0 \tag{3.3.27}$$

$$Q_2 = \frac{R_L}{I_0}\frac{\delta g(x)}{\delta x}\bigg|_{x=0}\frac{\delta h(y)}{\delta y}\bigg|_{y=0} xy \tag{3.3.28}$$

$$Q_3 = 0 \tag{3.3.29}$$

$$Q_4 = \frac{R_L}{I_0}\left[\frac{1}{6}\frac{\delta^3 g(x)}{\delta x^3}\bigg|_{x=0}\frac{\delta h(y)}{\delta y}\bigg|_{y=0} x^3 y + \frac{1}{6}\frac{\delta g(x)}{\delta x}\bigg|_{x=0}\frac{\delta^3 h(y)}{\delta y^3}\bigg|_{y=0} xy^3\right] \tag{3.3.30}$$

Eventually, substituting Equation (2.1.23) and (2.1.40) into Equations (3.3.28) and (3.3.30) yields:

$$Q_2 = \frac{R_L}{I_0} \frac{\frac{I_0}{2\eta V_{th}}}{1+\frac{R_1 I_0}{2\eta V_{th}}} \frac{\frac{I_E}{2\eta V_{th}}}{1+\frac{R_2 I_E}{2\eta V_{th}}} xy \tag{3.3.31}$$

$$Q_4 = -\frac{R_L}{I_0}\left[\frac{1}{6}\frac{\frac{I_0}{4(\eta V_{th})^3}}{(1+\frac{R_1 I_0}{2\eta V_{th}})^4}\frac{\frac{I_E}{2\eta V_{th}}}{1+\frac{R_2 I_E}{2\eta V_{th}}} xy^3 + \frac{1}{6}\frac{\frac{I_E}{4(\eta V_{th})^3}}{(1+\frac{R_2 I_E}{2\eta V_{th}})^4}\frac{\frac{I_0}{2\eta V_{th}}}{1+\frac{R_1 I_0}{2\eta V_{th}}} x^3 y\right] \tag{3.3.32}$$

Bringing terms to common denominator and applying algebraic simplifications yields the final mathematical expressions:

$$Q_2 = \frac{R_L}{I_0}\frac{I_0}{2\eta V_{th}+R_1 I_0}\frac{I_E}{2\eta V_{th}+R_2 I_E} xy \tag{3.3.33}$$

$$\begin{aligned} Q_4 = -\frac{R_L}{I_0}\Big[&\frac{1}{6}\frac{4\eta V_{th} I_0}{(2\eta V_{th}+R_1 I_0)^4}\frac{I_E}{2\eta V_{th}+R_2 I_E} xy^3 \\ &+ \frac{1}{6}\frac{4\eta V_{th} I_E}{(2\eta V_{th}+R_2 I_E)^4}\frac{I_0}{2\eta V_{th}+R_1 I_0} x^3 y\Big] \end{aligned} \tag{3.3.34}$$

Assuming x and y sinusoidal voltages:

$$x = V_{IF}\cos(\omega_{IF} t) \tag{3.3.35}$$

$$y = V_{LO}\cos(\omega_{LO} t) \tag{3.3.36}$$

the term Q_2 becomes:

$$Q_2 = \frac{R_L}{I_0}\frac{I_0}{2\eta V_{th}+R_1 I_0}\frac{I_E}{2\eta V_{th}+R_2 I_E} V_{IF} V_{LO}\cos(\omega_{IF} t)\cos(\omega_{LO} t) \tag{3.3.37}$$

Since we can rewrite the product of two sinusoidal signal by using the trigonometric identity:

$$\cos(\alpha)\cos(\beta) = \frac{\cos(\alpha-\beta)+\cos(\alpha+\beta)}{2} \tag{3.3.38}$$

Equation (3.3.37) takes the following form:

$$Q_2 = \frac{R_L}{I_0}\frac{I_0}{2\eta V_{th}+R_1 I_0}\frac{I_E}{2\eta V_{th}+R_2 I_E} V_{IF} V_{LO}\frac{\cos[(\omega_{IF}+\omega_{LO})t]+\cos[(\omega_{IF}-\omega_{LO})t]}{2} \tag{3.3.39}$$

This results in second-order intermodulation products. The term $Q4$ generates second and fourth order intermodulation products.

By substituting Equations (3.3.35) and (3.3.36) into Equation (3.3.34), we get indeed:

$$\begin{aligned} Q_4 = &- \frac{R_L}{6I_0} \frac{4\eta V_{th} I_0}{(2\eta V_{th} + R_1 I_0)^4} \frac{I_E}{2\eta V_{th} + R_2 I_E} V_{IF} \cos(\omega_{IF} t) \left[V_{LO} \cos(\omega_{LO} t)\right]^3 + \\ &- \frac{R_L}{6I_0} \frac{4\eta V_{th} I_E}{(2\eta V_{th} + R_2 I_E)^4} \frac{I_0}{2\eta V_{th} + R_1 I_0} \left[V_{IF} \cos(\omega_{IF} t)\right]^3 V_{LO} \cos(\omega_{LO} t) \end{aligned} \tag{3.3.40}$$

Now, by reminding the trigonometric identity:

$$\cos^3(\alpha) = \frac{\cos(3\alpha) + 3\cos(\alpha)}{4} \tag{3.3.41}$$

Equation (3.3.40) results in:

$$\begin{aligned} Q_4 = &- \frac{R_L}{6I_0} \frac{4\eta V_{th} I_0}{(2\eta V_{th} + R_1 I_0)^4} \frac{I_E}{2\eta V_{th} + R_2 I_E} V_{IF} V_{LO}^3 \cos(\omega_{IF} t) \frac{\cos(3\omega_{LO} t) + 3\cos(\omega_{LO} t)}{4} + \\ &- \frac{R_L}{6I_0} \frac{4\eta V_{th} I_E}{(2\eta V_{th} + R_2 I_E)^4} \frac{I_0}{2\eta V_{th} + R_1 I_0} V_{IF}^3 V_{LO} \cos(\omega_{LO} t) \frac{\cos(3\omega_{IF} t) + 3\cos(\omega_{IF} t)}{4} \end{aligned} \tag{3.3.42}$$

Applying Equation (3.3.38) to Equation (3.3.42) leads to eight distinct tones:

$$\begin{aligned} Q_4 = &- \frac{R_L}{6I_0} \frac{4\eta V_{th} I_0}{(2\eta V_{th} + R_1 I_0)^4} \frac{I_E}{2\eta V_{th} + R_2 I_E} V_{IF} V_{LO}^3 \frac{\cos[(3\omega_{LO} + \omega_{IF})t] + \cos[(3\omega_{LO} - \omega_{IF})]}{8} + \\ &- \frac{R_L}{6I_0} \frac{4\eta V_{th} I_0}{(2\eta V_{th} + R_1 I_0)^4} \frac{I_E}{2\eta V_{th} + R_2 I_E} V_{IF} V_{LO}^3 \frac{3\cos[(\omega_{LO} + \omega_{IF})t] + 3\cos[(\omega_{LO} - \omega_{IF})]}{8} + \\ &- \frac{R_L}{6I_0} \frac{4\eta V_{th} I_E}{(2\eta V_{th} + R_2 I_E)^4} \frac{I_0}{2\eta V_{th} + R_1 I_0} V_{IF}^3 V_{LO} \frac{\cos[(3\omega_{IF} + \omega_{LO})t] + \cos[(3\omega_{IF} - \omega_{LO})t]}{8} + \\ &\frac{R_L}{6I_0} \frac{4\eta V_{th} I_E}{(2\eta V_{th} + R_2 I_E)^4} \frac{I_0}{2\eta V_{th} + R_1 I_0} V_{IF}^3 V_{LO} \frac{3\cos[(\omega_{IF} + \omega_{LO})t] + 3\cos[(\omega_{IF} - \omega_{LO})t]}{8} \end{aligned} \tag{3.3.43}$$

Denoting the amplitude of the second-order intermodulation products as $V_{OUT}(\omega_{LO} \pm \omega_{IF})$, as $V_{OUT}(3\omega_{IF} \pm \omega_{LO})$ the amplitudes for the tones at frequency $3\omega_{IF} \pm \omega_{LO}$, and as $V_{OUT}(\omega_{IF} \pm 3\omega_{LO})$ the amplitudes for the tones at the frequency $\omega_{IF} \pm 3\omega_{LO}$, we can write:

$$
\begin{aligned}
V_{OUT}(\omega_{LO} \pm \omega_{IF}) =& \frac{R_L}{2} \frac{1}{2\eta V_{th} + R_1 I_0} \frac{I_E}{2\eta V_{th} + R_2 I_E} V_{IF} V_{LO} \\
&- \frac{R_L}{4} \frac{\eta V_{th}}{(2\eta V_{th} + R_1 I_0)^4} \frac{I_E}{2\eta V_{th} + R_2 I_E} V_{IF} V_{LO}^3 \\
&- \frac{R_L}{4} \frac{I_E \eta V_{th}}{(2\eta V_{th} + R_2 I_E)^4} \frac{1}{2\eta V_{th} + R_1 I_0} V_{IF}^3 V_{LO} \qquad (3.3.44) \\
V_{OUT}(3\omega_{LO} \pm \omega_{IF}) =& - \frac{R_L}{12} \frac{\eta V_{th}}{(2\eta V_{th} + R_1 I_0)^4} \frac{I_E}{2\eta V_{th} + R_2 I_E} V_{IF} V_{LO}^3 \qquad (3.3.45) \\
V_{OUT}(\omega_{LO} \pm 3\omega_{IF}) =& - \frac{R_L}{12} \frac{I_E \eta V_{th}}{(2\eta V_{th} + R_2 I_E)^4} \frac{1}{2\eta V_{th} + R_1 I_0} V_{IF}^3 V_{LO} \qquad (3.3.46)
\end{aligned}
$$

3.3.1 Circuit simulation and comparison

For sake of validation of Equations (3.3.44)-(3.3.46), the circuit in Fig. 3.2.1 has been implemented in the SG13G2 130nm SiGe BiCMOS technology by IHP (Innovation for High-Performance Microelectronics) in Frankfurt am Oder (Germany). The Design Kit (DK) offers Room Temperature (RT) and Cryogenic Temperature models (CT). Figure 3.3.1 shows the resulting schematic. The circuit has been therefore simulated both at RT (300K) and at CT (4K). Since in Equations (3.3.44)-(3.3.46) amplitude exhibits specific dependence on V_{RF} and V_{LO}, we performed transient simulations by sweeping V_{RF} (V_{LO}) while keeping V_{LO} (V_{RF}) constant. Then, by performing an FFT on the output signal, we obtained the amplitude of each tone, and plotted it against the sweeping voltage.

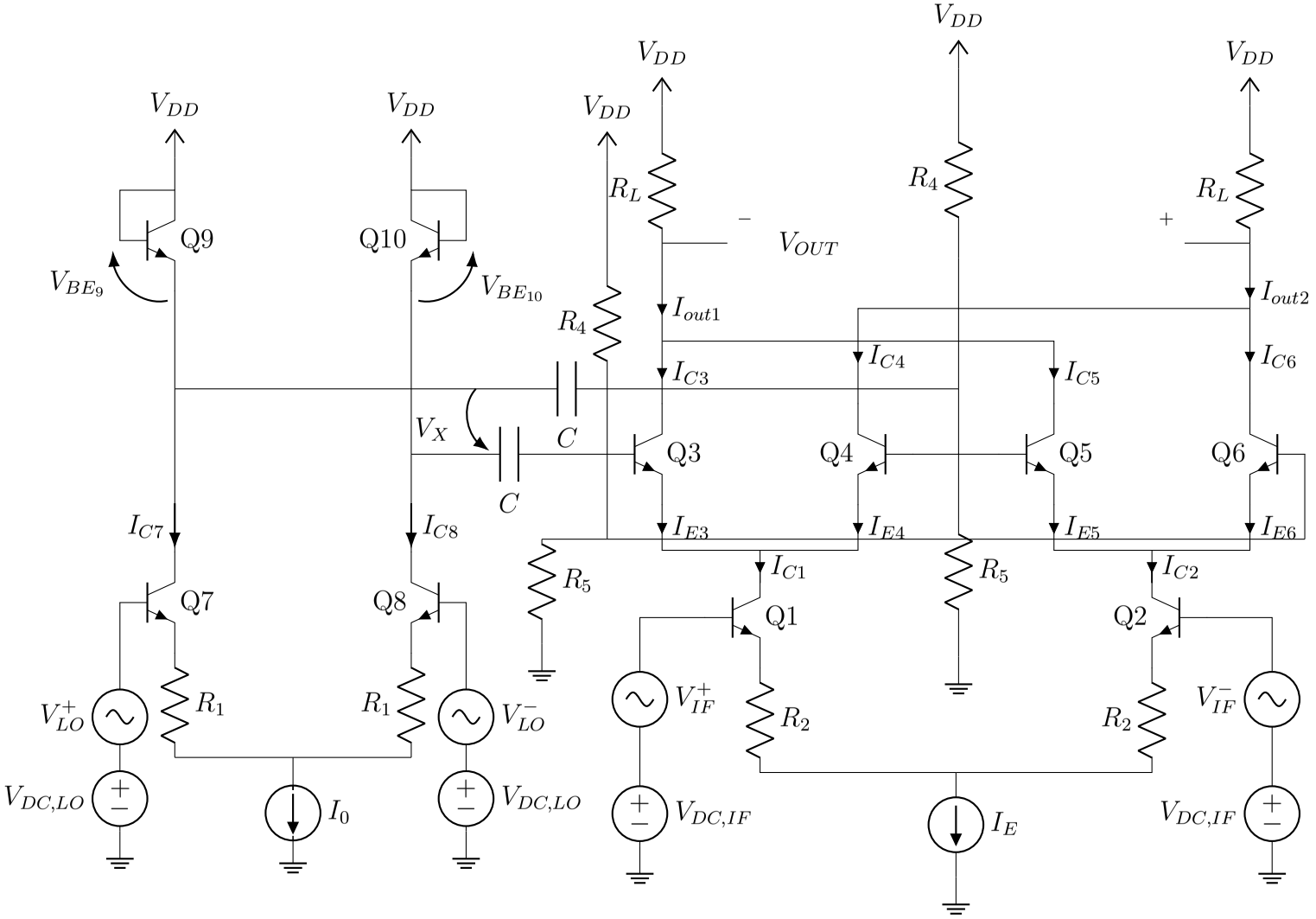


Figure 3.3.1: Schematic of Gilbert multiplier implemented in the IHP technology

Tables 3.1 and 3.2 report the adopted values for resistors, capacitors and bias, respectively.

Temp [K]	$R_L\,[\Omega]$	$R_1\ [\Omega]$	$R_2\ [\Omega]$	$R_4\,[k\Omega]$	$R_5\,[k\Omega]$	$C\,[pF]$
300	2000	800	800	15	150	100
4	2000	800	800	20	160	100

Table 3.1: Resistors and capacitors at RT and CT

Temp [K]	$I_0\,[\mu A]$	$I_E\,[\mu A]$	$V_{DD}\,[V]$	$V_{DC,IF}\,[V]$	$V_{DC,LO}\,[V]$
300	117	117	2.5	1.2	1.2
4	243	243	2.5	1.2	1.2

Table 3.2: Bias voltages at RT and CT and tail currents

Table 3.3 reports the sizes adopted for the bipolar transistors. The values of η were obtained in Chapter 1.

Temp [K]	W [nm]	L [nm]	m1	η
300	70	900	1	1.08
4	70	900	1	26.37

Table 3.3: Transistor sizes. m1 refer to the number of emitter, the effectively area emitter is defined as m1$\times W \times L$

Transient simulations were carried out by sweeping V_{LO} (V_{IF}) from 1μV to 100mV with V_{IF} (V_{LO}) kept constant at 100mV. In particular, the local oscillator frequency ω_{LO} was kept equal to $1GHz$ and the intermediate frequency ω_{IF} equal to $140MHz$. The amplitudes of the output tones calculated from Equations (3.3.44)-(3.3.46) and reported in Tables 3.4-3.7, have been compared with the amplitudes from the spectra obtained from the transient simulations, reported in Tables 3.8-3.11. Moreover, for sake of readability, Figures 3.3.2-3.3.7 depict calculated and simulated amplitudes.

V_{LO} [mV]	$V_{OUT}(\omega_{LO} \pm \omega_{IF})$ [V]	$V_{OUT}(\omega_{LO} \pm 3\omega_{IF})$ [V]	$V_{OUT}(3\omega_{LO} \pm \omega_{IF})$ [V]
0.001	$5.0180\,10^{-07}$	$7.3017\,10^{-09}$	$7.3017\,10^{-19}$
0.01	$5.0180\,10^{-06}$	$7.3017\,10^{-08}$	$7.3017\,10^{-16}$
0.1	$5.0180\,10^{-05}$	$7.3017\,10^{-07}$	$7.3017\,10^{-13}$
1	$5.0180\,10^{-04}$	$7.3017\,10^{-06}$	$7.3017\,10^{-10}$
10	$5.0158\,10^{-03}$	$7.3017\,10^{-05}$	$7.3017\,10^{-07}$
100	$4.7990\,10^{-02}$	$7.3017\,10^{-04}$	$7.3017\,10^{-04}$
Reference	Fig. 3.3.2a	Fig. 3.3.3a	Fig. 3.3.4a

Table 3.4: Calculated tone amplitudes at 300 K for sweeping V_{LO} and $V_{IF} = 100mV$

V_{IF} [mV]	$V_{OUT}(\omega_{LO} \pm \omega_{IF})$ [V]	$V_{OUT}(\omega_{LO} \pm 3\omega_{IF})$ [V]	$V_{OUT}(3\omega_{LO} \pm \omega_{IF})$ [V]
0.001	$5.0180\,10^{-07}$	$7.3017\,10^{-19}$	$7.3017\,10^{-09}$
0.01	$5.0180\,10^{-06}$	$7.3017\,10^{-16}$	$7.3017\,10^{-08}$
0.1	$5.0180\,10^{-05}$	$7.3017\,10^{-13}$	$7.3017\,10^{-07}$
1	$5.0180\,10^{-04}$	$7.3017\,10^{-10}$	$7.3017\,10^{-06}$
10	$5.0158\,10^{-03}$	$7.3017\,10^{-07}$	$7.3017\,10^{-05}$
100	$4.7990\,10^{-02}$	$7.3017\,10^{-04}$	$7.3017\,10^{-04}$
Reference	Fig. 3.3.2b	Fig. 3.3.3b	Fig. 3.3.4b

Table 3.5: Calculated tone amplitudes at 300 K for sweeping V_{IF} and $V_{LO} = 100mV$

V_{LO} [mV]	$V_{OUT}(\omega_{LO} \pm \omega_{IF})$ [V]	$V_{OUT}(\omega_{LO} \pm 3\omega_{IF})$ [V]	$V_{OUT}(3\omega_{LO} \pm \omega_{IF})$ [V]
0.001	$5.3519\,10^{-07}$	$8.4800\,10^{-10}$	$8.4800\,10^{-20}$
0.01	$5.3519\,10^{-06}$	$8.4800\,10^{-09}$	$8.4800\,10^{-17}$
0.1	$5.3519\,10^{-05}$	$8.4800\,10^{-08}$	$8.4800\,10^{-14}$
1	$5.3519\,10^{-04}$	$8.4800\,10^{-07}$	$8.4800\,10^{-11}$
10	$5.3516\,10^{-03}$	$8.4800\,10^{-06}$	$8.4800\,10^{-08}$
100	$5.3264\,10^{-02}$	$8.4800\,10^{-05}$	$8.4800\,10^{-05}$
Reference	Fig. 3.3.5a	Fig. 3.3.6a	Fig. 3.3.7a

Table 3.6: Calculated tone amplitudes at 4 K for sweeping V_{LO} and $V_{IF} = 100mV$

V_{IF} [mV]	$V_{OUT}(\omega_{LO} \pm \omega_{IF})$ [V]	$V_{OUT}(\omega_{LO} \pm 3\omega_{IF})$ [V]	$V_{OUT}(3\omega_{LO} \pm \omega_{IF})$ [V]
0.001	$5.3519\,10^{-07}$	$8.4800\,10^{-20}$	$8.4800\,10^{-10}$
0.01	$5.3519\,10^{-06}$	$8.4800\,10^{-17}$	$8.4800\,10^{-09}$
0.1	$5.3519\,10^{-05}$	$8.4800\,10^{-14}$	$8.4800\,10^{-08}$
1	$5.3519\,10^{-04}$	$8.4800\,10^{-11}$	$8.4800\,10^{-07}$
10	$5.3516\,10^{-03}$	$8.4800\,10^{-08}$	$8.4800\,10^{-06}$
100	$5.3264\,10^{-02}$	$8.4800\,10^{-05}$	$8.4800\,10^{-05}$
Reference	Fig. 3.3.5b	Fig. 3.3.6b	Fig. 3.3.7b

Table 3.7: Calculated tone amplitudes at 4 K for sweeping V_{IF} and $V_{LO} = 100mV$

V_{LO} [mV]	$V_{OUT}(\omega_{LO} \pm \omega_{IF})$ [V]	$V_{OUT}(\omega_{LO} \pm 3\omega_{IF})$ [V]	$V_{OUT}(3\omega_{LO} \pm \omega_{IF})$ [V]
0.001	$4.6330\,10^{-07}$	$6.9274\,10^{-09}$	$1.2925\,10^{-14}$
0.01	$4.6330\,10^{-06}$	$6.9274\,10^{-08}$	$1.1127\,10^{-13}$
0.1	$4.6330\,10^{-05}$	$6.9274\,10^{-07}$	$1.6486\,10^{-12}$
1	$4.6330\,10^{-04}$	$6.9274\,10^{-06}$	$7.2195\,10^{-10}$
10	$4.6310\,10^{-03}$	$6.9252\,10^{-05}$	$7.1587\,10^{-07}$
100	$4.4132\,10^{-02}$	$6.6560\,10^{-04}$	$8.1567\,10^{-04}$
Reference	Fig. 3.3.2a	Fig. 3.3.3a	Fig. 3.3.4a

Table 3.8: Simulated tone amplitudes at 300 K for sweeping V_{IF} and $V_{LO} = 100\,\mathrm{mV}$

V_{IF} [mV]	$V_{OUT}(\omega_{LO} \pm \omega_{IF})$ [V]	$V_{OUT}(\omega_{LO} \pm 3\omega_{IF})$ [V]	$V_{OUT}(3\omega_{LO} \pm \omega_{IF})$ [V]
0.001	$4.6060\,10^{-07}$	$1.2783\,10^{-13}$	$8.4457\,10^{-09}$
0.01	$4.6060\,10^{-06}$	$1.2785\,10^{-12}$	$8.4457\,10^{-08}$
0.1	$4.6060\,10^{-05}$	$1.3022\,10^{-11}$	$8.4457\,10^{-07}$
1	$4.6060\,10^{-04}$	$6.4265\,10^{-10}$	$8.4456\,10^{-06}$
10	$4.6042\,10^{-03}$	$5.8303\,10^{-07}$	$8.4431\,10^{-05}$
100	$4.4132\,10^{-02}$	$6.6560\,10^{-04}$	$8.1567\,10^{-04}$
Reference	Fig. 3.3.2b	Fig. 3.3.3b	Fig. 3.3.4b

Table 3.9: Simulated Tone amplitudes a 300 K for sweeping V_{IF} and $V_{LO} = 100\,\mathrm{mV}$

V_{LO} [mV]	$V_{OUT}(\omega_{LO} \pm \omega_{IF})$ [V]	$V_{OUT}(\omega_{LO} \pm 3\omega_{IF})$ [V]	$V_{OUT}(3\omega_{LO} \pm \omega_{IF})$ [V]
0.001	$5.2134\,10^{-07}$	$6.9732\,10^{-10}$	$2.1976\,10^{-16}$
0.01	$5.2134\,10^{-06}$	$6.9732\,10^{-09}$	$2.7170\,10^{-15}$
0.1	$5.2134\,10^{-05}$	$6.9731\,10^{-08}$	$6.2791\,10^{-13}$
1	$5.2134\,10^{-04}$	$6.9657\,10^{-07}$	$6.0625\,10^{-10}$
10	$5.2155\,10^{-03}$	$6.2385\,10^{-06}$	$5.9957\,10^{-07}$
100	$5.3140\,10^{-02}$	$9.3929\,10^{-05}$	$1.6049\,10^{-04}$
Reference	Fig. 3.3.5a	Fig. 3.3.6a	Fig. 3.3.7a

Table 3.10: Simulated tone amplitudes at 4 K for sweeping V_{LO} and $V_{IF} = 100\,\text{mV}$

V_{IF} [mV]	$V_{OUT}(\omega_{LO} \pm \omega_{IF})$ [V]	$V_{OUT}(\omega_{LO} \pm 3\omega_{IF})$ [V]	$V_{OUT}(3\omega_{LO} \pm \omega_{IF})$ [V]
0.001	$5.3366\,10^{-07}$	$2.9581\,10^{-15}$	$2.0341\,10^{-09}$
0.01	$5.3366\,10^{-06}$	$1.0588\,10^{-13}$	$2.0341\,10^{-08}$
0.1	$5.3366\,10^{-05}$	$3.2405\,10^{-12}$	$2.0341\,10^{-07}$
1	$5.3365\,10^{-04}$	$2.3202\,10^{-10}$	$2.0339\,10^{-06}$
10	$5.3367\,10^{-03}$	$7.1311\,10^{-07}$	$1.9477\,10^{-05}$
100	$5.3140\,10^{-02}$	$9.3929\,10^{-05}$	$1.6049\,10^{-04}$
Reference	Fig. 3.3.5b	Fig. 3.3.6b	Fig. 3.3.7b

Table 3.11: Simulated tone amplitudes at 4 K for sweeping V_{IF} and $V_{LO} = 100\,\text{mV}$

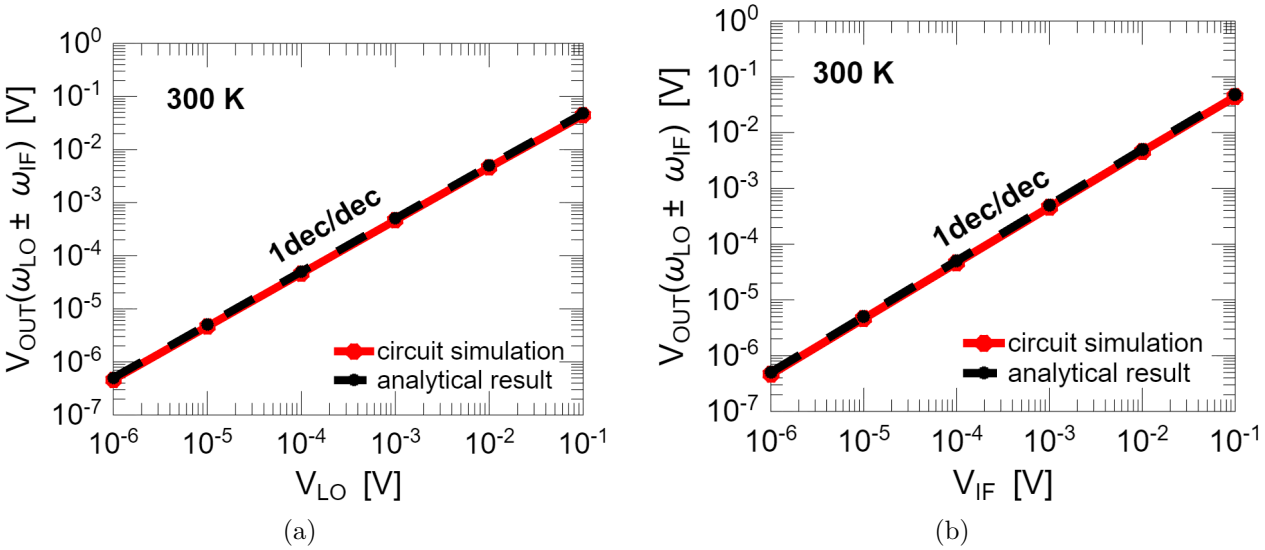
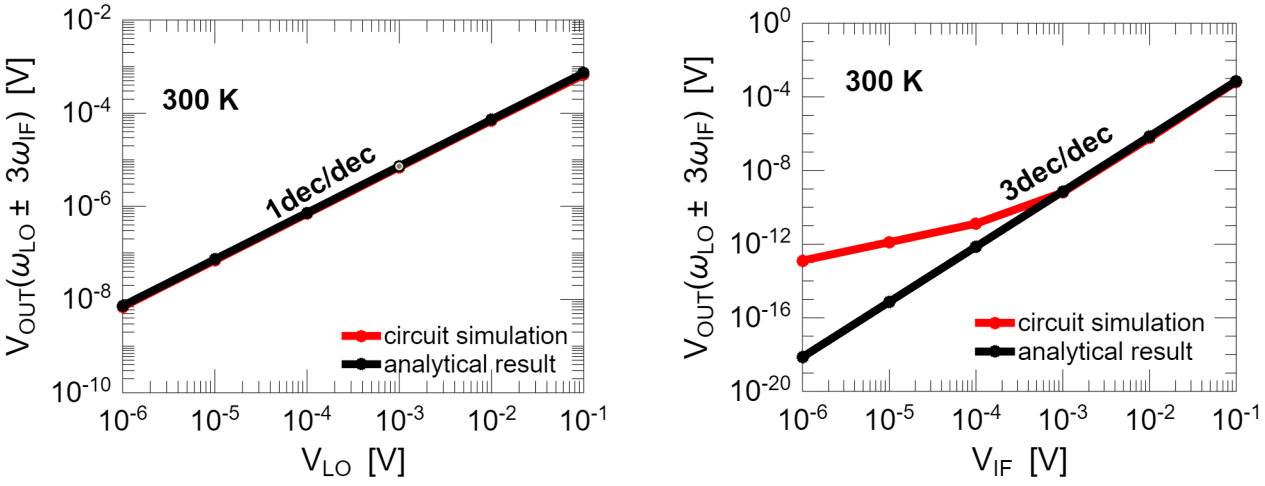
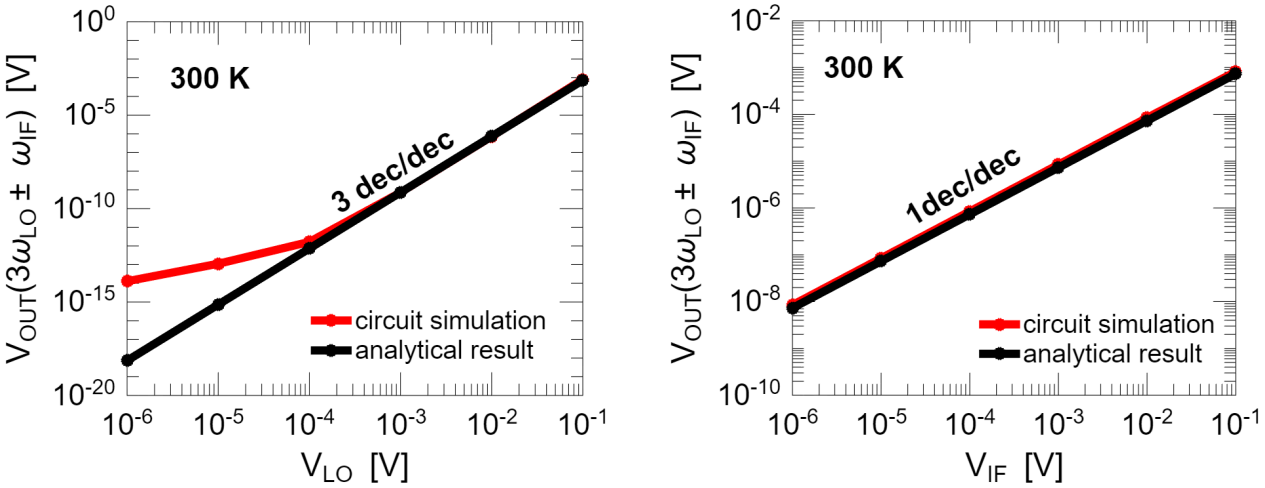


Figure 3.3.2: Amplitude of second-order intermodulation product versus V_{LO} (**a**) and V_{IF} (**b**) for $V_{IF} = 100\,\text{mV}$ and $V_{LO} = 100\,\text{mV}$, respectively, at 300 K.



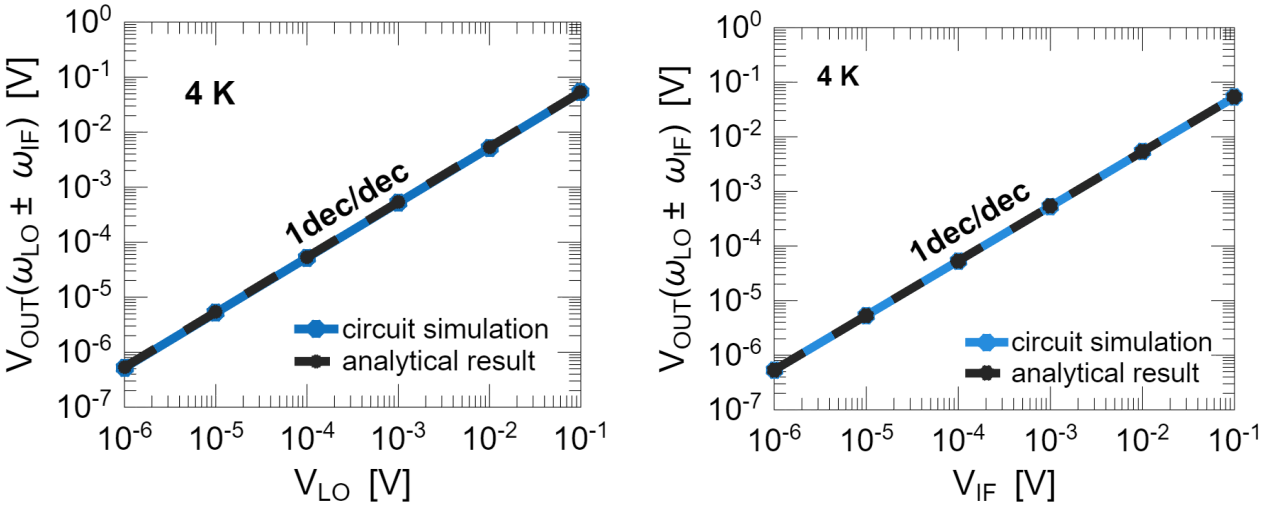
(a) (b)

Figure 3.3.3: Amplitude of third-order intermodulation product at $\omega_{LO} \pm 3\omega_{IF}$ versus V_{LO} (**a**) and V_{IF} (**b**) for $V_{IF} = 100\,\text{mV}$ and $V_{LO} = 100\,\text{mV}$, respectively, at 300 K.



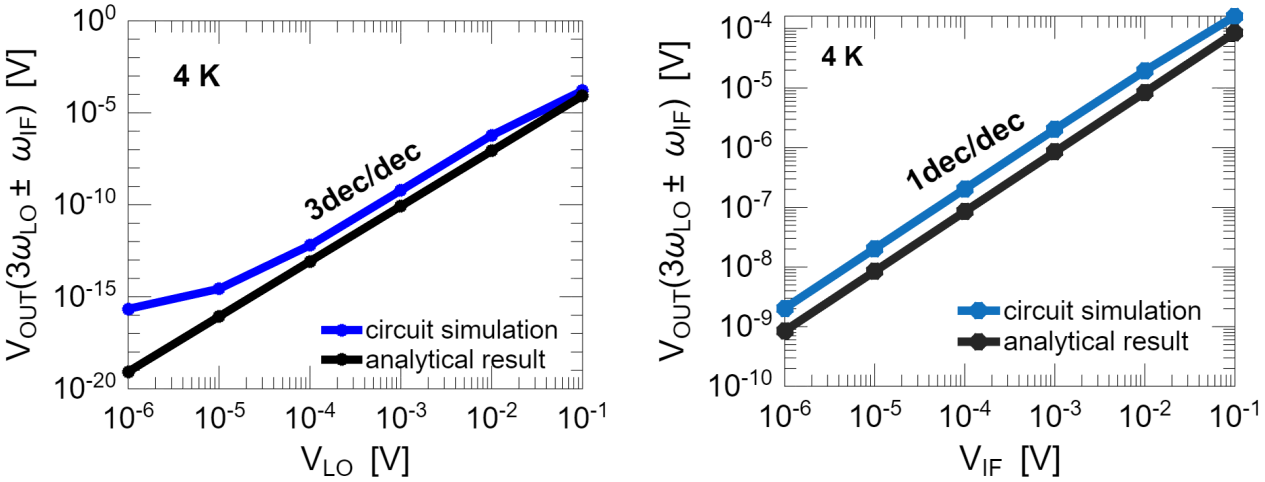
(a) (b)

Figure 3.3.4: Amplitude of third-order intermodulation product at $3\omega_{LO} \pm \omega_{IF}$ versus V_{LO} (**a**) and V_{IF} (**b**) for $V_{IF} = 100\,\text{mV}$ and $V_{LO} = 100\,\text{mV}$, respectively, at 300 K.



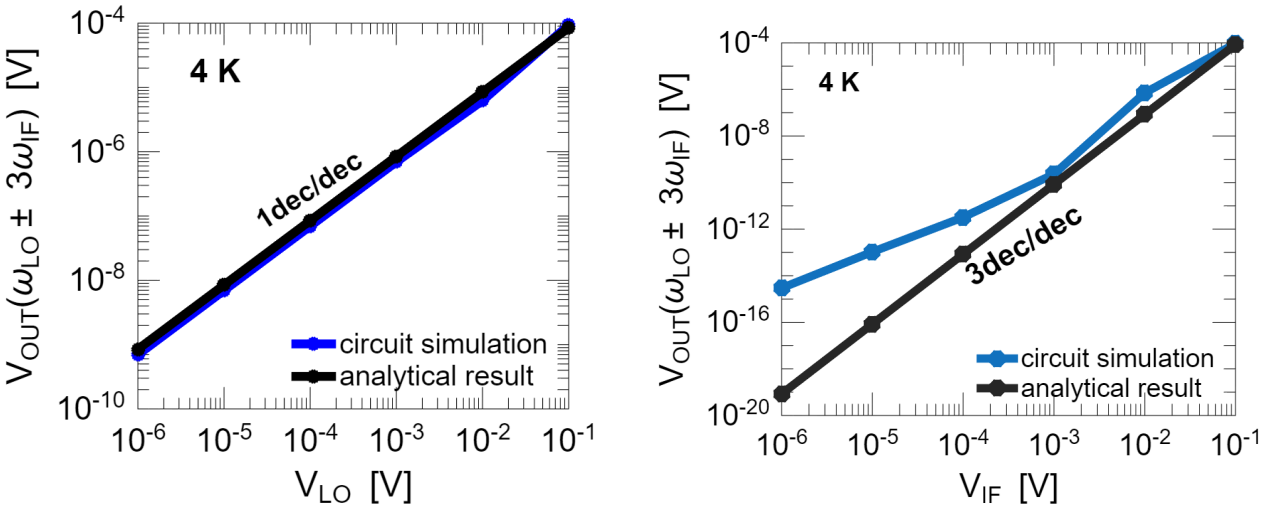
(a) (b)

Figure 3.3.5: Amplitude of the intermodulation product at $\omega_{LO} \pm \omega_{IF}$ versus V_{LO} (**a**) and V_{IF} (**b**) for $V_{IF} = 100\,\text{mV}$ and $V_{LO} = 100\,\text{mV}$, respectively, at 4 K.



(a) (b)

Figure 3.3.6: Amplitude of the third-order intermodulation product at $3\omega_{LO} \pm \omega_{IF}$ versus V_{LO} (**a**) and V_{IF} (**b**) for $V_{IF} = 100\,\text{mV}$ and $V_{LO} = 100\,\text{mV}$, respectively, at 4 K.



(a) (b)

Figure 3.3.7: Amplitude of the third-order intermodulation product at $\omega_{LO} \pm 3\omega_{IF}$ versus V_{LO} (**a**) and V_{IF} (**b**) for $V_{IF} = 100\,\text{mV}$ and $V_{LO} = 100\,\text{mV}$, respectively, at 4 K.

The figures show, overall, a good agreement between calculated and simulated amplitudes. In particular, in agreement with Equation (3.3.44), both at RT and CT, the simulated amplitudes of the tones at frequencies $\omega_{LO} \pm \omega_{IF}$ exhibit a linear dependence on the amplitude of the sweeping tone. Similarly, in agreement with Equations (3.3.45) and (3.3.46), both at RT and CT, the simulated amplitudes of the tones at frequencies $\omega_{LO} \pm 3\omega_{IF}$ and $3\omega_{LO} \pm \omega_{IF}$, respectively, exhibit a linear dependence on the amplitude of the sweeping LO and IF, respectively, and a cubic dependence on the amplitude of the sweeping IF and LO, respectively. Nevertheles some disagreement between the analytical model and the circuit simulation have to be stressed out. Regardless of the temperature, when the V_{LO} (V_{IF}) sweeps, for V_{LO} (V_{IF}) lower than $10^{-4}V$ ($10^{-3}V$) we observe an error on the amplitudes at frequencies $V_{OUT}(3\omega_{LO} \pm \omega_{IF})(V_{OUT}(\omega_{LO} \pm 3\omega_{IF}))$. It seems therefore that when the sweeping tone (V_{LO}, V_{IF}) contributes by its third harmonic ($3\omega_{LO}$, $3\omega_{IF}$), circuit simulations are more prove to suffer from some numerical error for lower amplitudes. Indeed, when the sweeping tone contributes by its fundamental harmonic (ω_{LO}, ω_{IF}) error is no longer observed. In addition, it should be pointed out that at $4K$ for the tones at frequencies $\omega_{LO} \pm 3\omega_{IF}$ and $3\omega_{LO} \pm \omega_{IF}$ circuit simulations and analytical results appear weakly shifted. In our opinion, this can be ascribed to the fact of having adopted for the HBT at 4 K the exponential dependence of the collector current I_C on the base-emitter voltage V_{BE}:

$$I_C \approx I_{Cs} e^{\frac{V_{BE}}{\eta V_{th}}} \tag{3.3.47}$$

on which the proposed analytical modeling is founded. Neverthless this relationship between I_C and V_{BE} is based on a Drift-Diffusion (DD) charge transport mechanism while in the cryogenic HBT tunneling is dominant (see Section 1.3).

Indeed the DD-based exponential dependence above was applied to the cryogenic HBT but at the cost of using an abnormally high value of η, which should be regarded just like a fitting parameter.

This remark calls for the need of a more specific compact modeling for the cryogenic HBT, that moves from the microscopic tunnelling based charge transport from the emitter to the collector of the HBT. It worth here pointing out that the Bardin Thesys is still today relevant starting point[26].

3.3.2 SFDR analytical evaluation

The Spurious Free Dynamic Range (SFDR) is defined as the ratio between the power of the output desired tone (second order intermodulation product for a mixer) and the power of the highest harmonic distortion in the output spectrum, reported in dBc (dB respect to the carrier). In terms of signal amplitudes we introduce SFDR by the following formula:

$$SFDR = 20 \log_{10} \left[\frac{A_\omega}{\max\left(A_{k\omega}\right)} \right] \tag{3.3.48}$$

where A_ω is the amplitude of the second order intermodulation product at the frequency $\omega_{IF} \pm \omega_{LO}$, the $\max\left(A_{k\omega}\right)$ is highest $A_{k\omega}$, $A_{k\omega}$ being a generical higher order intermodulation product.
Equations (3.3.44), (3.3.45) and (3.3.46) can lead to a mathematical expression of SFDR. To this aim, it is useful introducing the following constant:

$$K_1 = \frac{1}{2\eta V_{th} + R_1 I_0} \frac{I_E}{2\eta V_{th} + R_2 I_E} \tag{3.3.49}$$

$$K_2 = \frac{\eta V_{th}}{(2\eta V_{th} + R_1 I_0)^4} \frac{I_E}{2\eta V_{th} + R_2 I_E} \tag{3.3.50}$$

$$K_3 = \frac{I_E \eta V_{th}}{(2\eta V_{th} + R_2 I_E)^4} \frac{1}{2\eta V_{th} + R_1 I_0} \tag{3.3.51}$$

so that we can rewrite Equations (3.3.44), (3.3.45) and (3.3.46) as follows:

$$V_{OUT}(\omega_{LO} \pm \omega_{IF}) = \frac{R_L}{2} K_1 V_{LO} V_{IF} - \frac{R_L}{4} K_2 V_{LO}^3 V_{IF} - \frac{R_L}{4} K_3 V_{LO} V_{IF}^3 \tag{3.3.52}$$

$$V_{OUT}(3\omega_{LO} \pm \omega_{IF}) = -\frac{R_L}{12} K_2 V_{LO}^3 V_{IF} \tag{3.3.53}$$

$$V_{OUT}(\omega_{LO} \pm 3\omega_{IF}) = -\frac{R_L}{12} K_3 V_{LO} V_{IF}^3 \tag{3.3.54}$$

$$\tag{3.3.55}$$

Let suppose that the higher harmonic in the spectrum is $V_{OUT}(\omega_{LO} \pm 3\omega_{IF})$, then the SFDR expression is:

$$\begin{aligned} SFDR_1 &= 20 \log_{10} \left(\left| \frac{\frac{R_L}{2} K_1 V_{LO} V_{IF} - \frac{R_L}{4} K_2 V_{LO}^3 V_{IF} - \frac{R_L}{4} K_3 V_{LO} V_{IF}^3}{\frac{R_L}{12} K 2 V_{LO}^3 V_{IF}} \right| \right) = \\ &= 20 \log \left[\left| 6 \frac{K_1}{K_2 V_{LO}^2} - 3 \left(\frac{K_3 V_{IF}^2}{K_2 V_{LO}^2} + 1 \right) \right| \right] \end{aligned} \tag{3.3.56}$$

From Equations (3.3.49)-(3.3.51) it results:

$$\frac{K_1}{K_2} = \frac{(2\eta V_{th} + R_1 I_0)^3}{\eta V_{th}} \tag{3.3.57}$$

$$\frac{K_3}{K_2} = \frac{(2\eta V_{th} + R_1 I_0)^3}{(2\eta V_{th} + R_2 I_E)^3} \tag{3.3.58}$$

So, substituting Equations (3.3.57) and (3.3.58) into Equation (3.3.56) yields:

$$SFDR_1 = 20 \log_{10} \left\{ \left| 6 \frac{(2\eta V_{th} + R_1 I_0)^3}{\eta V_{th} V_{LO}^2} - 3 \left[\frac{(2\eta V_{th} + R_1 I_0)^3 V_{IF}^2}{(2\eta V_{th} + R_2 I_E)^3 V_{LO}^2} + 1 \right] \right| \right\} \tag{3.3.59}$$

Now, let suppose that the higher harmonic is $V_{OUT}(3\omega_{LO} \pm \omega_{IF})$. We can rewrite Equation (3.3.56) as:

$$\begin{aligned} SFDR_2 &= 20 \log_{10} \left(\left| \frac{\frac{R_L}{2} K_1 V_{LO} V_{IF} - \frac{R_L}{4} K_2 V_{LO}^3 V_{IF} - \frac{R_L}{4} K_3 V_{LO} V_{IF}^3}{\frac{R_L}{12} K_3 V_{IF}^3 V_{LO}} \right| \right) = \\ &= 20 \log \left| 6 \frac{K_1}{K_3 V_{IF}^2} - 3 \left(\frac{K_2 V_{LO}^2}{K_3 V_{IF}^2} + 1 \right) \right| \end{aligned} \tag{3.3.60}$$

Now, we can evaluate the expression $\frac{K_1}{K3}$ that will result:

$$\frac{K_1}{K_3} = \frac{(2\eta V_{th} + R_2 I_E)^3}{\eta V_{th}} \tag{3.3.61}$$

The SFDR in that case will be:

$$SFDR_2 = 20\log_{10}\left\{\left|6\frac{(2\eta V_{th} + R_2 I_E)^3}{\eta V_{th} V_{IF}^2} - 3\left[\frac{(2\eta V_{th} + R_2 I_E)^3 V_{LO}^2}{(2\eta V_{th} + R_1 I_0)^3 V_{IF}^2} + 1\right]\right|\right\} \tag{3.3.62}$$

We take as $SFDR$ the worst case between $SFDR_1$ and $SFDR_2$:

$$SFDR = MIN(SFDR_1, SFDR_2) \tag{3.3.63}$$

Since the emitter degeneration resistors R_1 and R_2 impacts on the linearity, SDFR has been calculated for $V_{IF} = V_{LO} = 100mV$ by adopting the values in Tables 3.1,3.2,3.3 except for the degeneration resistors. First R_1 has been swept by keeping R_2 constant (800Ω) and then R_2 has been swept by keeping R_1 constant (800Ω). Figures 3.3.8 and 3.3.9 depict, respectively, the obtained results at RT.

The figure points out that $SFDR_1$ ($SFDR_2$), linked to intermodulation product at frequency $\omega_{IF} \pm 3\omega_{LO}$ ($3\omega_{IF} \pm \omega_{LO}$), determines the SFDR for R_1 (R_2) lower than about 800Ω, in agreement with R_1 (R_2) and ω_{LO} (ω_{IF}) being present in the first (second) section of the Gilbert multiplier. Similar results were obtained at CT.

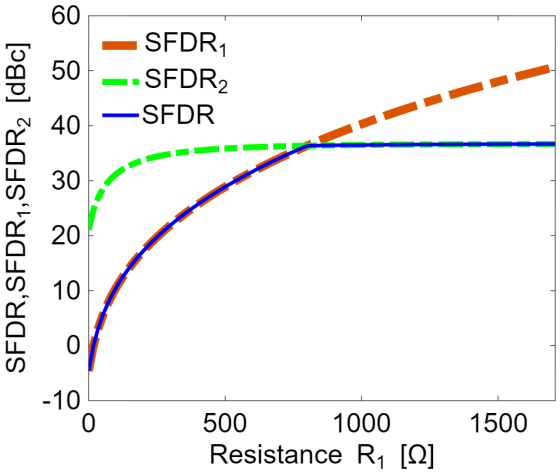


Figure 3.3.8: SFDR vs R_1 at 300K

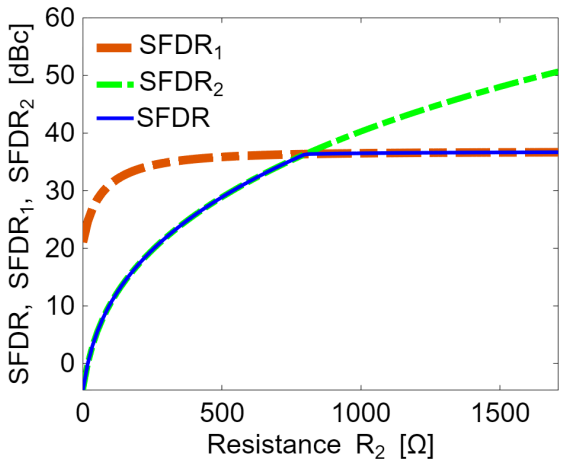


Figure 3.3.9: SFDR vs R_2 at 300K

We can see that $SFDR_1$ ($SFDR_2$) curve increase linearly until it crosses the $SFDR_2$ ($SFDR_1$) curve.

According to Equation (3.3.63) $SFDR_2$ ($SFDR_1$) curve exhibit two different slopes. In both the Figures we can recognise the point in which the SFDR become negative as recovered by the previous equations.
Another calculation was carried out by sweeping both the resistances. The Figure 3.3.10 shows the obtained result.

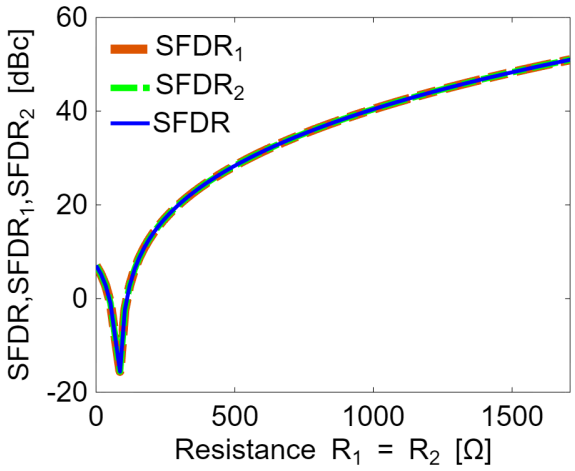


Figure 3.3.10: SFDR vs $R_1 = R_2$ at 300K

Same simulations as before were carried $4K$. In this case, the maximum value of resistance for $R_1 I_0 = 200mV$ is $R_1 = 823\Omega$. Figures 3.3.11-3.3.13 show the obtained results.

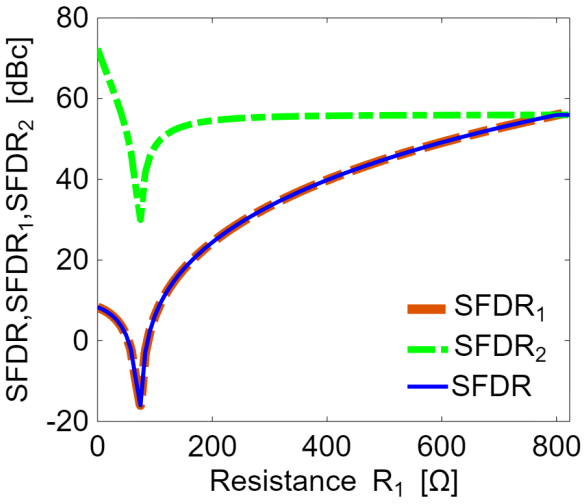


Figure 3.3.11: SFDR vs R_1 at $4K$

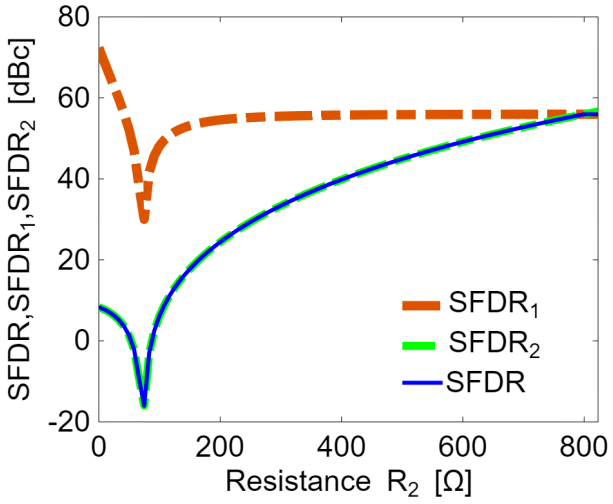


Figure 3.3.12: SFDR vs R_2 at $4K$

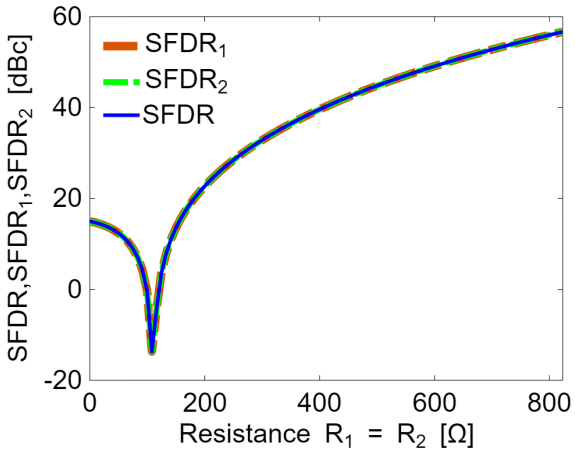
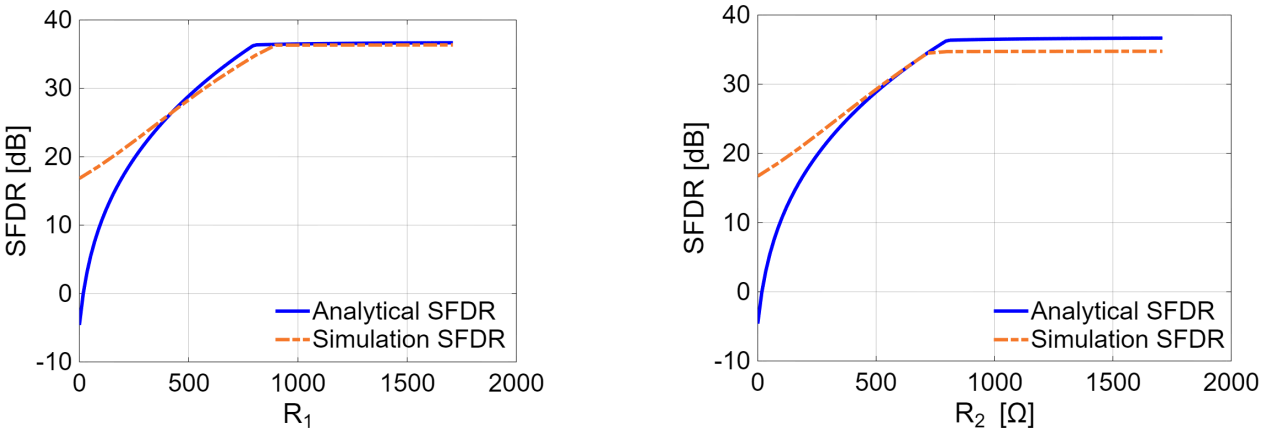


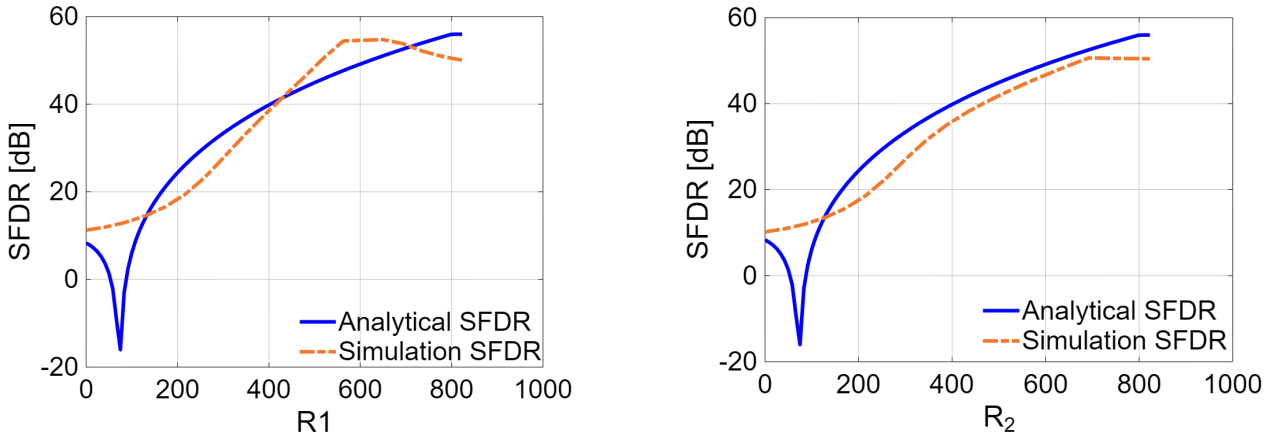
Figure 3.3.13: SFDR vs $R_1 = R_2$ at $4K$

Same investigations as before were been carried out by transient circuit simulations. All the curves shows the minimum point in which the SFDR become nagative. The following figures compare the obtained results with the previous analytical results:



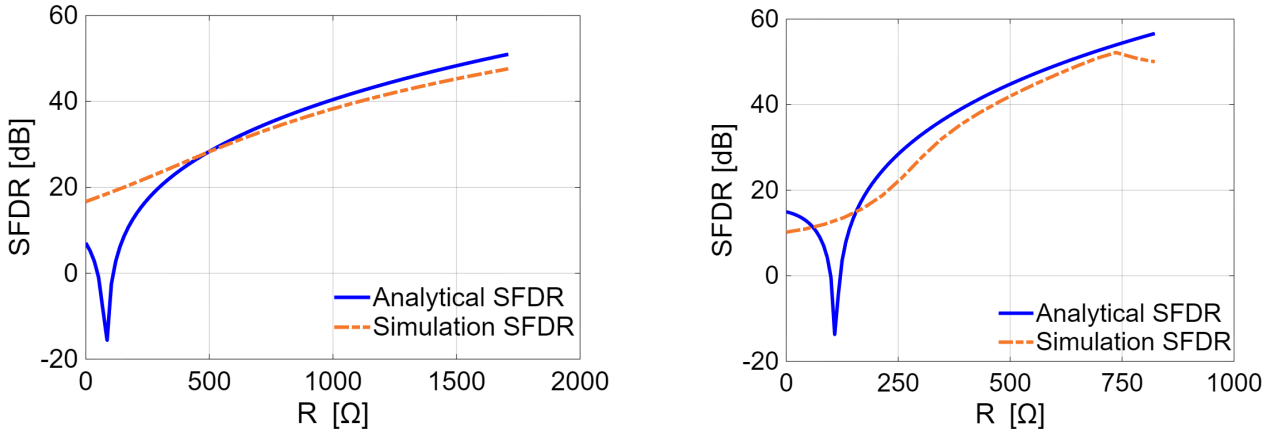
(a) (b)

Figure 3.3.14: Analytical and simulated SFDR vs R_1 at $300K$ (**a**), or Analytical and simulated SFDR vs R_2 at $300K$ (**b**)



(a) (b)

Figure 3.3.15: Analytical and simulated SFDR vs R_1 at $4K$ (**a**), or Analytical and simulated SFDR vs R_2 at $4K$ (**b**)



(a) (b)

Figure 3.3.16: Analytical and simulated SFDR vs $R_1 = R_2 = R$ at 300 K (**a**) and 4 K (**b**)

Figures 3.3.14 and 3.3.15 show that SFDR is negative, that is $|a_1|$ is lower than $|a_3|$, for low enough values of the degeneration resistors. Figures 3.3.8 and 3.3.9 show, respectively, that in these intervals the SFDR is set by $SFDR_1$ and $SFDR_2$. When R_1 sweeps, while R_2 is kept constant at 800Ω, the edge values of R_1, for which $|a_1| = |a_3|$, can be calculated from Equation (3.3.59) as follows:

$$\left[\frac{2}{\eta V_{th} V_{LO}^2} - \frac{V_{IF}^2}{y^3 V_{LO}^2}\right] x^3 = \frac{2}{3} \tag{3.3.64}$$

$$\left[\frac{2}{\eta V_{th} V_{LO}^2} - \frac{V_{IF}^2}{y^3 V_{LO}^2}\right] x^3 = \frac{4}{3} \tag{3.3.65}$$

where $x \triangleq 2\eta V_{th} + R_1 I_0$ and $y \triangleq 2\eta V_{th} + R_2 I_E$. Using the parameters in Tables 3.1, 3.2, and 3.3, Equations (3.3.64) and (3.3.65) yield edge values of $R_1 \simeq -86.4\Omega$ and $R_1 \simeq 15.9\Omega$ ($R_1 \simeq 53.5\Omega$ and $R_1 \simeq 86.9\Omega$) at RT (CT). Beacause of mathematical symmetry between Equations (3.3.59) and (3.3.62), the same values apply to R_2 when $R_1 = 800\Omega$ is fixed. For $R = R_1 = R_2$, as in Figure 3.3.16, the edge values are $R \simeq 46.7\Omega$ and $R \simeq 109.2\Omega$ ($R \simeq 99.2\Omega$ and $R \simeq 119.9\Omega$) at RT (CT). Each of Equations (3.3.64) and (3.3.65) also has a pair of complex-conjugate solutions, discussed in Appendix B. A vertical asymptote occurs at the minimum shown in the figures above. When R_1 is swept while R_2 is kept constant at $800\,\Omega$, the value of R_1 for which $\frac{a_1}{a_3} = 0$ can be calculated as follows:

$$\left[\frac{2}{\eta V_{th} V_{LO}^2} - \frac{V_{IF}^2}{y^3 V_{LO}^2}\right] x^3 = 1 \tag{3.3.66}$$

As in the previous case, this yields one real solution and two complex-conjugate solutions. The real solution of Equation 3.3.66, using the parameters in Tables 3.1, 3.2, and 3.3, result to $R_1 \simeq -29.4\,\Omega$ ($R_1 \simeq 72.1\,\Omega$) at RT (CT). For the case in which $R = R_1 = R_2$ the value correspond to $R \simeq 79.7\Omega$ ($R \simeq 110.1\Omega$) at RT (CT). The complex-conjugate solutions can instead be calculated analytically, as discussed in Appendix B. Overall, the analytical model provides a good estimate of the simulated SFDR. This agreement is particularly relevant because SFDR is an important parameter for accurate qubit control (see Section 1.2). For $R_1 = R_2 = 800\Omega$, a closer comparison between analytical and simulated SFDR values is carried out. According to the definition of SFDR reported in Equation (3.3.48), the table 3.12 reports values calcutated from the results obtained in Section 3.3.1, while Table 3.13 report the values from the circuit simulations for with $V_{IF} = V_{LO} = 100mV$:

Temp [K]	A_ω [mV]	$A_{k\omega}$ [mV]	**SFDR**
300	47.99	0.730	36.357
4	53.264	0.085	55.940

Table 3.12: SFDR from analytical model

Temp [K]	A_ω [mV]	$A_{k\omega}$ [mV]	**SFDR**
300	44.132	0.816	34.661
4	53.140	0.160	50.420

Table 3.13: SFDR from circuit simulation

The table shows that the analytical model overestimates the SFDR with a relative error of about 5% (10%) at 300 K (4 K).

3.4 Jones demodulator

In the Jones demodulator, whose basic schematic is depicted in Figure 3.4.1, the switching activity of the transistors M1÷M4 generates intermodulation products of frequencies $mf_{LO} \pm nf_{IF}$ where both m and n are integers [15]. The circuit can be splitted into the three sections highlighted in the figure. It is worth noticing that the transconductor section is the same circuit investigated in Section 2.3.

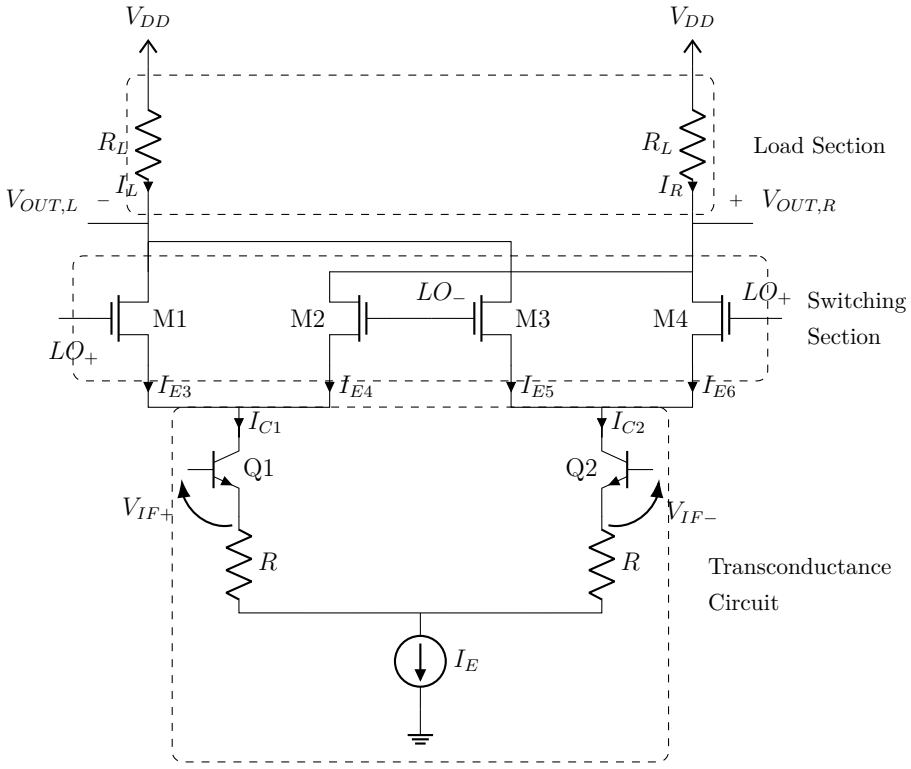


Figure 3.4.1: Jones schematic

The switching section, is driven by the LO_+ and LO_- square wave signals, oscillating between $0V$ and V_G. When LO_+ is high, M1 and M4 are ON, while, M2 and M3 are OFF. The current I_L (I_R) flowing through the left (right) load resistor R_L is thus I_{C1} (I_{C2}). The output differential current, defined as $\Delta I_{LR} = I_L - I_R$, is equal to $\Delta I_{12} = I_{C1} - I_{C2}$ and the differential output voltage, defined as $V_{OUT,L} - V_{OUT,R}$, is equal to $R_L(I_L - I_R) = R_L \Delta I_{12}$. When, instead, LO_- is high, M1 and M4 are OFF, while, M2 and M3 are ON. The current flowing through the left (right) load resistor R_L is now I_{C2} (I_{C1}). In this case $\Delta I_{LR} = I_{C2} - I_{C1} = -\Delta I_{12}$ and $V_{OUT} = -R_L \Delta I_{12}$. By indicating with f_{LO} the oscillating frequency of the signals driving the switching transistors, the output differential voltage V_{OUT} behaves thus in the time domain as depicted in Figure 3.4.2.

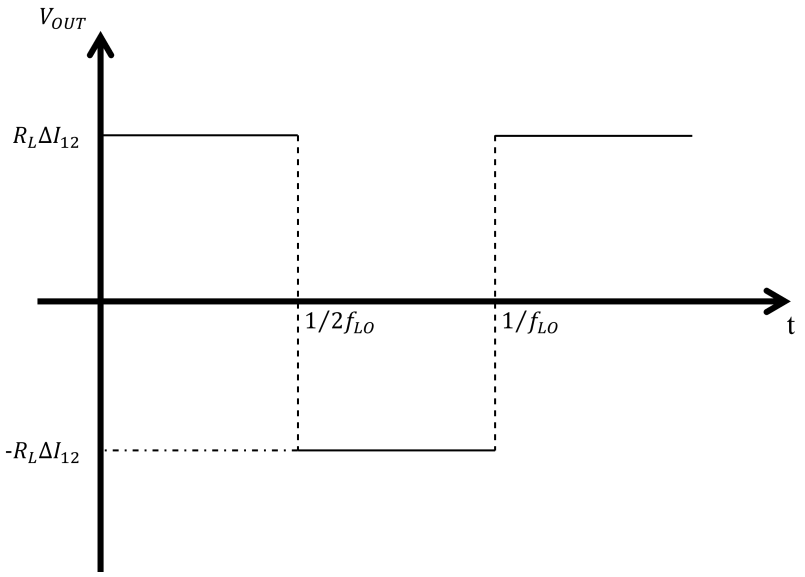


Figure 3.4.2: Representation of differential output current at load of circuit 3.4.1

It is a square wave of peak amplitude $V_{OUT,peak} \triangleq R_L\Delta I_{12}$, whose Fourier series is [15]:

$$\Delta V_{OUT}(t) = R_L\Delta I_{12}\frac{4}{\pi}\sum_{n=0}^{+\infty}\frac{\sin\left[(2n+1)\,\omega_{LO}t\right]}{(2n+1)} \tag{3.4.1}$$

Instead, for the transconductance section composed by Q1 and Q2, its behaviour is described according to Section 2.1. By reminding the approximated closed form of ΔI_{12} obtained in Chapter 2 we can write:

$$\Delta V_{OUT}(t) = \frac{4}{\pi}R_L\left[a_1\,\cos\left(\omega_{IF}t\right) + a_3\cos\left(3\omega_{IF}t\right)\right]\left\{\sum_{n=0}^{+\infty}\frac{\sin\left[(2n+1)\,\omega_{LO}t\right]}{(2n+1)}\right\} \tag{3.4.2}$$

where a_1 and a_3 are:

$$a_1 \triangleq \frac{\frac{I_0}{2\eta V_{th}}}{1+\frac{RI_0}{2V_{th}}}\Delta V_{IN} - 3\frac{I_0}{96(\eta V_{th})^3}\,\frac{1}{\left(1+\dfrac{I_0R}{2\eta V_{th}}\right)^4}\Delta V_{IN}^3 \tag{3.4.3}$$

$$a_3 \triangleq -\frac{I_0}{96(\eta V_{th})^3}\,\frac{1}{\left(1+\dfrac{I_0R}{2\eta V_{th}}\right)^4}\Delta V_{IN}^3 \tag{3.4.4}$$

By recalling the trigonometric identity $\sin(\alpha)\cos(\beta) = \dfrac{\sin(\alpha-\beta)+\sin(\alpha+\beta)}{2}$, Equation (3.4.2) yields:

$$\Delta V_{OUT}(t) = \frac{2}{\pi} R_L a_1 \left\{ \sum_{n=0}^{+\infty} \frac{\sin[(2n+1)\,\omega_{LO} + \omega_{IF}]\,t}{2n+1} + \frac{\sin[(2n+1)\,\omega_{LO} - \omega_{IF}]\,t}{2n+1} \right\} + \frac{2}{\pi} R_L a_3 \left\{ \sum_{n=0}^{+\infty} \frac{\sin[(2n+1)\,\omega_{LO} + 3\omega_{IF}]\,t}{2n+1} + \frac{\sin[(2n+1)\,\omega_{LO} - 3\omega_{IF}]\,t}{2n+1} \right\} \quad (3.4.5)$$

Considering the Equation (3.4.5) till $n = 1$, in order to compare the resulting harmonics with the ones obtained also in the circuit in Figure 3.2.1, leads to the following second order ($V_{OUT_{11}}$) and fourth order ($V_{OUT_{13}}, V_{OUT_{31}}$) intermodulation product in the output signal V_{OUT}:

$$\Delta V_{OUT_{11}}(t) = \frac{2}{\pi} R_L a_1 \sin[(\omega_{LO} \pm \omega_{IF})\,t] \quad (3.4.6)$$

$$\Delta V_{OUT_{13}}(t) = \frac{2}{\pi} a_3 \sin[(\omega_{LO} \pm 3\omega_{IF})\,t] \quad (3.4.7)$$

$$\Delta V_{OUT_{31}}(t) = \frac{2}{\pi} R_L a_1 \frac{1}{3} \sin[(3\omega_{LO} \pm \omega_{IF})\,t] \quad (3.4.8)$$

$$\Delta V_{OUT_{33}}(t) = \frac{2}{3\pi} R_L a_3 \sin[(3\omega_{LO} \pm 3\omega_{IF})\,t] = \Delta V_{OUT_{33}} \sin[(3\omega_{LO} \pm 3\omega_{IF})\,t] \quad (3.4.9)$$

3.5 Analytical evaluation and simulation result

The simulated circuit was implemented using SG13G2 130nm SiGe BiCMOS technology by IHP in order to verify the obtained analytical results. In Figure 3.5.1 a cosinusoidal input voltage is applied to the transconductance circuit, while, unlike in Figure 3.5.1, the upper quad (M1,M2,M3,M4) is driven by a square wave so that the transistors operate in switching mode as described in Section 3.4:

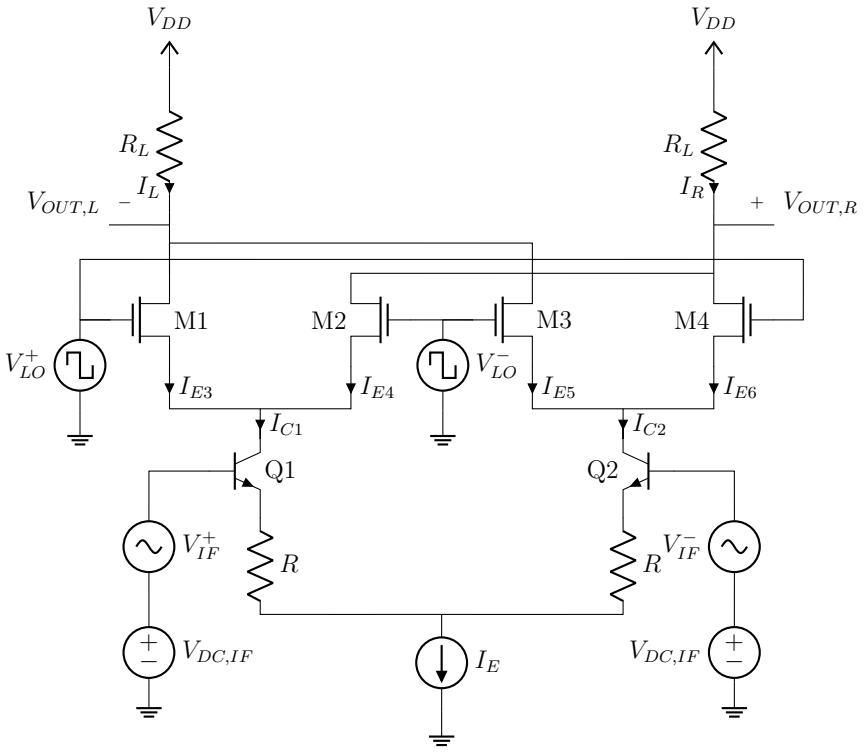


Figure 3.5.1: Jones schematic implemented using IHP technology

Table 3.14 reports the transistor sizes, table 3.14 resistor and bias voltages and current and Table 3.15 signal amplitudes and frequencies. Substituting these values into Equations (3.4.6), (3.4.7) and (3.4.8) leads to the amplitudes in the 3.16.

Temp [K]	$W_{MOS}\,[\mu m]$	$L_{MOS}\ [nm]$	n_1	$W_{HBT}\,[nm]$	$L_{HBT}\ [nm]$	m_1
300	12.45	130	10	70	900	1
4	12.45	130	10	70	900	1

Table 3.14: Transistor sizes for different temperature. n_1 define the number of gates in the MOS, instead, m_1 the number of emitter

Temp [K]	$V_{DD}\,[V]$	$V_{DC,IF}\,[V]$	$R_L\,[\Omega]$	$R\ [\Omega]$	$I_E\,[\mu A]$
300	1.6	1.2	2000	800	117
4	1.6	1.2	2000	800	243

Table 3.15: Circuit bias for different temperature.

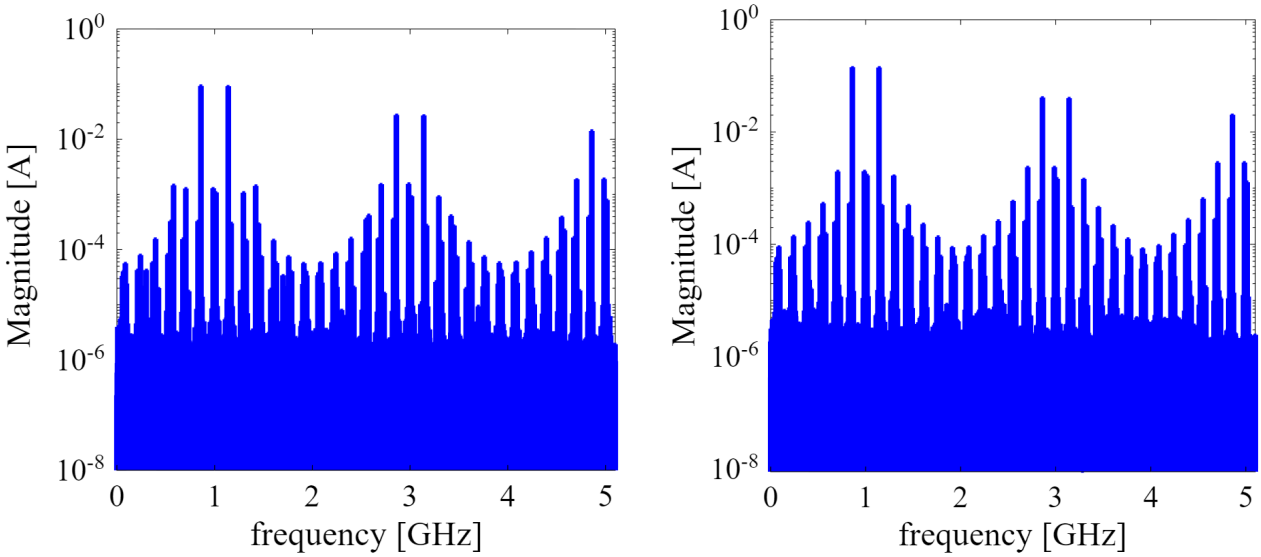
Temp [K]	$V_{LO,min}$ $[V]$	$V_{LO,max}$ $[V]$	V_{IF} $[mV]$	f_{LO} $[GHz]$	f_{IF} $[MHz]$
300	0	1.6	100	1	140
4	0	1.6	100	1	140

Table 3.16: Input signals for different temperature.

Temperature [K]	$V_{OUT_{11}}$ $[mV]$	$V_{OUT_{31}}$ $[mV]$	$V_{OUT_{13}}$ $[mV]$
300	95.362	31.787	1.387
4	144.843	48.281	0.231

Table 3.17: Amplitudes calculated from the analitical model.

These amplitudes have been compared with the amplitudes from the simulated spectra in Figure 3.5.2a and 3.5.2b.



(a) (b)

Figure 3.5.2: Spectrum of switching architecture mixer with HBT transconductor and switching MOSFET load at 300K (**a**) and 4K (**b**)

Table 3.18 reports the amplitudes of interest.

Temperature [K]	$\omega_{LO} \pm \omega_{IF}$ $[mV]$	$3\omega_{LO} \pm \omega_{IF}$ $[mV]$	$3\omega_{LO} \pm \omega_{IF}$ $[mV]$
300	92.870	27.60	1.433
4	142.406	41.079	0.185

Table 3.18: Amplitude from the circuit simulation

Table 3.19 compare simulated and calculated amplitudes.

Temp [K]	**Simulated [mV]**	**Analytical [mV]**	**Err. [%]**
	$V_{OUT_{11}}$		
300	92.870	95.362	-2.68
4	142.406	144.843	-2.44
	$V_{OUT_{13}}$		
300	1.433	1.387	3.2
4	0.185	0.231	-24.86
	$V_{OUT_{31}}$		
300	27.60	31.787	-15.17
4	41.079	48.281	-17.53

Table 3.19: Comparison between analytical and simulated amplitudes

The error between simulation and analytical results is calculated as in the following equation:

$$Error[\%] = 100\frac{A_{sim} - A_{analytic}}{A_{sim}} \tag{3.5.1}$$

where A_{sim} refer to the amplitude of the signal obtained from the circuit simulation and $A_{analytic}$ the amplitude obtained from analytical model at the frequency of interest. Again, as already observed for the Gilbert multiplier, the error is more pronounced for simulations carried at 4 K.

3.5.1 SFDR in classical switching topology

As in Section 3.3.2, we analytically evaluate the SFDR of the mixer starting from the spectral components given in Equations (3.4.6), (3.4.7), and (3.4.8). From the amplitudes of these intermodulation products, it is possible to calculate the following SFDR:

$$SFDR_1 = 20\log_{10}\frac{\Delta V_{OUT_{11}}}{\Delta V_{OUT_{13}}} = 20\log_{10}\left|\frac{a_1}{a_3}\right| \tag{3.5.2}$$

$$SFDR_2 = 20\log_{10}\frac{\Delta V_{OUT_{11}}}{\Delta V_{OUT_{31}}} = 20\log_{10} 3 = 9.542dB \tag{3.5.3}$$

$$SFDR_3 = 20\log_{10}\frac{\Delta V_{OUT_{11}}}{\Delta V_{OUT_{33}}} = 20\log_{10}\left|\frac{3a_1}{a_3}\right| = SFDR_1 + SFDR_2 \tag{3.5.4}$$

Investigating the SFDR achievable using the Jones demodulator, we find that $SFDR_2$ represent the maximum SFDR attainable with this topology.Furthermore, the interval over which the $SFDR_1$ is positive defined coincides with the intervals defined in Equations 2.1.49 and 2.1.50 in the degenerated differential couple. Equation (3.5.4) shows that, according to the definition of SFDR given in Equation (3.3.63), $SFDR_3$ can be ruled out in the evaluation of the SFDR. On the other hand, because of Equations (3.4.3) and (3.4.4) we can write:

$$\left|\frac{a_1}{a_3}\right| = \left|\frac{\frac{I_E\Delta V_{IN}}{2\eta V_{th}+RI_E} + 3a_3}{a_3}\right| = \left|3 + \frac{1}{a_3}\frac{I_E\Delta V_{IN}}{2\eta V_{th} + RI_E}\right| \tag{3.5.5}$$

The ratio between (3.4.3) and (3.4.4) is constant and equal to three, leading to:

$$SFDR_2 = 20\log_{10}(3) = 9.542 \text{ dBc} \tag{3.5.6}$$

Table 3.20 analytical and simulated SFDR shows a good agreement between:

Temperature [K]	Analytical SFDR $[dBc]$	Simulation SFDR$[mV]$	Error %
300	9.542	10.539	10.448
4	9.542	10.798	13.164

Table 3.20: Comparison of SFDR.

3.6 Circuit comparison in short

3.6.1 SFDR obtained from analytical model

Concerning the Gilbert multiplier (see figure 3.2.1), Table 3.21 reports the SFDR obtained from the analytical model where A_ω is the amplitude of the fundamental tone and $A_{k\omega}$ the amplitude of the highest armonics present in the output spectrum.

Temp [K]	A_ω $[V]$	$A_{k\omega}$ $[V]$	**SFDR** $[dBc]$
300	47.99	0.730	36.357
4	53.264	0.085	55.94

Table 3.21: SFDR extrapolated from the analytical model of the multiplier for $V_{IF} = V_{LO} = 100mV$ (see Tables 3.4-3.7).

The resulting SFDR improves by decreasing the temperature. As for the Jones demodulator (see figure 3.4.1), Table 3.22 reports the SFDR obtained from the analytical model.

Temp [K]	A_ω $[mV]$	$A_{k\omega}$ $[mV]$	**SFDR** $[dBc]$
300	95.362	31.787	9.542
4	144.843	48.281	9.542

Table 3.22: SFDR obtained from the analytical model of the switching mixer for $V_{IF} = V_{LO} = 100mV$.

In this case, the SFDR is temperature indipendent. The two tables show that the Gilbert multiplier offers better SFDR, specially at 4 K.

3.6.2 SFDR obtained from the simulation

Tables 3.23 and 3.24 reports the SFDR obtained from the circuit simulations of the Gilbert multiplier and the Jones demodulator respectively.

Temp [K]	A_ω $[mV]$	$A_{k\omega}$ $[mV]$	**SFDR** $[dBc]$
300	43.944	0.833	34.445
4	53.518	0.159	50.54

Table 3.23: SFDR extrapolated from the simulated model of the multiplier for $V_{IF} = V_{LO} = 100mV$ (see Tables 3.8-3.11).

Temp [K]	A_ω $[V]$	$A_{k\omega}$ $[V]$	**SFDR** $[dBc]$
300	92.870	27.60	10.539
4	142.406	41.079	10.798

Table 3.24: SFDR extrapolated from the simulated model of the switching mixer for $V_{IF} = V_{LO} = 100mV$.

The simulation results in fair good agreements with the analytical results in Table 3.21 and 3.22.

3.7 Final Consideration

The comparison between the analytical calculations and the Cadence simulations shows an overall good agreement for the desired mixing products at $\omega_{LO} \pm \omega_{IF}$. In particular, their amplitude exhibits the expected linear dependence on both V_{LO} and V_{IF}, confirming the validity of the proposed analytical description in the considered input range. The higher-order products at $3\omega_{LO} \pm \omega_{IF}$ and $\omega_{LO} \pm 3\omega_{IF}$ also follow the predicted cubic dependence on the corresponding input amplitude. Small discrepancies are observed at very low input amplitudes and at 4 K, where the spectral components are close to the numerical limit of the FFT-based extraction and where the adopted exponential HBT model represents an approximation of the actual cryogenic device behaviour. Comparing the results obtained for the SFDR reported in Tables 3.21, 3.22, 3.23, and 3.24 reveals that the switching implementation generates harmonic components with higher amplitudes than the linear multiplier. Another consideration regarding the SFDR is that all the circuits achieve better results at lower temperature. In fact, at 4 K, the harmonic components are lower than at 300 K. This behaviour is mainly due to the higher transconductance exhibited by the devices at cryogenic temperature. Overall, the results confirm that the linear Gilbert multiplier offers a more favourable trade-off between frequency conversion and spectral purity than the switching Jones demodulator. The analytical model therefore provides a useful preliminary tool for selecting the input amplitudes, bias currents, and degeneration resistances before carrying out detailed circuit simulations.

4 RF Figure of Merit for the Gilbert multiplier

This chapter aims to completely characterize the Gilbert Multiplier at 300 K and 4 K using the Figure of Merits, reported in Section 1.2. The used simulation in Cadence Virtuoso were Periodic AC, Periodic Steady State, PNoise and S-parameter simulation. In the next section we will explain the simulation we have realized.

4.1 1 dB CP and IIP3

Figure 4.1.1 depicts schematic used to simulate the $1\,dB$ CP and IIP3. The input ports are connected to an ideal balun fed by a port. Also the output port is connected to a balun where at the output a third port is placed.

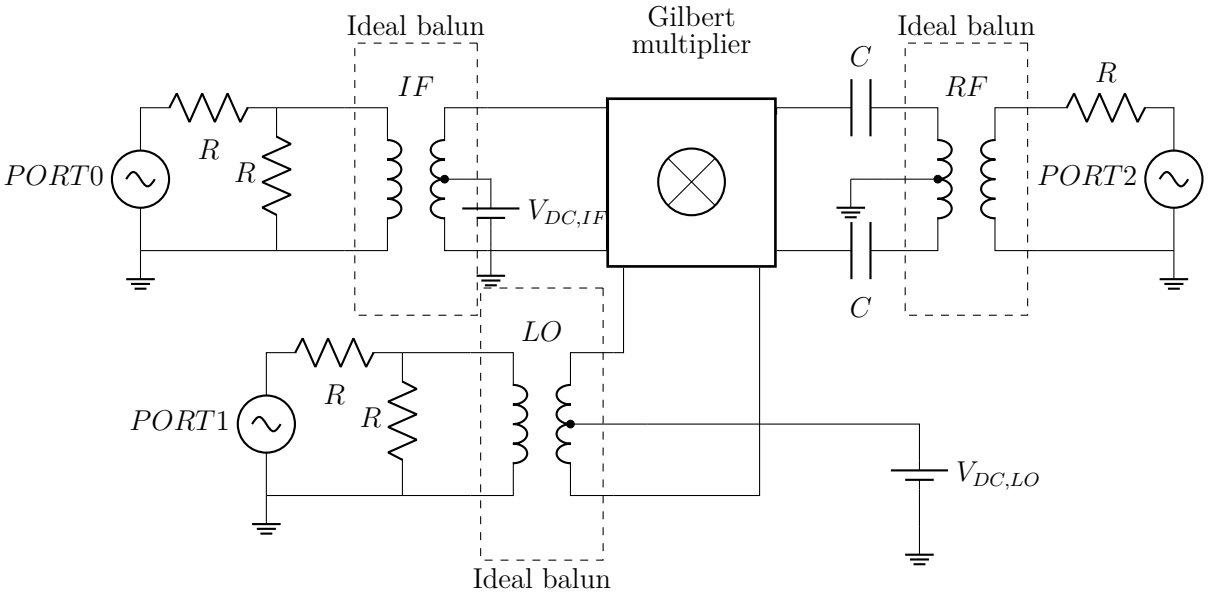


Figure 4.1.1: Test implementation

The Mixer internal components are kept with the same value as reported in Tables 3.1, 3.2 and 3.3.

The components reported in Figure 4.1.1 have the following values:

Temperature [K]	R [Ω]	C[pF]	$p_{lo}[dBm]$	f_{LO} [GHz]	$p_{if}[dBm]$	f_{IF} [MHz]
300	50	100	-10	1	-10	140
4	50	100	-10	1	-10	140

Table 4.1: Circuit parameters for AC simulations.

The Voltage conversion gain is obtained by means of a PSS+PAC simulation. The voltage conversion gain of an upconversion mixer is extracted by first computing the periodic steady-state operating point under large-signal local oscillator excitation (PSS), and then applying a small-signal perturbation at the baseband or IF input (PAC).
The conversion gain as a function of RF frequency is obtained by sweeping the input signal frequency and evaluating the ratio between the upconverted output voltage at the desired RF sideband and the applied input voltage. In this way, the frequency-dependent upconversion behavior of the mixer can be characterized, including gain variation across the RF band and the influence of the local oscillator-driven time-varying nonlinearities.

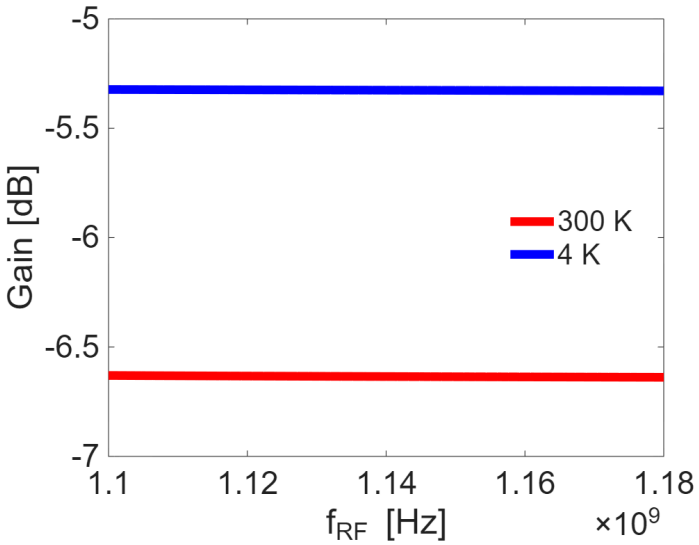


Figure 4.1.2: Output Gain versus f_{RF} frequency

The $1dB$ Compression Point is obtained by sweeping the p_{RF} $[dBm]$ power.

Selecting in the ADE plot window the Compression Point curve on the 1^{st} Order Harmonic and selecting the Output port, we obtain the curves in Figure 4.1.3:

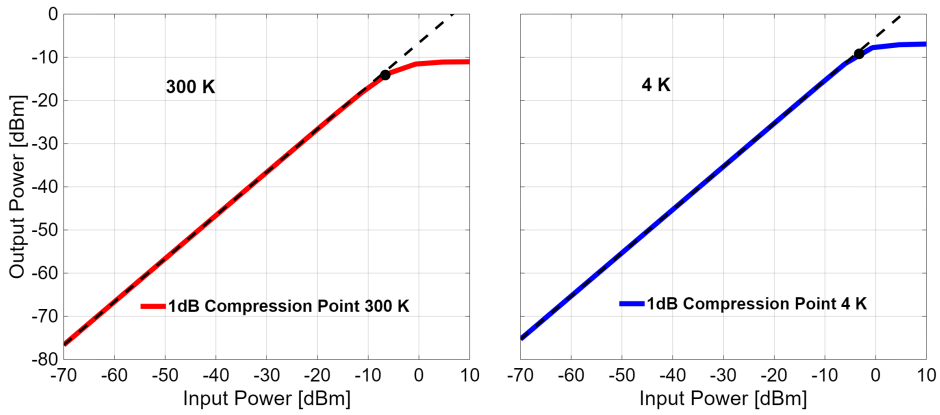


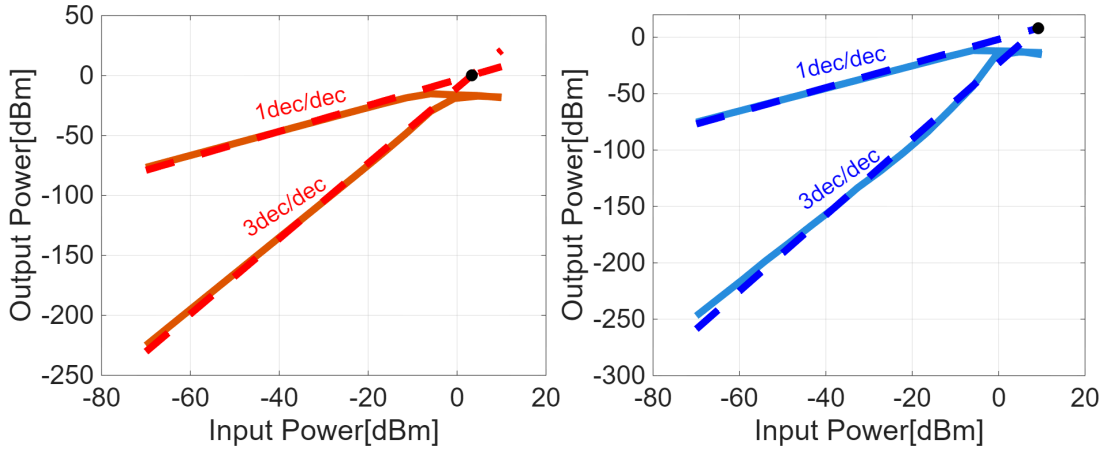
Figure 4.1.3: 1dB-Compression Point curves compared at 4K and 300K

The $1dB$ CP from the two curves shown in Figure 4.1.3 has the values in Table 4.2:

Temperature [K]	RF power for $1dB$ CP [dBm]
300	-6.60
4	-3.25

Table 4.2: Table 1dB compression point values at 300 K and 4 K

The $IIP3$, you can choose, in the ADE plot window, the function IPN curve. Selecting the two curve to be plotted, 3^{rd} Order Harmonic and the 1^{st} Order Harmonic and measure it at the output port, we obtained the curves in Figure 4.1.4.



(a) (b)

Figure 4.1.4: IIP3 curves at 300 K (**a**) and 4 K (**b**)

Temperature [K]	$IIP3$ [dBm]
300	3.32
4	9.13

Table 4.3: IIP3 at 4 K and 300 K

In a memoryless third-order non-linearity the relation between $IIP3$ and $1dB$ CP is:

$$\mathrm{IIP3} = \mathrm{P_{1dB}} + 9.46\,\mathrm{dB} \tag{4.1.1}$$

Substituiting the result obtained in $1dB$ CP simulation, and applying Equation (4.1.1) we can compared with the result obtained in the $IIP3$ simulation will be compared with the analytical one:

Temperature [K]	$IIP3$	memoryless $IIP3$
300	3.32	2.86
4	9.13	6.21

Table 4.4: Simulated and analytical IIP3 values at 300 K and 4 K

4.2 Noise Figure (NF)

This section presents the simulated NF of the Gilbert multiplier at 300 K and 4 K. As in all frequency downconverting electronics, the NF are two: Double Side Band (DSB) and Single Side Band (SSB). The simulation are realized on Cadence using PSS and PNoise simulation. The IF and RF port are set as DC port, instead, the LO port as a sine source. The PNoise simulation set the input port (RF port) as noise source, and measure at the output port (RF port) the spectral power for the signal and for the noise.
Figure 4.2.1 shows the obtained results:

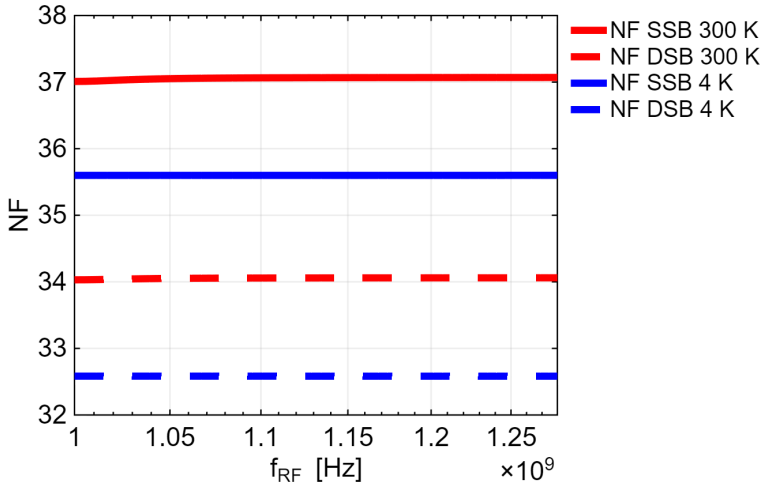


Figure 4.2.1: NF SSB compared to DSB for 300K and 4K model. The value is much higher than 1 dB because the gain is lower than 0dB

Figure shows that the difference between SSB NF and DSB NF, for the same input power p_{lo}, is equal to $3dBm$, as reported in Section 1. Moreove, the figure shows a slight improvement of NF at 4 K.

4.3 Port Isolation

The Port Isolation its evaluated using the S-parameter analysis. Starting from the PSS analysis, as beating we set the LO frequency and a PSP (Periodical S-Parameter) analysis with a sweeping frequency from 0 to 200 MHz. The frequency has to be inteded relative to the port. The RF port is set as a DC port as the output IF port.

Figure 4.3.1 shows the resulting port isolation at 300 K model are reported in figure below:

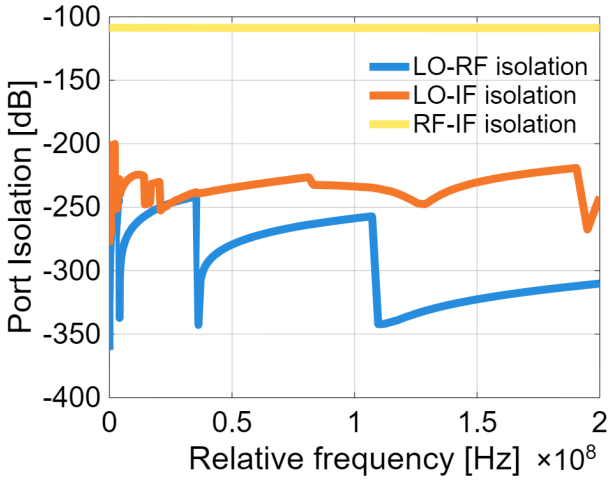


Figure 4.3.1: 300 K Port isolation between each port configuration

The y axis in each figures refer to the power of the signal measured at the output port divided to the input power signal. For the 4 K model the resulting curves are depicted in Figure 4.3.2:

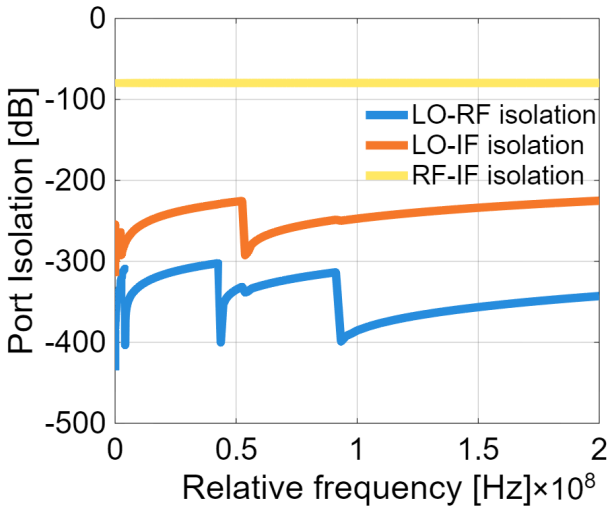


Figure 4.3.2: 4 K Port isolation between each port configuration

To confirm the result obtained in S-parameter simulation, we perform also a transient simulation. Then, we turn on only one input signal at time. Starting by applying LO signal with a constant power of -10 dBm, and keeping the IF and RF port as a DC ports, and plotting the signal at the input of each the remaining port.

Then we invert the simulation by imposing the IF signal as sinusoidal signal,with a constant power of -10 dBm, and LO port as DC port. Figure 4.3.3 and 4.3.4 show the obtained results.

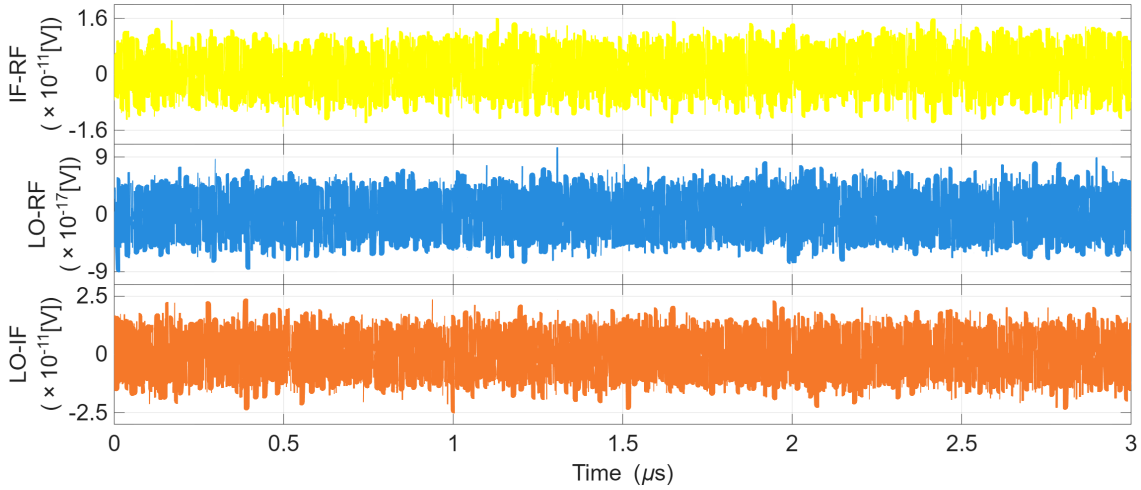


Figure 4.3.3: 300 K Output signal at each port. The y label P1-P2 refer respectively for input port where we inject signal, and output port in which we plot the signal

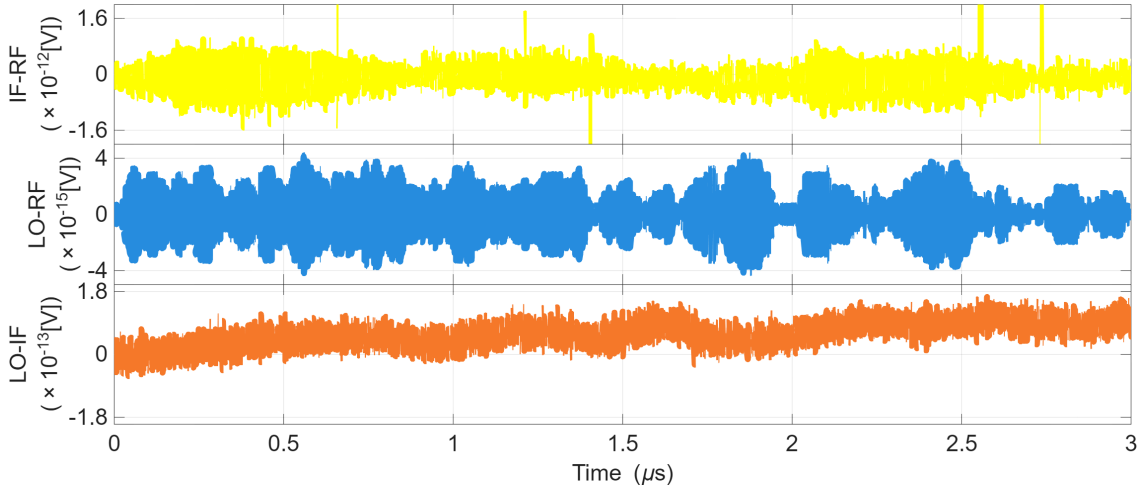


Figure 4.3.4: 4 K Output signal at each port. The y label P1-P2 refer respectively for input port where we inject signal, and output port in which we plot the signal

The magnitude obtained for each output signal divided by the input signal amplitude, gives results in the order of the port Isolation obtained in the Figures 4.3.1 and 4.3.2.
The high port isolation achieved in this architecture primarily arises from the intrinsic properties of the Gilbert cell. The local oscillator (LO) signal is effectively decoupled through capacitive coupling networks that feed the upper differential transistor pairs, preventing direct LO leakage to the output.

Additionally, any residual feedthrough between the LO port and the other ports occurs through parasitic capacitances that are connected in series; as a result, the equivalent capacitance is dominated by the smallest parasitic element, significantly attenuating the coupling path. Moreover, the fully symmetric topology of the circuit ensures minimal imbalance. Since the output is generated as the product of differential input signals, it ideally vanishes when either input approaches zero. This behavior leads to strong common-mode rejection and contributes to the overall high common-mode rejection ratio (CMRR) of the structure.

4.4 Results Summary

The results obtained from circuit-level simulations at 300 K and 4 K show a clear improvement in the cryogenic model, particularly in terms of noise performance. In particular, the lower noise figure at 4 K can be mainly attributed to the reduction of thermal noise, while the enhancement in the compression point and IIP3 indicates a more favorable nonlinear behavior under cryogenic operation. Overall, the analysis confirms that cryogenic operation provides a significant advantage for the Gilbert multiplier when used as a mixer, making it a promising solution for low-temperature RF applications.

Conclusion

This work has presented the design, modeling, and characterization of a cryogenic Gilbert multiplier operating at 4 K, compared against its 300 K counterpart. Its behaviour has been compared with a Jones demodulator at 4 K and 300 K . The analysis has been carried out through a combination of theoretical modeling, circuit-level simulations, and performance metric evaluation, with particular emphasis on nonlinearity, noise, and spectral purity. The results demonstrate that the proposed analytical model, derived using a bidimensional Taylor series model approximation obtained from recursive defined functions, provides an accurate prediction of the fundamental mixing behavior at both RT and CT regimes. The amplitudes and frequency locations of these components show close agreement with transient simulations, validating the correctness of the second-order nonlinear terms included in the analytical formulation. This confirms that, despite the significant variation in device parameters at cryogenic temperatures, the dominant mixing contribution remains well captured by the linearized model. However, higher-order harmonics exhibit noticeable discrepancies. These deviations can be attributed to the intrinsic limitations of the truncated nonlinear model, which neglects higher-order contributions and limits regards the imposed DD-model over the cryogenic real model of the device. From a performance standpoint, the Gilbert-cell-based multiplier demonstrates superior Spurious-Free Dynamic Range (SFDR) when compared to the Jones demodulator. This improvement can be attributed to the inherently more symmetric topology and improved suppression of even-order distortion products in the Gilbert structure. The differential operation and better control of switching behavior contribute to a cleaner output spectrum, particularly under moderate input drive conditions. To reduce the effective power consumption, the gain of the mixer is low, that increase also the Noise figure of the device. Despite these limitations, the port-to-port isolation characteristics are found to be highly effective. In particular, LO-to-RF and LO-to-IF leakages are significantly suppressed, confirming the robustness of the differential topology and the effectiveness of the circuit symmetry. This aspect is especially critical in cryogenic quantum computing applications, where unwanted signal leakage can introduce back-action and degrade qubit coherence. In conclusion, the Gilbert multiplier represents a viable solution for cryogenic RF front-end applications, offering a favorable trade-off between linearity and isolation, while highlighting the need for improved gain and noise optimization in future developments. Further work may focus on extending the nonlinear model to higher orders and incorporating temperature-dependent device physics to enhance predictive accuracy under large-signal conditions.

A Current Mirror approximation [19]

Taking the following reference circuit:

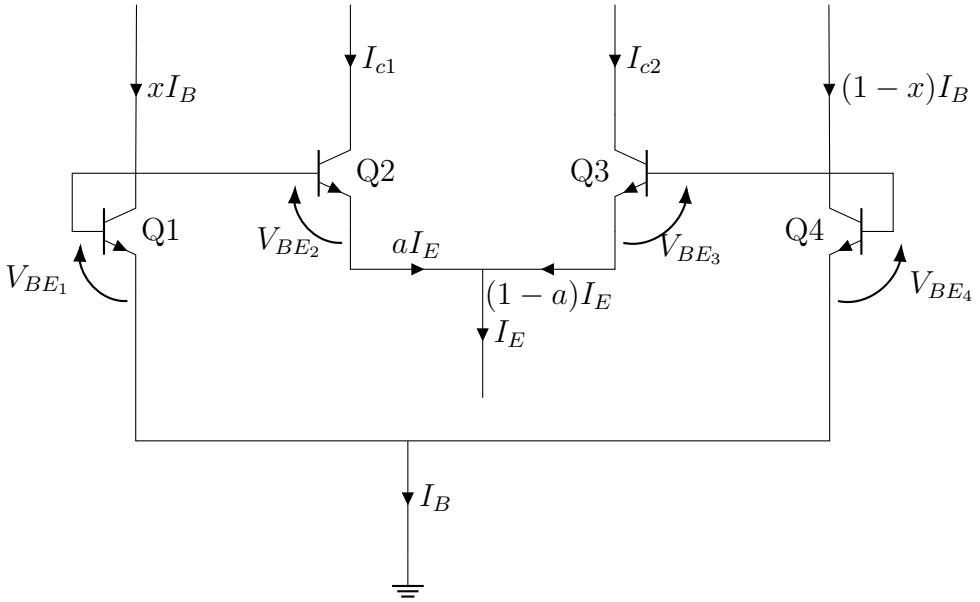


Figure A.0.1: Schematic

We can write the following equation:

$$V_{BE1} - V_{BE2} - (V_{BE4} - V_{BE3}) = 0 \tag{A.0.1}$$

Using the relation $V_{BE} = V_{th} \ln\left(\frac{I_C}{I_S}\right)$ we can rewrite the previous Equation as:

$$V_{th}\left[\ln\left(\frac{xI_B}{I_{s1}}\right) - \ln\left(\frac{aI_e}{I_{s2}}\right) - \ln\left(\frac{(1-x)I_B}{I_{s4}}\right) + \ln\left(\frac{(1-a)I_e}{I_{s3}}\right)\right] = 0 \tag{A.0.2}$$

Assuming that all the I_s current are equal, that is equivalent to say that they has the same emitter area. We can rewrite the relation in the following form:

$$\ln\left[\frac{xI_B}{(1-x)I_B}\right] = \ln\left[\frac{aI_e}{(1-a)I_e}\right] \tag{A.0.3}$$

Resolving the equation:

$$\frac{xI_B}{(1-x)I_B} = \frac{aI_e}{(1-a)I_e} \tag{A.0.4}$$

$$\frac{x}{1-x} = \frac{a}{1-a} \tag{A.0.5}$$

$$x = a \tag{A.0.6}$$

$$\tag{A.0.7}$$

Results that the collectors current are:

$$I_{c1} = xI_e \tag{A.0.8}$$

$$I_{c2} = (1-x)I_e \tag{A.0.9}$$

$$\tag{A.0.10}$$

B Cardano's demonstration

Starting from the Equation 3.3.64 and 3.3.65, they can be rewritten in a more generical form as below:

$$y^3 + py + q = 0 \tag{B.0.1}$$

the equation can be solved using the Cardano rule. The result depend on the Δ, defined as $\Delta = \left(\frac{q}{2}\right)^2 + \left(\frac{p}{3}\right)^3$. The possible solutions are:

$$\Delta > 0 \quad \text{for one real solution and two complex conjugate solutions} \tag{B.0.2}$$

$$\Delta = 0 \quad \text{for real solutions, with at least two coincident} \tag{B.0.3}$$

$$\Delta < 0 \quad \text{for three real distinct solution} \tag{B.0.4}$$

The solution can be found using the following steps: We can derive y as:

$$y = u + v = \sqrt[3]{-\frac{q}{2} + \sqrt{\frac{q^2}{4} + \frac{p^3}{27}}} + \sqrt[3]{-\frac{q}{2} - \sqrt{\frac{q^2}{4} + \frac{p^3}{27}}} \tag{B.0.5}$$

In the case of B.0.1, the $p = 0$, and the solution is for $\Delta = \left(\frac{q}{2}\right)^2 > 0$, the equation fall in the case B.0.2. We can now recover the value u and v for the Equation B.0.5 that, for $q < 0$, are respectively:

$$u = \sqrt[3]{-\frac{q}{2} + \sqrt{\frac{q^2}{4} + \frac{p^3}{27}}} = \sqrt[3]{-\frac{q}{2} + \sqrt{\frac{q^2}{4}}} = \sqrt[3]{-\frac{q}{2} + \frac{|q|}{2}} = -\sqrt[3]{q} \tag{B.0.6}$$

$$v = \sqrt[3]{-\frac{q}{2} - \sqrt{\frac{q^2}{4} + \frac{p^3}{27}}} = \sqrt[3]{-\frac{q}{2} - \sqrt{\frac{q^2}{4}}} = \sqrt[3]{-\frac{q}{2} - \frac{|q|}{2}} = \sqrt[3]{0} \tag{B.0.7}$$

The three possible solutions are:

$$y_1 = -\sqrt[3]{q} \quad \text{real solution} \tag{B.0.8}$$

$$y_{2,3} = u(-\frac{1}{2} \pm i\frac{\sqrt{3}}{2}) + v(-\frac{1}{2} \mp i\frac{\sqrt{3}}{2}) \quad \text{complex conjugated solutions} \tag{B.0.9}$$

By substituting the value of u and v, in our case the complex conjugate solutions become, :

$$y_{2,3} = -\sqrt[3]{q}(-\frac{1}{2} \pm \frac{\sqrt{3}}{2}) \tag{B.0.10}$$

Bibliography

[1] Fabio Sebastiano. "Fundamentals of Cryo-CMOS Circuits and Systems for Quantum Computing: Challenges and prospects in interfacing future quantum computers". In: *IEEE Solid-State Circuits Magazine* 17.3 (2025), pp. 61–71.

[2] Fabio Sebastiano et al. "Cryo-CMOS electronic control for scalable quantum computing". In: *Proceedings of the 54th Annual Design Automation Conference 2017*. 2017, pp. 1–6.

[3] Junhyeop Kim, Juhui Jeong, and Junghwan Han. "Cryogenic cmos active mixer employing transformer based current bleeding technique". In: *IEEE Transactions on Circuits and Systems II: Express Briefs* (2025).

[4] Emre Altuner, Ismail Serdar Özoğuz, and Mustafa Berke Yelten. "High-linearity Gilbert-cell mixer design for cryogenic applications". In: *Analog Integrated Circuits and Signal Processing* 113.2 (2022), pp. 249–256.

[5] Behzad Razavi and Razavi Behzad. *RF microelectronics*. Vol. 2. Prentice hall New York, 2012.

[6] Edwin H. Armstrong. "Method of Receiving High-Frequency Oscillations". US 1342885 A. June 8, 1920. URL: https://patents.google.com/patent/US1342885A/en.

[7] Edwin H. Armstrong. "Wireless receiving system." US1113149A. 1913. URL: https://patents.google.com/patent/US1113149A/en.

[8] Ralph V. L. Hartley. "Modulation system". US1666206A. 1928. URL: https://patents.google.com/patent/US1666206A/en.

[9] Donald K. Weaver. "A Third Method of Generation and Detection of Single-Sideband Signals". In: *Proceedings of the IRE* 44.12 (1956), pp. 1703–1705. DOI: 10.1109/JRPROC.1956.273272.

[10] Asad A. Abidi. "Direct-Conversion Radio Transceivers for Digital Communications". In: *IEEE Journal of Solid-State Circuits* 30.12 (1995), pp. 1399–1410.

[11] Ariel Luzzatto and Gadi Shirazi. *Wireless Transceiver Design*. Section 1.3.1, "Two-Step Conversion Transmitter". John Wiley & Sons, 2007. URL: https://catalogimages.wiley.com/images/db/pdf/047006076X.excerpt.pdf.

[12] T. D. Stetzler et al. "A 2.7–4.5 V Single Chip GSM Transceiver RF Integrated Circuit". In: *IEEE Journal of Solid-State Circuits* 30.12 (Dec. 1995), pp. 1421–1429. URL: https://ieeexplore.ieee.org/document/482189.

[13] RVL Hartley. "Relations of carrier and side-bands in radio transmission". In: *Proceedings of the Institute of Radio Engineers* 11.1 (2006), pp. 34–56.

[14] Alessandro Badiali et al. "Design of CMOS RFICs for the Quantum Microprocessor". In: (2026).

[15] Alessandro Badiali and Mattia Borgarino. "Cryo-CMOS multi-frequency modulator for 2-qubit controller". In: *Electronics* 13.13 (2024), p. 2546.

[16] John D Cressler and Guofu Niu. *Silicon-germanium heterojunction bipolar transistors*. Artech house, 2003.

[17] Michael A. Nielsen and Isaac L. Chuang. *Quantum Computation and Quantum Information*. 10th Anniversary Edition. Cambridge, UK: Cambridge University Press, 2010.

[18] N. R. Rizvi et al. "A Survey of Microwave-Implemented Superconducting Qubit Control Architectures". In: *IEEE Transactions on Applied Superconductivity, Vol. 7* (2026). Jan. 2026, pp. 6000152.

[19] Barrie Gilbert. "A high-performance monolithic multiplier using active feedback". In: *IEEE Journal of Solid-State Circuits* 9.6 (1974), pp. 364–373.

[20] Thomas H. Lee. *The Design of CMOS Radio-Frequency Integrated Circuits*. 2nd ed. Cambridge University Press, 2003.

[21] G.L. Patton et al. "63-75 GHz fT SiGe-base heterojunction bipolar technology". In: *Digest of Technical Papers.1990 Symposium on VLSI Technology*. 1990, pp. 49–50. DOI: 10.1109/VLSIT.1990.111002.

[22] John D. Cressler. "SiGe-Base Bipolar Transistors for Cryogenic BiCMOS Applications". In: *ESSDERC '92: 22nd European Solid State Device Research conference*. 1992, pp. 841–848. DOI: 10.1016/0167-9317(92)90556-7.

[23] Partha S Chakraborty et al. "A 0.8 THz f_{MAX} SiGe HBT Operating at 4.3 K". In: *IEEE Electron Device Letters* 35.2 (2014), pp. 151–153.

[24] Michael Schröter and Xiaodi Jin. "A physics-based analytical formulation for the tunneling current through the base of bipolar transistors operating at cryogenic temperatures". In: *IEEE Transactions on Electron Devices* 70.1 (2022), pp. 247–253.

[25] Jiahui Yuan et al. "An investigation of negative differential resistance and novel collector–current kink effects in SiGe HBTs operating at cryogenic temperatures". In: *IEEE transactions on electron devices* 54.3 (2007), pp. 504–516.

[26] Joseph Cheney Bardin. *Silicon-germanium heterojunction bipolar transistors for extremely low-noise applications*. California Institute of Technology, 2009.

[27] Jad Benserhir et al. "Broadband noise characterization of SiGe HBTs down to 4K". In: *IEEE Journal of the Electron Devices Society* (2025).

[28] Lin Song et al. *Characterization of bipolar transistors for cryogenic temperature sensors in standard CMOS*. 2016, pp. 1–3.

[29] Hanbin Ying et al. *Compact modeling of SiGe HBTs for design of cryogenic control and readout circuits for quantum computing*. 2020, pp. 1–4.

[30] Feng Liu, Zhi Deng, and Yinong Liu. "Cryogenic bandgap reference circuit with compact model parameter extraction of MOSFETs and BJTs for HPGe detectors". In: *IEEE Transactions on Nuclear Science* 67.10 (2020), pp. 2209–2216.

[31] S Bonen et al. "Cryogenic characterization of the high frequency and noise performance of SiGe HBTs from DC to 70 GHz and down to 2 K". In: *IEEE Microwave and Wireless Components Letters* 32.6 (2022), pp. 696–699.

[32] H Rücker, J Korn, and J Schmidt. "Operation of SiGe HBTs at cryogenic temperatures". In: *2017 IEEE Bipolar/BiCMOS Circuits and Technology Meeting (BCTM)*. IEEE. 2017, pp. 17–20.

[33] Beth O Woods, H Alan Mantooth, and John D Cressler. "SiGe HBT compact modeling for extreme temperatures". In: *2007 international semiconductor device research symposium*. IEEE. 2007, pp. 1–2.

[34] D Prêle et al. "Standard SiGe technologies operating at 4 K for front-end readout of SQUID arrays". In: *2006 8th International Conference on Solid-State and Integrated Circuit Technology Proceedings*. IEEE. 2006, pp. 191–193.

[35] Laleh Najafizadeh et al. "Sub-1-K operation of SiGe transistors and circuits". In: *IEEE Electron Device Letters* 30.5 (2009), pp. 508–510.

[36] Anton A Cherepanov, Ilya L Novikov, and Vladislav Yu Vasiliev. "An evaluation of SiGe HBT operation at cryogenic temperatures". In: *2019 20th International Conference of Young specialists on Micro/Nanotechnologies and Electron Devices (EDM)*. IEEE. 2019, pp. 23–27.

[37] Sander Weinreb, Joseph C Bardin, and Hamdi Mani. "Design of cryogenic SiGe low-noise amplifiers". In: *IEEE transactions on microwave theory and techniques* 55.11 (2007), pp. 2306–2312.

[38] EF Crabbe et al. "Low temperature operation of Si and SiGe bipolar transistors". In: *International Technical Digest on Electron Devices*. IEEE. 1990, pp. 17–20.

[39] John D Cressler. "Silicon-germanium as an enabling technology for extreme environment electronics". In: *IEEE Transactions on Device and Materials Reliability* 10.4 (2010), pp. 437–448.

[40] Behzad Razavi. *Fundamentals of microelectronics*. John Wiley & Sons, 2021.

[41] E. Charbon et al. "Cryo-CMOS for quantum computing". In: *Proceedings / conference paper* (2017). Cryogenic CMOS for scalable quantum computing. URL: https:

//infoscience.epfl.ch/entities/publication/256873eb-772f-4b74-a1f6-13154554e037.

[42] B. Patra et al. "Cryo-CMOS Circuits and Systems for Quantum Computing Applications". In: *IEEE Journal of Solid-State Circuits* (2017). URL: https://research.tudelft.nl/en/publications/cryo-cmos-circuits-and-systems-for-quantum-computing-applications.

[43] X. Li et al. "Cryogenic Characterization of 28 nm Bulk CMOS Technology for Quantum Computing". In: *arXiv preprint arXiv:1806.01142* (2018). URL: https://arxiv.org/abs/1806.01142.

[44] Chang He et al. *Optimized Cryo-CMOS Technology with VTH<0.2V and Ion>1.2mA/um for High-Peformance Computing*. 2024. arXiv: 2411.03099 [eess.SY]. URL: https://arxiv.org/abs/2411.03099.

[45] Zhidong Tang and other. *Generic Cryo-CMOS Device Modeling and EDACompatible Platform for Reliable Cryogenic IC Design*. 2024. arXiv: 2211.05309 [eess.SY]. URL: https://arxiv.org/abs/2211.05309.

[46] J. Kim et al. "Cryo-CMOS Electronics For Quantum Computing: Bringing Classical Electronics Closer to Qubits". In: *IEEE conference / journal paper* (2021). URL: https://ieeexplore.ieee.org/document/9467038/.

[47] Faisal Bashir et al. "Cryogenic electronics for high performance computing applications: A comprehensive review". In: *Materials Today Physics* 59 (2025), p. 101960. ISSN: 2542-5293. DOI: https://doi.org/10.1016/j.mtphys.2025.101960. URL: https://www.sciencedirect.com/science/article/pii/S2542529325003165.

[48] Rosario M. Incandela et al. "Characterization and Compact Modeling of Nanometer CMOS Transistors at Deep-Cryogenic Temperatures @IEEE2018". In: *IEEE Journal of the Electron Devices Society* 6 (2018), pp. 996–1006. ISSN: 2168-6734. DOI: 10.1109/JEDS.2018.2821763.

[49] Jay Orear. "Enrico Fermi-The Master Scientist". In: *Cornell University Press* (2004).

[50] H. E. Jones. "Dual output synchronous detector utilizing transistorized differential amplifiers". US Patent US3241078A. 1963. URL: https://patents.google.com/patent/US3241078A/en.

[51] B. Gilbert. "A DC–500 MHz Amplifier/Multiplier Principle". In: *IEEE International Solid-State Circuits Conference (ISSCC) Digest of Technical Papers*. Feb. 1968, pp. 114–115.

[52] B. Gilbert. "Translinear Circuits: An Historical Overview". In: *Analog Integrated Circuits and Signal Processing* 9 (1996), pp. 95–118. DOI: 10.1007/BF00166408.